Radiative and dynamic controls of global scale energy fluxes

Aaron Donohoe

A dissertation submitted in partial fulfillment
of the requirements for the degree of

Doctor of Philosophy

University of Washington

DRAFT 2011 DRAFT

Program Authorized to Offer Degree: Atmospheric Sciences

University of Washington

Abstract

Radiative and dynamic controls of global scale energy fluxes

Aaron Donohoe

Chair of the Supervisory Committee:
Professor David S. Battisti
Atmospheric Sciences

In this thesis I study the processes that control the global scale energy budget of the climate system and the fluxes of energy within the climate system using both models and data. I focus on three primary questions: (1) What determines the Earth's planetary albedo? (2) What determines the meridional heat transport in the climate system? (3) What controls the seasonal amplitude of energy fluxes on the equator-to-pole scale?

(1) Planetary Albedo The planetary albedo is partitioned into a component due to atmospheric reflection and a component due to surface reflection by using shortwave fluxes at the surface and top of the atmosphere in conjunction with a simple radiation model. The vast majority of the observed global average planetary albedo (88%) is due to atmospheric reflection. Surface reflection makes a relatively small contribution to planetary albedo because the atmosphere attenuates the surface contribution to planetary albedo by a factor of approximately three. The global average planetary albedo in the ensemble average of the CMIP3 pre-industrial simulations is also primarily (87%) due to atmospheric albedo. The inter-model spread in planetary albedo is relatively large and is found to be predominantly a consequence of inter-model differences in atmospheric albedo, with surface processes playing a much smaller role despite significant inter-model differences in surface albedo. The CMIP3 models show a decrease in planetary albedo under a doubling of carbon dioxide – also primarily due to changes in atmospheric reflection (which explains more than 90% of the

inter-model spread). All models show a decrease in planetary albedo due to the lowered surface albedo associated with a contraction of the cryosphere in a warmer world, but this effect is small compared to the spread in planetary albedo due to model differences in the change in clouds.

(2) Meridional Heat Transport The meridional heat transport (MHT) is expressed as the difference between the equator-to-pole contrast in absorbed solar radiation (ASR^*) and outgoing longwave radiation (OLR^*). As an example, in the Northern Hemisphere observations, the extratropics receive an 8.1 PW deficit of net solar radiation (ASR*) relative to the global average that is balanced by a 2.4 PW deficit of outgoing longwave radiation (OLR^*) and 5.7 PW of energy import via the atmospheric and oceanic circulation (MHT). The inter-model spread of MHT in the CMIP3 simulations of the pre-industrial climate is primarily ($R^2 = 0.72$) due to differences in ASR^* while model differences in OLR^* are uncorrelated with the MHT spread. ASR* is partitioned into components due to the incident radiation at the top of the atmosphere and the equator-to-pole contrast of planetary albedo which is further subdivided into components due to atmospheric and surface reflection. In the observations 62% of ASR^* is due to the meridional distribution of incident radiation, 33% is due to atmospheric reflection, and 5% is due to surface reflection. The inter-model spread in ASR^* is due to model differences in the equator-to-pole gradient in planetary albedo that are primarily a consequence of atmospheric reflection differences (92% of the spread) and is uncorrelated with differences in surface reflection. As a consequence, MHT in climate models is primarily determined by cloud reflection. These ideas are extended to simulations of anthropogenic global warming and paleoclimate states where it is found that changes in cloud reflection exert as profound an influence on MHT as even zeroeth order changes in surface albedo.

(3) Seasonal energy fluxes The seasonal amplitude of energy fluxes to the extratropics is driven by large variations in solar radiation that are primarily balanced by ocean heat storage anomalies; changes in meridional heat transport, emitted long wave radiation, and

atmospheric heat storage play a decreasingly important role in the seasonal energy balance. We use a simplified coupled (atmosphere-ocean) energy balance model to understand the seasonal amplitude of the various extratropical energy fluxes. The model is found to reproduce the sensitivity of the energy fluxes to the ocean mixed layer depth found in an ensemble of aquaplanet general circulation model simulation with varying mixed layer depths. Land-ocean contrasts also have a large impact on the seasonal energetics of the extratropical climate system. Over the ocean, zonal heat transport from the land domain is maximized during the summer, and the sum of the insolation and zonal heat transport anomalies is balanced by ocean heat storage. In contrast, over the land, the primary summertime balance is excess solar insolation balanced by an enhanced zonal heat export. The observed seasonal cycle of energy fluxes and the land and ocean temperatures are replicated in a simplified energy balance model that includes land-ocean contrast and the hemispheric differences in fractional land area. The sensitivity of the seasonal cycle in climate (atmosphere and ocean temperatures) - and in the gross partitioning of the mix of energy flux processes that determine the climate - to the fractional land area is further explored in an ensemble of energy balance model integrations. In both the aquaplanet and land-ocean contrast energy balance models, the partitioning of energy fluxes amongst different physical processes can be understood in terms of the sensitivity of those processes to temperature perturbations.

TABLE OF CONTENTS

LIST OF FIGURES

LIST OF TABLES

Chapter 1

INTRODUCTION

The global scale energy fluxes within the climate system are a consequence of both radiative and dynamical processes and their mutual interactions. For example, the annual mean meridional heat transport in the atmosphere and ocean can be diagnosed from the radiative fields – as the net radiative cooling integrated over the polar cap– or from the dynamic fields – as the column integral of the moist static energy flux. The two calculations of the meridional heat transport rely on very different pieces of information but are self consistent with each other; the large scale radiative fields are set up by the dynamic flux of moist static energy and the flux of moist static is influenced by the gradient in the radiative fields. Thus, the diagnostic tool (either the radiative or dynamic fields) used to calculate the meridional heat transport does not prove causality and a complete understanding of the physical processes that determine the magnitude of the heat flux requires that the radiative and dynamic energy fluxes be viewed in a common framework.

In this thesis, we explore the radiative and dynamic controls of large scale energy fluxes from the perspective of the atmospheric energy budget on hierarchy of spatio-temporal scales. We consider the following energy fluxes: (i) absorbed shortwave radiation (ASR), (ii) outgoing longwave radiation (OLR) , (iii) meridional heat transport (MHT), (iv) storage (in the atmospheric or oceanic column), and (v) zonal atmospheric heat transport between the ocean and land domain (ZHT). We adopt a multi-scale approach because spatio-temporal averaging isolates certain physical processes by eliminating other processes. For example, global averaging eliminates the meridional heat transport (since energy can only be re-organzied within the system but not added to or removed from the system by atmospheric and oceanic energy transports) and annual averaging in a steady state system eliminates energy storage. Table 1.1 summarizes the energy fluxes that contribute to the climate

Spatio/temporal averaging	ASR	OLR	MHT	Storage	ZHT
Global/Annual	O	O	X	X	X
Zonal/Annual	O	O	O	X	X
Global/Seasonal	O	O	X	O	X
Zonal/Seasonal	O	O	O	O	X
Land-Ocean contrast/Seasonal	O	O	O	O	O

Table 1.1: Summary of the energy fluxes that contribute to the climate system's energy budget on different spatio-temporal scales. O's (X's) indicate that the energy flux does (does not) contribute.

system's energy budge on different spatio-temporal scales.

The analysis of the large scale energy fluxes within the climate system on multiple scales allows us to isolate and understand a small number of processes on large spatio-temporal scales, apply this understanding to smaller spatio-temporal scales, and ultimately put radiative and dynamic energy fluxes into a common conceptual framework. The processes that control the global and annual average energy budget also affect the local and seasonal energy budget with the added complication that dynamic energy transports and energy storage also come into play on the smaller spatio-temporal scales. If we take the lessons we learn from the global and annual average energy budget and apply them to the smaller scale, we can reconcile the relative importance of the dynamic and radiative fluxes on the local and seasonal scale. In this thesis, we start from the largest spatio-temporal scale (the global and annual mean) where a limited number of energy fluxes are isolated and work towards smaller scales (the seasonal cycle and land-ocean contrast) where more physical processes are involved.

In the annual and global average, the climate system achieves radiative equilibrium at the top of the atmosphere (TOA); the annual and global average ASR must equal the annual and global average OLR in a steady climate system. In chapter 2, we ask, what controls the global and annual average net shortwave radiation at the TOA (ASR)? More specifically, the fraction of incident radiation at the TOA that is reflected back to space, the Earth's planetary albedo, is a consequence of both atmospheric reflection and surface

reflection. We partition the planetary albedo between atmospheric and surface reflection and demonstrate that the vast majority of the observed annual and global average planetary albedo is due to atmospheric reflection, primarily due to clouds. We also demonstrate that the global and annual average planetary albedo (and thus ASR) in climate models is primarily a consequence of cloud reflection and differences in cloud reflection account for the vast majority of the planetary albedo differences between models and the anticipated changes due to anthropogenic greenhouse gases.

On the equator-to-pole scale, the climate system achieves an annual average three-way energy balance between ASR, OLR, and MHT. For example, the extratropics receive a deficit of ASR (relative to the global average) that is balanced by the sum of the OLR deficit over the same region and MHT from the tropics to the extratropics. In Chapter 3, we demonstrate that the models used in the IPCC's fourth assessment (International Panel on Climate Change [Solomon et al., 2007) feature a remarkably large spread in the magnitude of MHT. We further demonstrate that this spread is due to inter-model differences in the meridional gradient of ASR and is unrelated to inter-model differences in OLR. The model differences in the meridional gradient in ASR, in turn, are a consequence of model differences in cloud reflection. Thus, the same processes that were found to control the annual and global average ASR in Chapter 2, also influence the equator-to-pole contrast of ASR and thus the dynamic heat transport in the system (MHT). Our results demonstrate that the extratropical deficit of ASR is a consequence of the modeled cloud field and is balanced primarily by MHT and secondarily by OLR suggesting that, on the equator-to-pole scale, MHT is a more efficient pathway toward achieving energy balance than OLR.

We gain further insight into the radiative and dynamic controls of atmospheric energy fluxes by analyzing the seasonal cycle of the observed energy fluxes (Chapter 4). A simplified linearized energy balance model that divides the globe into three boxes (the extratropics in each hemisphere and the tropics) each with an atmosphere and ocean is introduced. The simplified model reproduces the observed mix of energy fluxes over the multitude of spatio-temporal scales considered in this study (ranging from the global annual average

to the seasonal land-ocean contrast). The magnitude of the various energy fluxes and storage can be understood in terms of the energy export efficiencies in the model which are defined as the change in the energy flux per unit change in temperature. In this framework, energy fluxes in the climate system are imposed by the spatio-temporal pattern of ASR and the climate system achieves equilibrium via the most efficient energy export and storage pathways. This conclusions persist over the multitude of spatio-temporal scales considered in this study subject only the modification of the number energy fluxes that contribute at each scale (Table 1.1).

Finally, in Chapter 5, we discuss how the conclusions reached in each section relate to each other. Specifically, we argue that the inter-model spread in *MHT* (Chapter 3) is a natural consequence of the inter-model spread in planetary albedo (Chapter 2) and the relative efficiencies of dynamic and radiative energy export on the equator-to-pole scale (Chapter 4).

Chapter 2

ATMOSPHERIC AND SURFACE CONTRIBUTIONS TO PLANETARY ALBEDO

2.1 Introduction

The ratio of reflected to incident shortwave radiation at the top of the atmosphere (TOA), the Earth's planetary albedo, is a function of climate state and exerts a profound influence on the Earth's climate. As a reference point, Budyko (1969) postulated that a change in global average planetary albedo of less than 0.02 units could cause global glaciation of the climate system. The radiative forcing associated with a doubling of carbon dioxide above the pre-industrial atmospheric concentration (3.7 Wm^{-2}, International Panel on Climate Change [Solomon et al. (2007)) is approximately equivalent to a 0.01 unit change in global average planetary albedo. The magnitude of temperature variability seen over the Holocene (Moberg et al., 2005) is consistent with planetary albedo variations of 0.01 units or less (Cahalan et al., 1994; Bender et al., 2010).

The meridional structure of planetary albedo is also inextricably linked to the strength of the atmospheric and oceanic circulation. The large scale circulation is primarily driven by the equator pole gradient in net shortwave radiation (Hartmann, 1994) which owes approximately one third of its existence to meridional gradient in planetary albedo (Stone, 1978). Climate states with altered meridional structures of planetary albedo exhibit varying magnitudes of meridional heat transport (Enderton and Marshall, 2009).

Finally, changes in planetary albedo associated with both cloud and surface processes are among the most powerful feedback processes in the response of the climate system to anthropogenic forcing (Bony and coauthors, 2006), and variations in the planetary albedo feedback explain a large portion of the inter-model spread in climate sensitivity among global climate models (Bender et al., 2006). Understanding the processes that control the Earth's

planetary albedo in the current climate state is central to predicting how the planetary albedo will respond to future climate changes.

The planetary albedo is a function of the optical properties of objects within the atmosphere (e.g., clouds, water vapor, and aerosols) and objects that constitute the planet's surface (e.g., ice, ocean, and trees) (Wielicki et al., 1995; Hall, 2004). It is convenient to lump the atmosphere's contribution to planetary albedo into three bulk processes: (a) clouds and aerosols that directly reflect incident solar radiation back to space, (b) atmospheric opacity to downwelling shortwave radiation that limits the amount of downwelling shortwave radiation reaching the surface and, (c) atmospheric opacity to shortwave radiation upwelling from the surface that limits the amount of shortwave radiation reflected by the surface that escapes to space (Qu and Hall, 2005). Thus, the atmosphere influences the planetary albedo by way of direct reflection back to space (process a) and by attenuating the effect of surface albedo on planetary albedo (processes b and c). Both the atmospheric and surface contributions to planetary albedo are functions of the climate state.

Several studies have examined the surface contribution to local planetary albedo in the polar regions. Gorodetskaya et al. (2006) used the satellite record of planetary albedo in conjunction with observational data sets of snow and ice concentration to demonstrate that changing ice/snow concentrations from 0% to 100% would result in local planetary albedo changes of order 0.20 with some regional dependence. This number is significantly less than the change in surface albedo associated with the melting of the cryosphere (Hummel and Reck, 1979) which suggests that the atmosphere strongly attenuates the impact of the surface albedo change on the planetary albedo. Qu and Hall (2005) found that surface reflection accounts for less than 25% of the climatological planetary albedo in the ice- and snow-covered regions of the planet and the remainder is due to clouds. They also found that, although the year-to-year variability of planetary albedo in cryospheric regions is mainly due to changes in surface albedo, atmospheric processes attenuate the effect of the surface albedo changes on the local planetary albedo by as much as 90% (i.e. the change in planetary albedo is 10% of the change in surface albedo).

In this study, we quantify the relative contributions of the surface and atmosphere to planetary albedo in the observations (Section 2.2). We then perform the same analyses on the output of the pre-industrial integrations from the climate models used in the International Panel on Climate Change (IPCC) Fourth Assessment Report (AR4) to determine whether the relative contributions of surface and atmospheric processes to the total planetary albedo observed in Nature is captured in the model simulations. We also calculate the inter-model spread in the hemispheric average planetary albedo and determine what portion of this spread is due to surface or atmospheric processes (Section 2.3). Finally, we analyze the changes in planetary albedo in the AR4 climate models due to a doubling of atmospheric carbon dioxide concentration and partition the changes in planetary albedo between changes in atmospheric and surface processes. We also examine planetary albedo in vastly different climate states, ranging from the last glacial maximum to an ice-free aquaplanet (Section 2.4). A summary and discussion of our results follows.

2.2 Partitioning of planetary albedo in Nature

In this section, we partition the observed planetary albedo into atmospheric and surface components and assess the contribution of each component to the hemispheric average planetary albedo.

2.2.1 Datasets used

We use the TOA and surface shortwave radiation data products from the Clouds and Earth's Radiant Energy System (CERES) experiment (Wielicki et al., 1996). We use Fasullo and Trenberth's (2008a,b) long term climatologies of the CERES TOA data that correct for missing data and global average energy imbalances. For the surface shortwave fluxes we use the CERES "AVG" fields which are derived by assimilating the satellite observations into a radiative transfer model to infer the surface fluxes (Rutan et al., 2001). All calculations are performed separately for each of the four CERES instruments (FM1 and FM2 on Terra from 2000 -2005 and FM3 and FM4 on AQUA from 2002 – 2005). We then average the

results over the four instruments. Our calculations are performed on the annual average (solar-weighted) data.

The observed TOA fluxes from CERES differ from previous satellite measurements from the Earth Radiation Budget Experiment (Barkstrom et al., 1989) by as much as 8 W m^{-2} in the zonal average (Trenberth et al., 2009; Loeb et al., 2009). The instrumental absolute calibration error in the CERES TOA fluxes are as large as 4.2 Wm^{-2} (Loeb et al., 2009) and the total error in the global average shortwave flux is estimated to be 2.6 W m^{-2} (Bender et al., 2006). Similarly, the CERES surface shortwave fluxes have systematic errors ranging from 3% to 5% (Kratz et al., 2010) and random errors in the hourly retrievals of order tens of W m^{-2} (see Trenberth et al., 2009, for a discussion) . In appendix A, we propagate the errors in the observational fluxes to obtain error estimates for the quantities calculated in this study.

2.2.2 Partitioning planetary albedo into atmospheric and surface components

2.2.2.1 Methodology

We now describe a methodology for partitioning the planetary albedo into atmospheric and surface components, given the upwelling and downwelling solar fluxes at both the TOA and the surface. We will denote the atmospheric contribution to the planetary albedo as $\alpha_{P,ATMOS}$ and the surface contribution to planetary albedo as $\alpha_{P,SURF}$ in the remainder of this paper.

At each gridpoint we build a single layer model of solar radiation that accounts for three shortwave processes: atmospheric reflection, atmospheric absorption and, surface reflection. We assume that each of these processes is isotropic; a certain percentage of the incident radiation is absorbed per pass through the atmosphere and a different percentage of the incident radiation is reflected per pass through the atmosphere. For example, of the total downwelling solar radiation incident at the TOA (S), a fraction R is reflected by the atmosphere, a fraction A is absorbed by the atmosphere and the remainder is transmitted to the surface. Of the transmitted radiation, a fraction α (the surface albedo) is reflected at the

surface back toward the atmosphere. Of this reflected radiation, a portion R is reflected back to the surface by the atmosphere, a portion A is absorbed within the atmosphere, and the remainder is transmitted to space Fig. 2.1. These processes are repeated for an infinite number of reflections. Hence, the annual mean upwelling solar flux at each gridpoint at the TOA is:

$$\begin{aligned} F\uparrow_{TOA} &= S[R + \alpha(1-R-A)^2 + \alpha^2 R(1-R-A)^2 + \alpha^3 R^2(1-R-A)^2 ..... \\ &= SR + S\alpha(1-R-A)^2[1 + (\alpha R) + (\alpha R)^2 ....] = SR + S\alpha\tfrac{(1-R-A)^2}{1-\alpha R} \end{aligned} , \quad (2.1)$$

where F$\uparrow_{TOA}$ is the upwelling solar flux at the TOA and the convergence of the infinite series to the final expression on the right hand side is ensured because both R and α are less than 1 (Qu and Hall, 2005). Similar convergent infinite series can be obtained for the downwelling and upwelling solar fluxes at the surface:

$$F\downarrow_{SURF} = S\frac{(1-R-A)}{1-\alpha R} \quad (2.2)$$

and

$$F\uparrow_{SURF} = \alpha S\frac{(1-R-A)}{1-\alpha R} = \alpha F\downarrow_{SURF} \quad (2.3)$$

Therefore, given data-sets of shortwave radiative fluxes on the left hand side of Eqs. 2.1-2.3 and S, these equations represent a system of 3 equations in terms of three unknown variables: A, R, and α. In practice, the ratio of upwelling to downwelling radiation at the surface (Eqs. 2.3 and 2.2) defines α such that the system can be reduced to two equations (2.1 and 2.2) and two unknowns (A and R)[1].

Solving these equations results in spatial maps of R (Fig. 2.2d) and A (not shown). Dividing Eq. 2.1 by S and separating the two terms allows us to partition the planetary albedo into atmospheric ($\alpha_{P,ATMOS}$) and surface components ($\alpha_{P,SURF}$):

---

[1]One can show that all possible solutions to our equations have $0 \leq R \leq 1$ and $0 \leq A \leq 1$, although it is not clear to us whether a solution to the generalized system of equations must exist. Nonetheless, solutions to Eqs. 2.1–2.3 exist at all gridpoints for the datasets and GCM output discussed in this paper. Furthermore, all solutions (A and R values at each gridpoint) discussed here are unique.

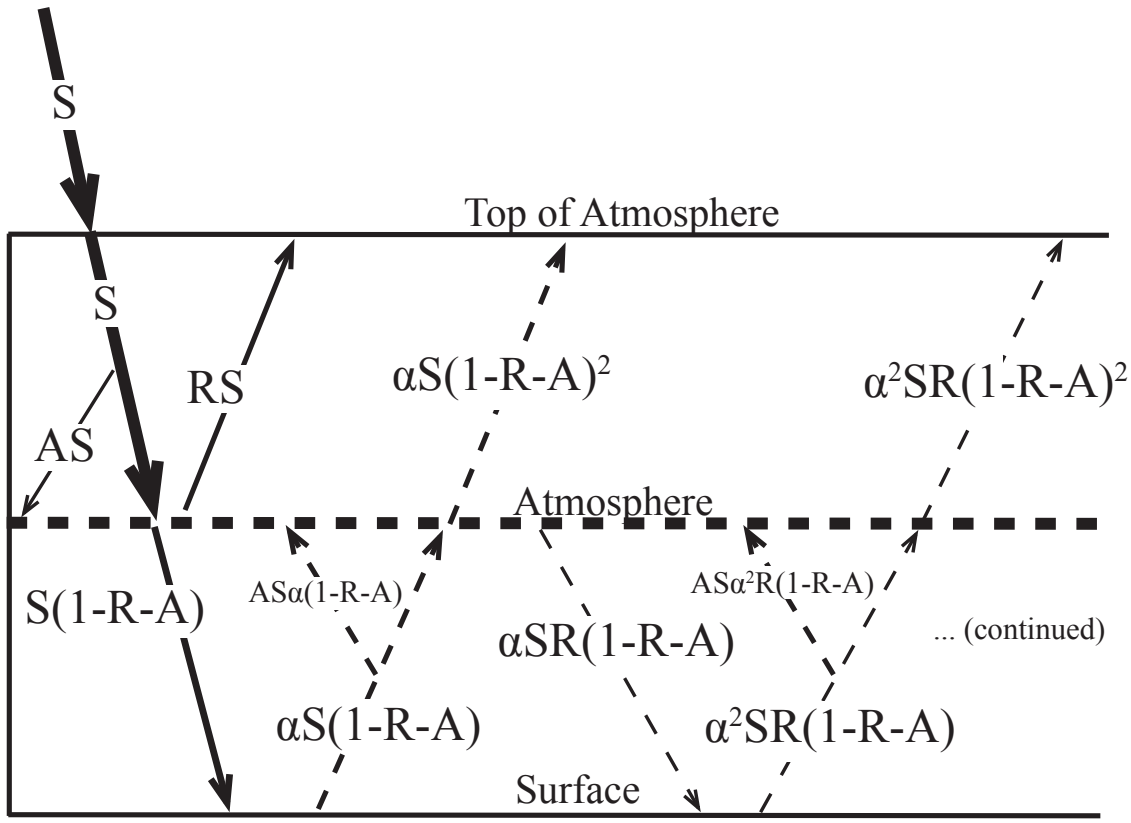

Figure 2.1: Schematic representing the first two reflections in the single layer solar radiation model. Moving from left to right, the arrows represent the radiative fluxes associated with the incident solar, first reflection, and second reflection. A, R, and α are the atmospheric absorption fraction during a single pass through the atmosphere, the fraction of cloud reflection, and the surface albedo respectively. The solid arrows at the TOA represent the radiative fluxes we associated with cloud reflection and the dashed arrows represent the radiative fluxes we associate with the surface reflection.

$$\alpha_{P,ATMOS} = R \tag{2.4}$$

and

$$\alpha_{P,SURF} = \alpha \frac{(1 - R - A)^2}{1 - \alpha R}. \tag{2.5}$$

$\alpha_{P,ATMOS}$ is due to direct reflection by the atmosphere (the first term on the right hand side of (2.1)). All of the solar radiation that is reflected by the surface and eventually passes through the TOA (the second term on the right hand side of Eq. 2.1) is attributed to $\alpha_{P,SURF}$. By definition, the surface and atmospheric contributions to planetary albedo sum to the planetary albedo:

$$\alpha_P = \alpha_{P,ATMOS} + \alpha_{P,SURF}. \tag{2.6}$$

Maps of $\alpha_{P,SURF}$ and $\alpha_{P,ATMOS}$ are shown in Fig. 2.2.

We calculate $\alpha_{P,ATMOS}$ and $\alpha_{P,SURF}$ using annual average (solar weighted) data. We have also performed the partitioning on the climatological monthly mean data and then averaged the monthly values of $\alpha_{P,ATMOS}$ and $\alpha_{P,SURF}$ to obtain the annual average climatology. The annual and zonal average $\alpha_{P,ATMOS}$ calculated from the monthly data agree with that calculated directly from the annual average data to within 1% of $\alpha_{P,ATMOS}$at all latitudes.

We note that Taylor et al. (2007) (hereafter T07) used a similar simplified radiative transfer model to partition planetary albedo into surface and atmospheric components. In contrast to our formulation, T07 assumed absorption only occurs on the first downward pass through the atmosphere and occurs above the level of atmospheric reflection. The impact of the differences in model formulation on the derived quantities $\alpha_{P,ATMOS}$ and $\alpha_{P,SURF}$ are reported in Appendix B. The qualitative conclusions found in this study are independent of the assumptions made in the simplified radiative transfer model.

Symbol	Meaning
α	Surface albedo
α_P	Planetary albedo = TOA albedo
A	Percent of absorption during each pass through the atmosphere
R	Percent of reflection during each pass through the atmosphere
$\alpha_{P,ATMOS}$	Atmospheric contribution to planetary albedo
$\alpha_{P,SURF}$	Surface contribution to planetary albedo
χ	Atmospheric attenuation of surface albedo

Table 2.1: Variables used in this chapter.

2.2.2.2 Results

The maps of surface and planetary albedo exhibit large values in the polar regions, with larger spatial differences in the meridional direction than in the zonal direction (Fig. 2.2); the predominant spatial structure in both maps is an equator-to-pole gradient. Significant meridional gradients in surface albedo are constrained to be at the transition to the cryospheric regions (around 70° in each hemisphere) whereas the meridional gradients in planetary albedo are spread more evenly across the storm track regions (from 30° to 60°).

The percentage of solar radiation absorbed during a single pass through the atmosphere (A, not shown) features a predominant equator-to-pole gradient with tropical values of order 25% and high latitude values of order 15% with still smaller values occurring over the highest topography. The global pattern of atmospheric solar absorption is virtually identical to the pattern of vertically integrated specific humidity (from NCEP reanalysis) with a spatial correlation coefficient of 0.92; this is expected because the atmospheric absorption of solar radiation is predominantly due to water vapor and ozone (M.D. and Lee, 1996) while clouds and black carbon each contribute less than 10% of the atmospheric absorption (Kim and Ramanathan, 2008).

The map of $\alpha_{P,ATMOS}$ (Fig. 2.2d) shows several anticipated features: 1. high values associated with the intertropical convergence zone in the equatorial Pacific; 2. low values in

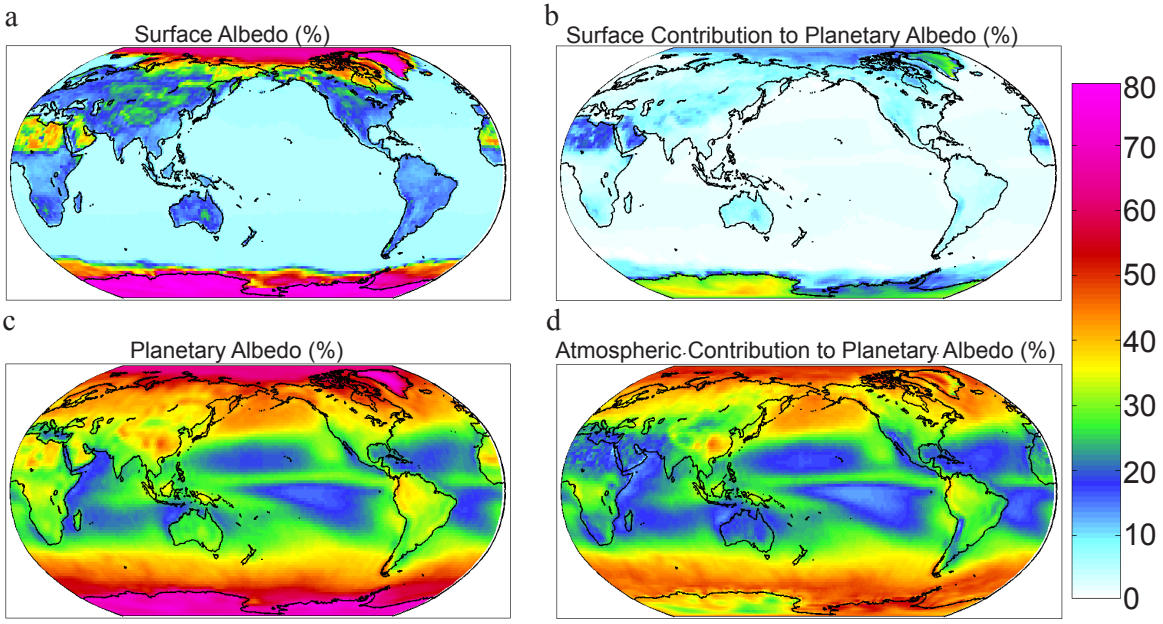

Figure 2.2: (a and c) The surface albedo and planetary albedo, expressed as a percent. (b and d) $\alpha_{P,SURF}$ and $\alpha_{P,ATMOS}$ expressed as a percent.

the drier subtropics; 3. high values in the NH Atlantic and Pacific storm tracks and in the nearly zonally symmetric SH storm track associated with synoptic storms; 4. high values in the Arctic and West Antarctica that tend to be cloudy during the local summer (Curry et al., 1996); 5. high values over placeSouth East Asia associated with extensive cold season stratocumulus (Hahn and Warren, 2003).

As is true for the planetary albedo and $\alpha_{P,ATMOS}$, $\alpha_{P,SURF}$ is greater in the polar regions than in the tropics. More important, however, is that $\alpha_{P,SURF}$ is greatly attenuated by the atmosphere (cf. the top two panels of Fig. 2.2) – so much so that almost everywhere the planetary albedo is largely determined by the atmospheric and not the surface contribution (cf. the right two panels of Fig. 2.2). Our simple radiative model predicts that $\alpha_{P,SURF}$ will be attenuated by square of the atmospheric transmissivity: $(1\text{-}R\text{-}A)^2$ (Eq. 2.5 and Fig. 2.1). In this framework, we can see that while the atmospheric opacity primarily acts to damp the impact of the surface albedo on planetary albedo, the atmosphere also imparts some spatial structure to $\alpha_{P,SURF}$ by virtue of the spatial structure in atmospheric opacity. For example, the surface albedo over Antarctica is fairly uniform, but $\alpha_{P,SURF}$ is much larger over East Antarctica because the atmosphere over East Antarctica is less opaque (both less cloud and less absorption by water vapor) than that over West Antarctica.

Atmospheric processes play a much greater role than surface processes in determining the amplitude and structure of planetary albedo, both regionally and in the global average. The (solar weighted) global average planetary albedo of 0.298 is partitioned into a global average $\alpha_{P,ATMOS}$ of 0.262 (88% of the total) and a global average $\alpha_{P,SURF}$ of 0.036 (12%, Table 2.2). These results are in qualitative agreement with Qu and Hall's (2005) conclusion that, "the atmosphere accounts for much more of the climatological planetary albedo (= 75%) than the surface ...". The hemispheric average planetary albedo is very similar in both hemispheres (0.299 in the NH versus 0.298 in the SH) although the partitioning between $\alpha_{P,ATMOS}$ and $\alpha_{P,SURF}$ differs slightly between the hemispheres ($\alpha_{P,ATMOS}$ contributes 86% of the hemispheric average planetary albedo in the NH as compared to 90% in the SH).

The zonal average planetary albedo, partitioned into $\alpha_{P,ATMOS}$and $\alpha_{P,SURF}$, is shown

(%)	Total	$\alpha_{P,ATMOS}$	$\alpha_{P,SURF}$	Surface Albedo
Observations	29.8	26.2	3.6	12.3
Observational Uncertainty (2σ)	0.8	1.8	0.9	
Model Average	30.4	26.4	4.0	13.2
Model Spread (2σ)	1.6	2.3	1.3	3.1

Table 2.2: Global average planetary albedo, its decomposition into atmospheric ($\alpha_{P,ATMOS}$) and surface ($\alpha_{P,SURF}$) components (as described in the text), and global average surface albedo for the observations and the CMIP3 multi-model average and spread (2 standard deviations). The observational uncertainty on total planetary albedo is taken from Bender et al. (2006). The observational uncertainty on $\alpha_{P,ATMOS}$and$\alpha_{P,SURF}$ is assessed by the method described in Appendix B. All entries are in percent units.

in Fig. 2.3a. At all latitudes, $\alpha_{P,ATMOS}$is greater than $\alpha_{P,SURF}$. $\alpha_{P,SURF}$ has higher values over the cryospheric and NH land mass regions, owing to the high surface albedo in those regions. $\alpha_{P,ATMOS}$is largest in the storm track regions and Arctic where clouds are prevalent and smallest in the dry subtropics; both the meridional structure of cloud fraction and solar zenith angle (Minnett, 1999) contribute to the meridional structure of $\alpha_{P,ATMOS}$.

As can be seen in Fig. 2.3b (or by comparing the top two panels of Fig. 2.2), $\alpha_{P,SURF}$ is much smaller than the actual surface albedo, α, because (1) the downwelling solar radiation at the TOA is attenuated by atmospheric reflection and absorption as it passes downward through the atmosphere and (2) the solar radiation reflected by the surface is attenuated by atmospheric absorption and reflection as it passes upwards from the surface to the TOA. Even over the polar regions, where the zonal mean surface albedo exceeds 70%, $\alpha_{P,SURF}$ never exceeds 30%. We define the atmospheric attenuation of surface albedo, χ, as

$$\chi = (1 - \frac{\alpha_{P,SURF}}{\alpha}) = 1 - \frac{(1 - R - A)^2}{1 - R\alpha}. \tag{2.7}$$

The atmospheric attenuation of the surface albedo (Fig. 2.3c) ranges from a maximum of

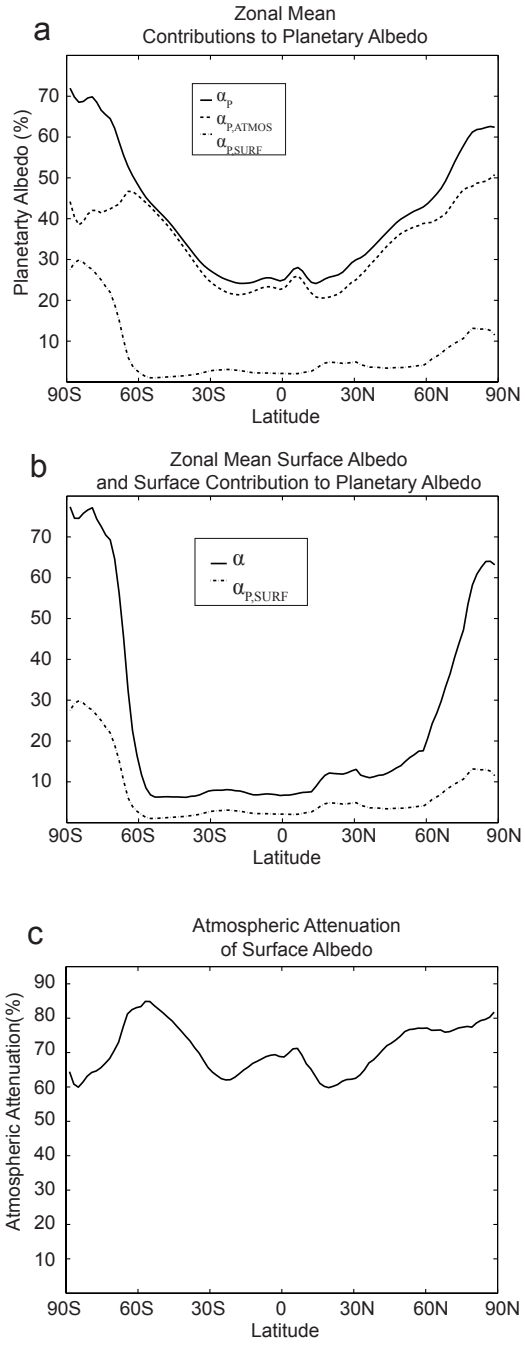

Figure 2.3: (a) Zonal mean planetary albedo partitioned between atmospheric and surface components. (b) Zonal mean surface albedo (a) and $\alpha_{P,SURF}$. (c) Atmospheric attenuation of surface albedo (χ).

80-85% in the storm tracks to a minimum of 60% in the dry subtropics. The meridional variations in atmospheric attenuation of surface albedo are small compared to the global mean atmospheric attenuation despite the large meridional variations in cloud properties; this is partly because solar radiation is attenuated by clear sky processes (i.e., solar atmospheric absorption) which contribute as much as 50% of the atmospheric attenuation in the global mean (Bony and coauthors, 2006).

In summary, over the observational period analyzed in this study, atmospheric processes are found to be the dominant (88%) contributor to global average planetary albedo while surface processes make a much smaller contribution to the global average planetary albedo.

2.3 Partitioning of planetary albedo in the models used in IPCC AR4

In this section, we look at the inter-model spread in planetary albedo in the pre-industrial (PI) simulations of the climate system performed using the climate models that were used in the IPCC AR4. We then employ the same methodology used in Section 2.2 to partition planetary albedo into its atmospheric and surface components. We find, not surprisingly, that the inter-model spread in planetary albedo is due to the differences in atmospheric processes and only weakly related to differences in surface albedo.

2.3.1 Model runs analyzed

We use data from the World Climate Research Programme's (WCRP) Coupled Model Intercomparison Project phase 3 (CMIP3) multi-model dataset: an archive of a suite of standardized coupled simulations from 25 global climate models that were included in the International Panel on Climate Change's Fourth Assessment Report (https://esgcet.llnl.gov:8443/index.jsp). The set of model simulations is commonly referred to as the WCRP's CMIP3 multi-model dataset (Meehl et al., 2007). We use output from the pre-industrial (PI) simulations which are forced with temporally invariant external forcing (CO_2 is set to 280 ppm). We use data from 15 coupled models that provided the output fields required for our analysis (Table 2.3).

Abbreviation	Full Name	Horizontal Resolution	Vertical Resolution
BCCR-BCM2.0	Bjerknes Centre for Climate Research, University of Bergen, Norway	T63	L31
CCCMA-CGCM3.1	Canadian Centre for Climate Modeling and Analysis, Canada	T47	L31
CNRM-CM3	Meteo-France/Centre National de Recherches Meteorologique, France	T63	L45
CSIRO-MK3.0	Australian Commonwealth Scientific and Research Organization (CSIRO), Australia	T63	L18
GFDL-CM2.0	NOAA/Geophysical Fluid Dynamics Laboratory, USA	2.0° X 2.5°	L24
GISS-ER	NASA/Goddard Institute for Space Studies, USA	4° X 5°	L20
IAP-FGOALS	National Key Laboratory of Numerical Modeling for Atmospheric Sciences and Geophysical Fluid Dynamics (LASG), China	T42	L26
MPI-ECHAM5	Max Planck Institute for Meteorology, Germany	T63	L31
INM-CM3.0	Institute for Numerical Mathematics, Russia	4° X 5°	L21
IPSL-CM4.0	Institute Pierre Simon Laplace, France	2.5° X 3.75°	L19
Micro3.2 (Hires)	National Institute for Environmental Studies, and Frontier Research Center for Global Change, Japan	T106	L56
MRI-CGCM2.3.2a	Meteorological Research Institute, Japan	T42	L30
NCAR-CCSM3.0	National Center for Atmospheric Research, USA	T85	L26
UKMO-HADCM3	Hadley Centre for Climate Prediction and Research/Met Office, UK	2.5° X 3.8°	L19
MIUB-ECHOg	University of Bonn, Germany	T30	L19

Table 2.3: Models used in this study and their resolution. The horizontal resolution refers to the latitudinal and longitudinal grid-spacing or the spectral truncation. The vertical resolution is the number of vertical levels.

2.3.2 Results

Averaged over all the CMIP3 models, the global average planetary albedo is 0.304 (Table 2.2). This value is within the range of observational estimates based on the corrected ERBE data (0.313 and CERES data (0.298). (See Fasullo and Trenberth (2008a,b) and Loeb et al. (2009) for a thorough discussion of the different satellite data sets and their uncertainties). The inter-model spread (two standard deviations) in planetary albedo is 0.016 corresponding to a TOA net shortwave difference of approximately 5.5 W m^{-2}across the models. Averaged across the models, $\alpha_{P,ATMOS}$ contributes 87% of the global average planetary albedo which agrees with the observed partitioning of global average planetary albedo between atmospheric and surface processes.

As is true of the observations, the two hemispheres contribute nearly equally to the global average planetary albedo in the models (spread on the ordinate of Fig. 2.4). Also in agreement with the observations, $\alpha_{P,SURF}$ contributes slightly more to the hemispheric average planetary albedo in the NH than in the SH (the offset on abscissa of Fig. 2.4b between the NH and SH data).

The inter-model spread in hemispheric average $\alpha_{P,ATMOS}$ (2σ=0.022) is approximately twice as large as that of $\alpha_{P,SURF}$ (2σ=0.012). Overall, the inter-model spread of hemispheric average planetary albedo is well correlated with the inter-model spread in hemispheric average $\alpha_{P,ATMOS}$ (Fig. 2.4a, R^2 = 0.53 and 0.71 in the NH and SH); it is not correlated with the hemispheric average $\alpha_{P,SURF}$ (Fig. 2.4b). The hemispheric average planetary albedo is poorly correlated with the hemispheric average $\alpha_{P,SURF}$ because the spread in hemispheric average $\alpha_{P,SURF}$is small compared to the spread in $\alpha_{P,ATMOS}$. Furthermore, the inter-model spread in $\alpha_{P,ATMOS}$ and $\alpha_{P,SURF}$ are negatively correlated as expected from Eq. 2.5 and discussed later in this section.

The large inter-model spread in global and hemispheric average planetary albedo is primarily due to atmospheric processes as opposed to surface albedo for three reasons: (1) the climatological planetary albedo is primarily (87%) determined by atmospheric reflection; (2) the surface albedo contribution to planetary albedo is strongly attenuated by the

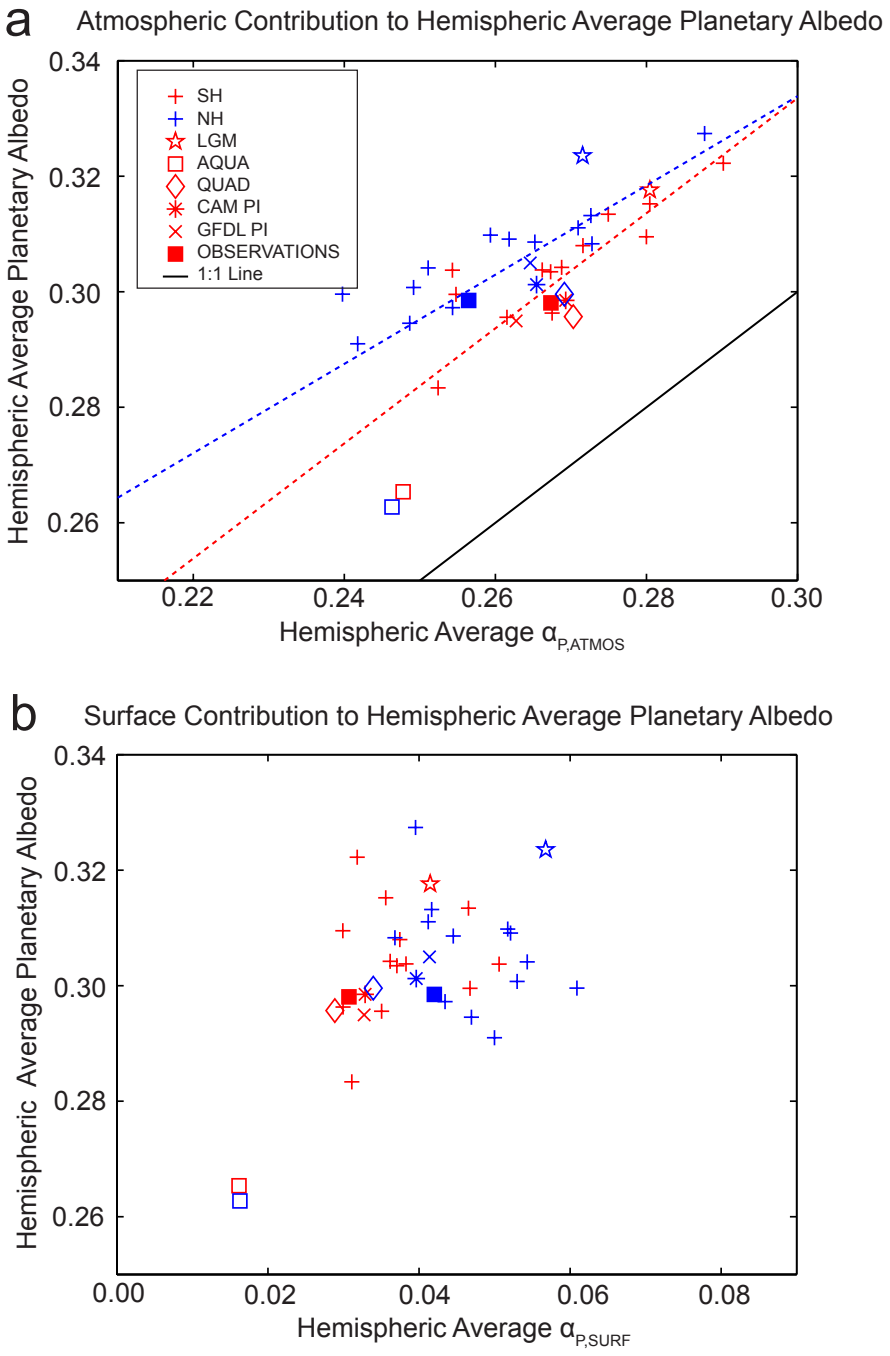

Figure 2.4: (a) Hemispheric average planetary albedo versus hemispheric average $\alpha_{P,ATMOS}$ in the CMIP3 PI simulations (crosses), observations (filled squares), and altered climate states. Red symbols and lines are for the Southern Hemisphere (SH) while blue denotes the Northern Hemisphere (NH). The dashed lines are linear best fits to the PI simulations and the solid line is the 1:1 line with zero intercept. (b) as in (a) except plotted against hemispheric average $\alpha_{P,SURF}$.

atmospheric opacity; and (3) a portion of the inter-model spread in surface albedo is a consequence of the inter-model spread in atmospheric opacity. As a consequence, the hemispheric average *surface albedo* is very weakly correlated with hemispheric average planetary albedo (R^2 is 0.03 in the NH and 0.12 in the SH Fig. 2.5) despite the relatively large inter-model spread in hemispheric average surface albedo ($2\sigma = 0.022$ in the NH and 0.036 in the SH).

The spatial map of the inter-model average planetary albedo is very similar to that observed except in Saharan Africa, the Arabian Peninsula, and the subtropical stratocumulus regions (not shown); in these regions, the models are biased low (the difference exceeds 2σ) compared to the observations. This bias exceeds the observational uncertainty in planetary albedo over those regions (Loeb et al., 2009). The inter-model spread in planetary albedo is greatest in the mid-latitude storm track regions over the country-regionNorth Atlantic, North Pacific, and Southern Ocean and in the cryosphere regions of both Hemispheres (not shown).

The zonal and annual average surface albedo, planetary albedo, $\alpha_{P,ATMOS}$, and $\alpha_{P,SURF}$ for each member of the CMIP3 PI ensemble are co-plotted (dashed black lines) in Fig. 2.6a-d alongside the observations (light blue lines). (Results from some additional model experiments are also shown in Fig. 2.6 and will be discussed in Section 2.4.) In agreement with the observations, the $\alpha_{P,ATMOS}$ in the CMIP3 ensemble is larger than $\alpha_{P,SURF}$ at all latitudes with the exception of the high Arctic and Antarctic (c.f. the bottom two panels of Fig. 2.6) . The meridional structure of surface albedo is consistent with the observations. However, there are substantial differences between models in annual average surface albedo, especially in the cryosphere regions as discussed in Roesch (2006).

The zonal average planetary albedo (Fig. 2.6b) exhibits substantial inter-model spread, exceeding 0.08 units (2σ) in the high latitudes (Fig. 2.7), which is attributed to differences in $\alpha_{P,ATMOS}$ in our analysis. Only in the high polar regions does $\alpha_{P,SURF}$ contribute significantly to the inter-model spread in planetary albedo (Fig. 2.7). This result suggests that model differences in the meridional structure of planetary albedo are primarily determined by atmospheric (cloud) processes and only weakly by inter-model differences in

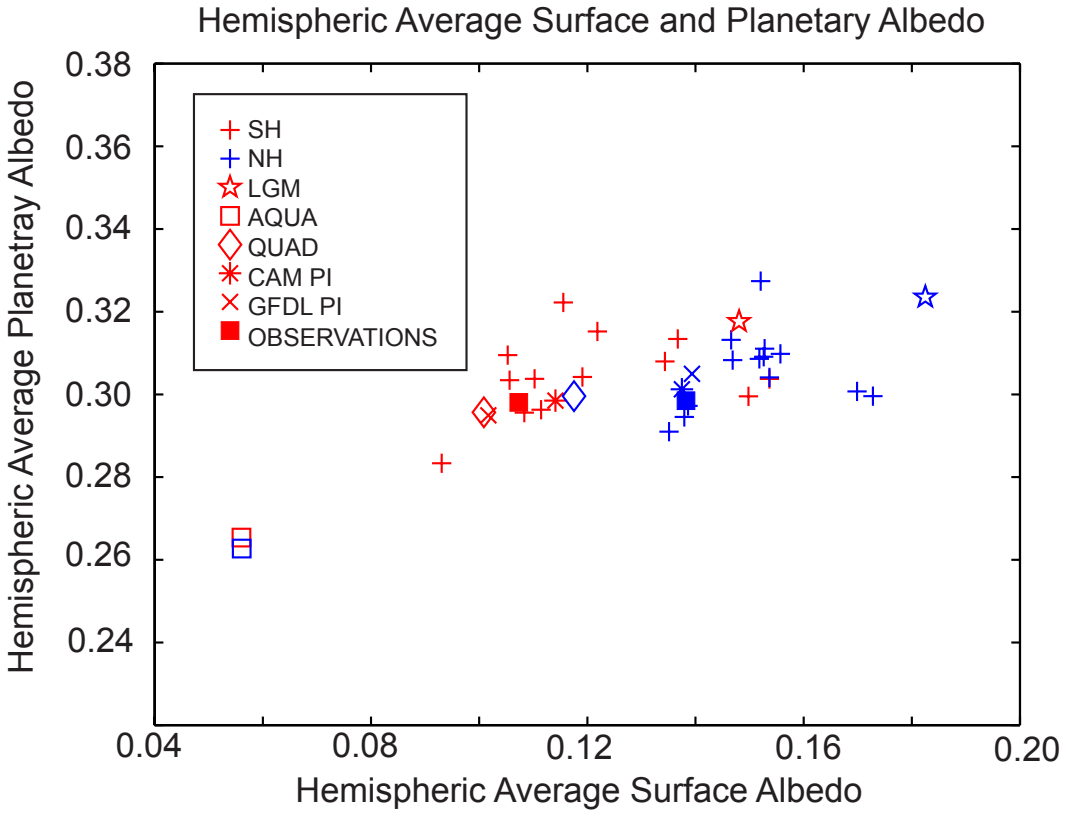

Figure 2.5: Hemispheric average planetary albedo versus hemispheric average surface albedo in the PI CMIP3 simulation (crosses), observations (filled squares), and altered climate states. Red symbols and lines are for the Southern Hemisphere (SH) while blue denotes the Northern Hemisphere (NH). The axes have a 1:1 ratio.

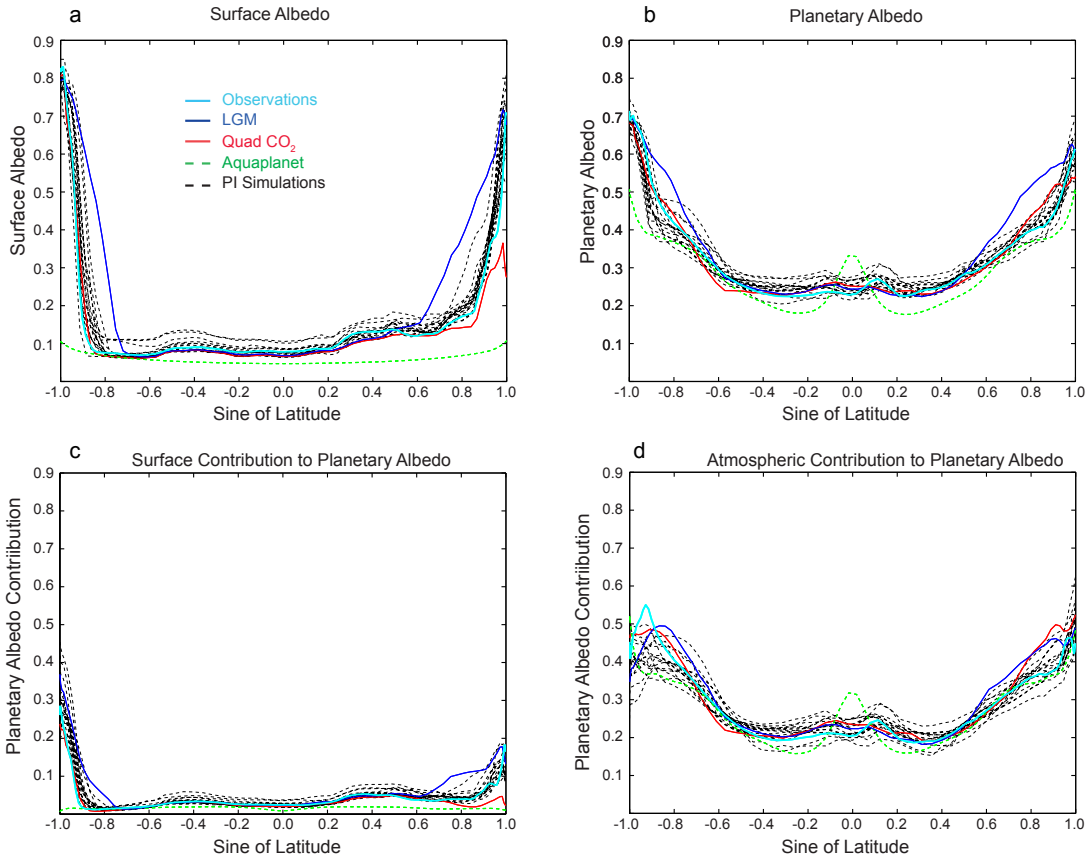

Figure 2.6: Zonal annual mean (a) surface albedo, (b) planetary albedo, (c) $\alpha_{P,SURF}$ and (d) $\alpha_{P,ATMOS}$ in the PI simulations from the CMIP3 models (dashed black lines). Also shown are the observations (solid, light blue) and model simulations of altered climate states (colored lines).

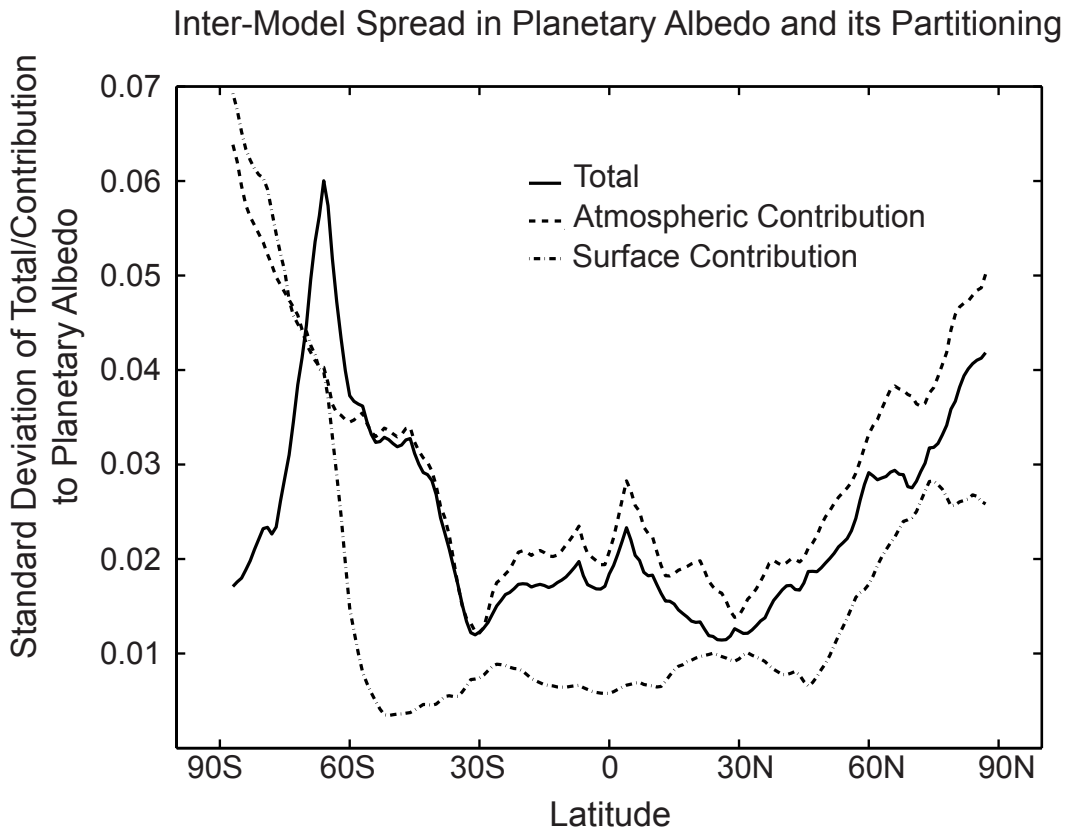

Figure 2.7: The inter-model standard deviation of zonal average planetary albedo (solid line), $\alpha_{P,ATMOS}$ (dashed line), and $\alpha_{P,SURF}$ (dashed-dot line) for the CMIP3 PI simulations.

surface processes.

With the exception of the SH ice margin, the inter-model standard deviation of $\alpha_{P,ATMOS}$ exceeds the total inter-model standard deviation of planetary albedo (Fig. 2.7); this result is a consequence of the negative correlation between $\alpha_{P,ATMOS}$ and $\alpha_{P,SURF}$ (not shown) that was also noted above. The negative correlation is expected based on our solar radiation model (i.e., Eq. 2.5); if two models had identical surface albedo in the country-regionArctic but different cloud reflectance (and hence atmospheric transmissivities) the model with the larger atmospheric reflectance would have a reduced $\alpha_{P,SURF}$ because the reflective surface

is less visible from the TOA. This result is interesting because it suggests that a portion of the inter-model spread in $\alpha_{P,SURF}$ is due to atmospheric variability across models as opposed to the inter-model spread of surface albedo.

2.4 Planetary albedo in simulations of altered climate states

In this section, we analyze the change in planetary albedo and its partitioning between surface and atmospheric processes due to a doubling of carbon dioxide from the pre-industrial values and in climate states with severely altered surface albedo distributions.

2.4.1 Carbon dioxide doubling experiments

2.4.1.1 Model runs used

Here we analyze the output from the "1pctto2x" simulations in the CMIP3 archive (Meehl et al., 2007). The initial conditions for each model come from the equilibrated pre-industrial (PI) simulations. Atmospheric CO_2 is increased at 1% per year until CO_2 has doubled relative to the PI concentration (70 years). The simulations are then run forward for an additional 150 years with carbon dioxide fixed at twice the PI concentration. We average the model output over the last 20 years of these simulations (years 201-220) and compare the climatological fields to their counterparts in that model's PI simulation. Theses runs will be referred to as the $2XCO_2$ and PI runs respectively.

2.4.1.2 Results

Averaged across all models, the doubling of CO_2 results in a reduction in the hemispheric average planetary albedo of -0.007$\pm$0.009 in the NH and -0.004 $\pm$0.009 in the SH; the range quoted is two standard deviations. The inter-model spread in the change of hemispheric average planetary albedo is strongly correlated with the change in $\alpha_{P,ATMOS}$ in both hemispheres (Fig. 2.8a) with an R^2 value of 0.91 in the NH and 0.96 in the SH (both significant at the 99% confidence interval). In contrast, the hemispheric average $\alpha_{P,SURF}$ change is not significantly correlated with the change in planetary albedo in either hemisphere (Fig.

2.8b). This is primarily because the inter-model spread in hemispheric average $\alpha_{P,ATMOS}$ change is approximately three times as large of that in $\alpha_{P,SURF}$. Although the change in hemispheric average $\alpha_{P,SURF}$ is negative in all models (abscissa of Fig. 2.8b) due to decreasing ice and snow cover, the inter-model spread in the $\alpha_{P,ATMOS}$ overwhelms the change in surface contribution resulting in a total planetary albedo feedback that is ambiguous in sign amongst the ensemble members. This result is in qualitative agreement with the conclusion of Kato et al. (2006) that the recent decline in Arctic sea ice has a negligible signature on the Arctic radiative budget at the TOA due to atmospheric attenuation and uncertainty in cloud feedbacks.

The change in hemispheric average $\alpha_{P,SURF}$ in the $2XCO_2$ runs is well correlated with the change is hemispheric average surface albedo (Fig. 2.9a, R^2 of 0.77 in the NH and 0.87 in the SH). This result can be understood by differentiating Eq. 2.5 with respect to α, R, and A:

$$\Delta(\alpha_{P,SURF}) = \frac{(1-R-A)^2}{(1-R\alpha)}\left(1+\frac{R\alpha}{1-R\alpha}\right)\Delta\alpha - \frac{2\alpha(1-R-A)}{1-R\alpha}\Delta A - \frac{\alpha(1-R-A)}{1-R\alpha}\left(2-\alpha\frac{1-R-A}{1-R\alpha}\right)\Delta R. \tag{2.8}$$

Eq. 2.8 highlights that changes in $\alpha_{P,SURF}$ are functions of both surface and atmospheric state; even if surface albedo remains constant in an altered climate state, the surface albedo contribution to planetary albedo could change by virtue of an atmospheric opacity change. Nonetheless, the changes in $\alpha_{P,SURF}$in the $2XCO_2$ runs are dominated by the first term on the r.h.s of Eq. 2.8 because the fractional changes in α are much larger than the fractional changes in either R or A (not shown). Furthermore, because both R and α are less than unity, $\frac{R\alpha}{1-R\alpha}\langle\langle 1$, Eq. 2.8 can be approximated by

$$\Delta(\alpha_{P,SURF}) \approx \frac{(1-R-A)^2}{(1-R\alpha)}\Delta\alpha \equiv (1-\chi)\Delta\alpha. \tag{2.9}$$

Eq. 2.9 neglects how changes in atmospheric opacity and changes in multiple reflections impact $\alpha_{P,SURF}$. It predicts that the changes in planetary albedo due to surface reflections

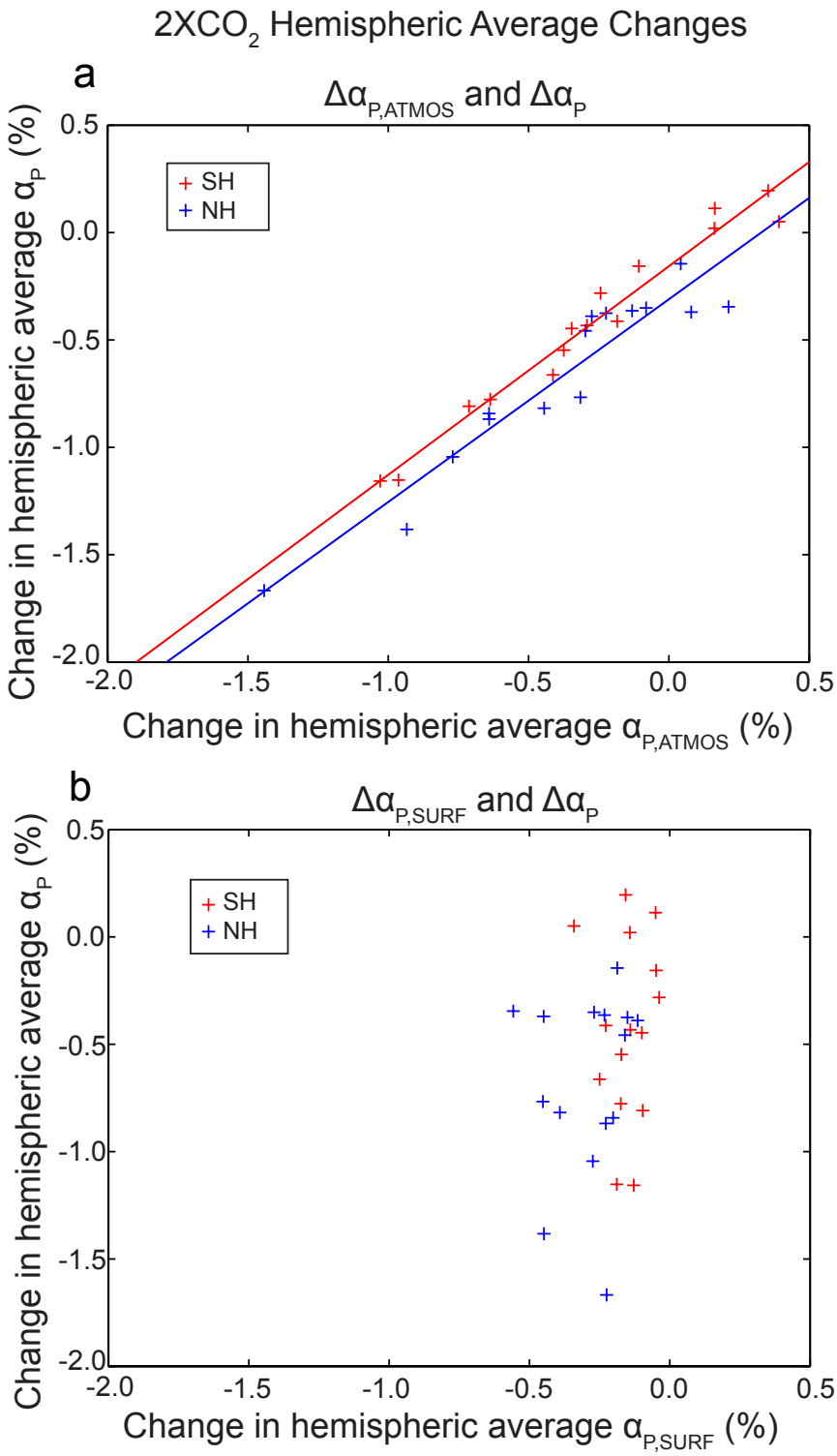

Figure 2.8: (a) Change in hemispheric average planetary albedo in the $2XCO_2$ runs (relative to the PI simulations) versus change in hemispheric average $\alpha_{P,ATMOS}$. The lines are the linear best fits in each hemisphere. (b) as in (a) except versus hemispheric average $\alpha_{P,SURF}$.

are equal to the change in surface albedo modified by the atmospheric attenuation of surface albedo in the mean climate. If all climate models had the same atmospheric attenuation of surface albedo (and Eq. 2.9 held perfectly), then we would expect the change in $\alpha_{P,SURF}$ in the $2XCO_2$ to be proportional to $\Delta\alpha$ with a slope equal to (1-χ). The strong correlation in Fig. 2.9a indicates that the models have a similar atmospheric attenuation of surface albedo and that inter-model spread in the surface albedo feedback is primarily driven by model differences in the surface albedo response to warming. This result is in qualitative agreement with the conclusion of Qu and Hall (2005) that the surface albedo feedback spread in climate models is due to spread in the simulated surface albedo changes and not in the inter-model spread of how surface albedo changes contribute to $F{\downarrow}_{TOA}$. The slope of the best fit lines in Fig. 2.9a are 0.34 in the NH and 0.30 in the SH suggesting that the change in planetary albedo associated with a change in surface albedo is approximately one third of the magnitude of the change in surface albedo. This result is at odds with Qu and Hall's (2005) finding that the change in planetary albedo per unit change in surface albedo is approximately one half. We have replicated Qu and Hall's result using their method on the data sets considered in this study suggesting the different quantitative conclusions are a consequence of methodological differences. The sensitivity of the atmospheric attenuation of surface albedo to the assumptions made in our simplified radiative transfer model (Fig. 2.1) is further discussed in Appendix B.

Fig. 2.9b shows that there is no correlation between the change in planetary albedo and the change in surface albedo, averaged over a hemisphere. This is a consequence of the atmospheric opacity attenuating the contribution of surface albedo changes to $F{\downarrow}_{TOA}$ and the large inter-model spread in changes in atmospheric (cloud) reflectivity. This result suggests that changes in surface albedo associated with poleward retreat of the cryosphere relative to its location in the present day climate are a poor predictor of changes in planetary albedo because the shortwave cloud feedback uncertainties exert a more profound influence on the $F{\downarrow}_{TOA}$ than the direct radiative forcing of the surface albedo. These results agree with Trenberth and Fasullo (2009) who found that decreases in planetary albedo in the

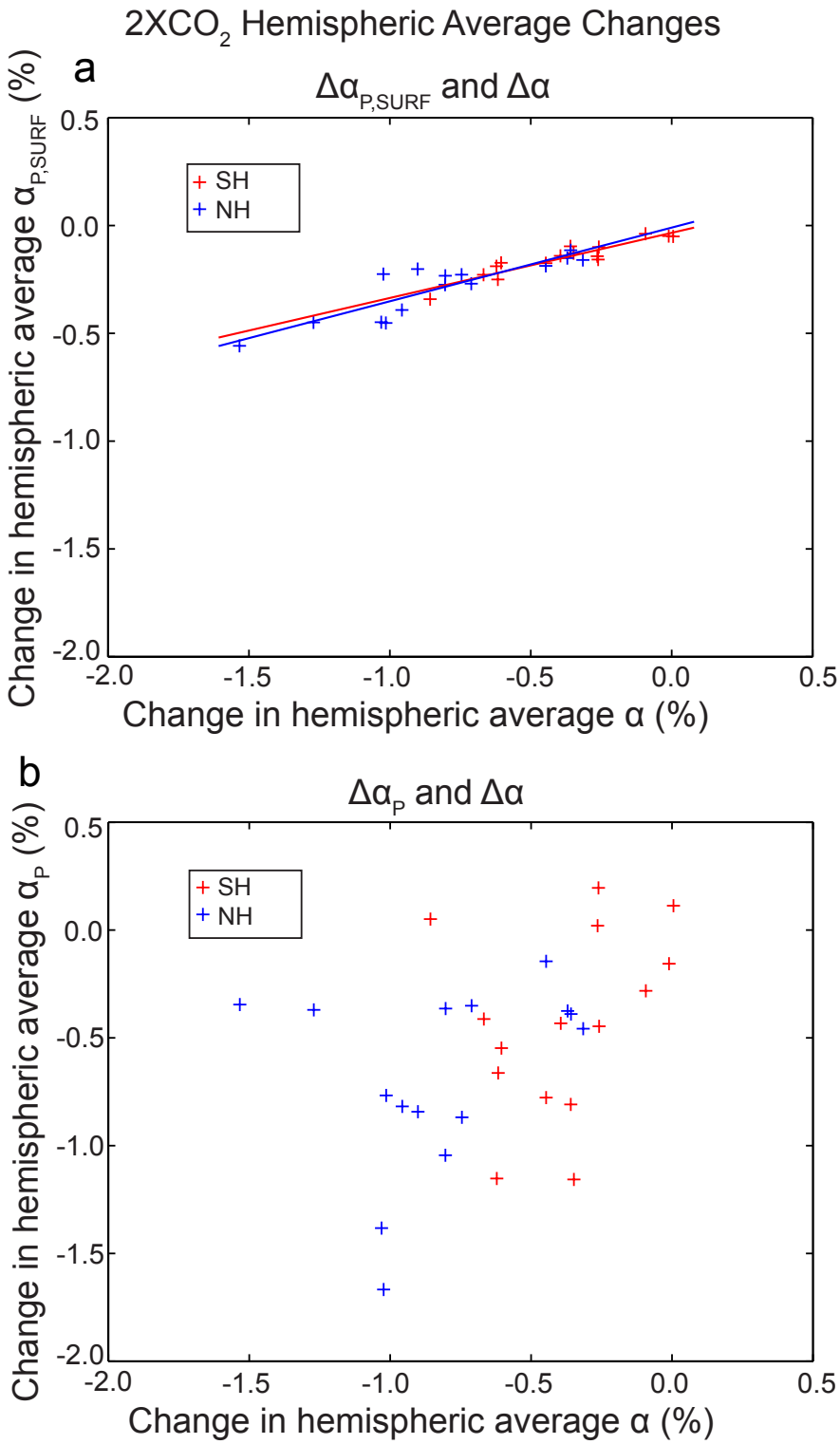

Figure 2.9: (a) Change in hemispheric average $\alpha_{P,SURF}$ in the $2XCO_2$ runs (relative to the PI simulations) versus change in hemispheric average surface albedo. The lines are the linear best fits in each hemisphere. (b) Change in hemispheric average planetary albedo in the $2XCO_2$ runs (relative to the PI simulations) versus change in hemispheric average surface albedo.

CMIP3 ensemble simulations for the A1B and A2 CO_2 emission scenarios are primarily a consequence of reduced cloud cover.

2.4.2 Simulations with specified surface albedo distributions

In this section, we explore the relationship between surface albedo and planetary albedo in models of radically different climates that feature severely altered spatial patterns of surface albedo.

2.4.2.1 Model runs used

We consider three greatly different climate states: the Last Glacial Maximum (LGM), the equilibrated climate under four times the PI CO_2concentration (QUAD), and an aquaplanet (AQUA) with no sea ice. The LGM simulation is performed with NCAR's CAM3 at a resolution of T42; it is forced with glacial orbital parameters and greenhouse gas concentrations, specified land ice albedo and topography and with sea ice concentrations and sea surface temperatures prescribed from the output of a fully coupled simulation of the LGM (see Li and Battisti, 2008, for a description). The QUAD simulation is also performed with CAM3 at a resolution of T42 with the greenhouse gas concentrations fixed at 1000 ppm and with sea surface temperatures, sea ice concentrations and snow extent prescribed as the output of an equilibrated coupled simulation. The LGM and QUAD runs are compared to a T42 CAM3 PI industrial run (the asterisk in Fig.s 2.5,2.6, and 2.9) as opposed to the T63 coupled CCSM3 PI run that is included in the CMIP3 ensemble. The AQUA simulation is performed with GFDL AM2 coupled to a 50 meter depth slab ocean and sea ice formation is prohibited even if the temperature drops below the freezing point (this run is identical to Kang et al. (2008), except with a 50m slab ocean). All simulations are run for 50 years and we average the output over the last 20 years of a single ensemble member of each simulation. The AQUA simulation is compared to the fully-coupled PI simulation included in the CMIP3 multi-model ensemble.

The prescribed spatial distribution of surface albedo varies widely in these runs (Fig.

2.6a and Fig. 2.10). The AQUA climate has almost no meridional gradient in surface albedo. (The small gradient in surface albedo is due to the angle of incidence dependence of ocean albedo). Relative to the control PI climate simulated by the same model, the QUAD climate has a reduced high latitude surface albedo due to a poleward shift in the ice edge while the LGM run has greatly enhanced surface albedo in the NH mid-latitudes mainly due to the presence of large continental ice sheets.

2.4.2.2 Results

While the changes in sea ice extent and in the distribution of land ice in the altered climate states greatly affect the surface albedo, the changes in planetary albedo are much smaller than the changes in surface albedo (Fig. 2.6 and Fig. 2.10). For example, in the LGM simulations the surface albedo in the mid-latitude NH increased by 0.25 (from ≈ 0.15 in the PI simulation to ≈ 0.40 in the LGM experiment), but the planetary albedo only increased by 0.10 relative to the PI simulations due to a 0.06 increase in $\alpha_{P,SURF}$ and a 0.04 increase in $\alpha_{P,ATMOS}$ (Fig. 2.10, the latter is due to more persistent clouds over the continental ice sheets).

In the global average, the planetary albedo increases from 0.300 in the PI to 0.320 in the LGM and is partitioned into a 0.012 increase in $\alpha_{P,SURF}$ and a 0.008 increase in $\alpha_{P,ATMOS}$ (Table 2.4.2.2). The global average surface albedo increase of 0.040 exceeds the $\alpha_{P,SURF}$ change by more than a factor of three, again suggesting that the impact of surface albedo changes on the TOA are attenuated by a factor of approximately three by atmospheric opacity. These results are in close agreement with T07 who found that the surface albedo changes over the ice sheets alone accounted for a 0.008 and 0.007 change in global average planetary albedo in two different simulations of the LGM. Our global average $\alpha_{P,SURF}$ changes also include changes in surface albedo away from the ice-sheets associated with a reduction in global sea level; we estimate this effect causes our global average $\alpha_{P,SURF}$ changes to be approximately 20% greater than that reported by T07.

In the AQUA simulation, the mid-latitude and high-latitude total planetary albedo and

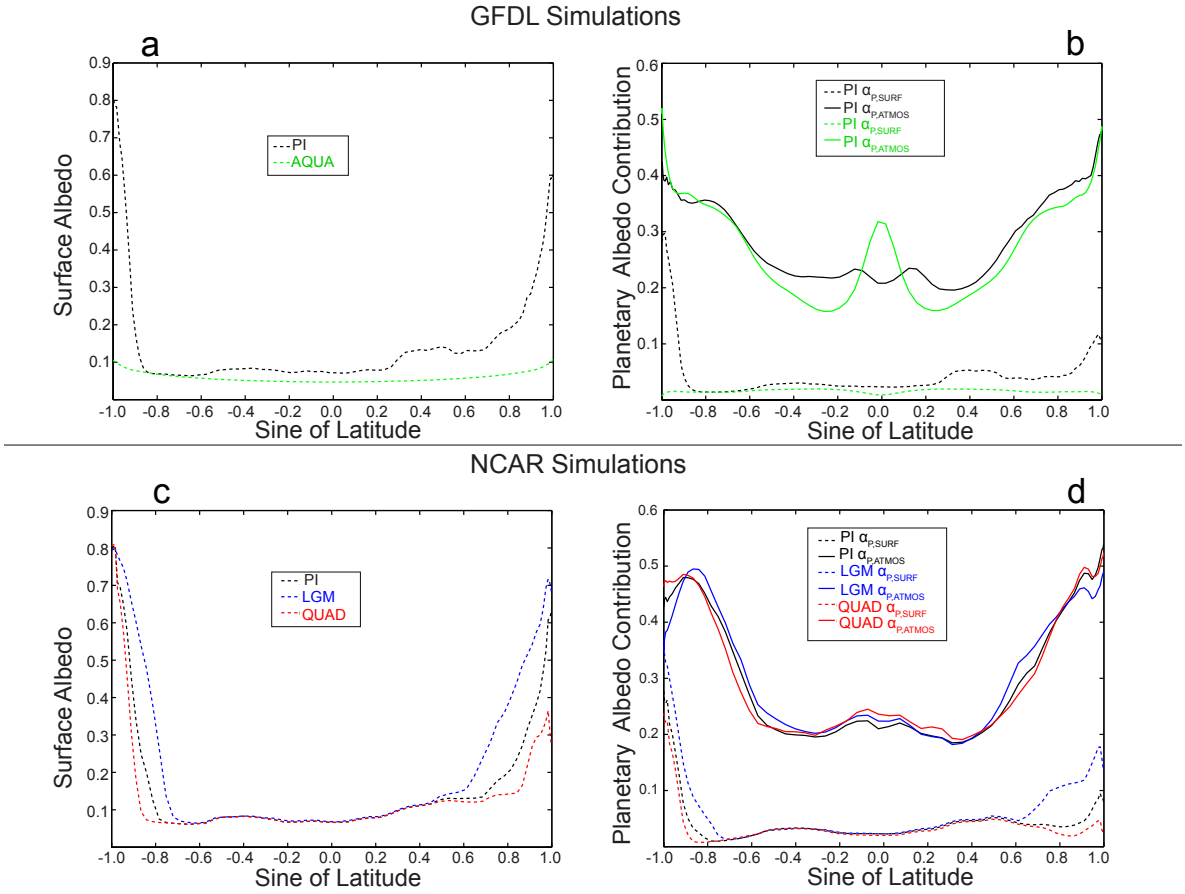

Figure 2.10: (a) Zonal average surface albedo in the GFDL simulations of the PI (black) and AQUA (green). (b) Zonal average $\alpha_{P,ATMOS}$, and $\alpha_{P,SURF}$ in the GFDL simulations of the PI (black) and AQUA (green). (c) and (d) as in (a) and (a) except for the NCAR simulations of the PI (black), QUAD (red), and LGM (blue).

Model /Hemisphere		Hemispheric Average Planetary Albedo (%)		
		Total	$\alpha_{P,ATMOS}$	$\alpha_{P,SURF}$
QUAD – PI	NH	-0.2	+0.4	-0.6
	SH	-0.3	+0.1	-0.4
LGM –PI	NH	+2.2	+0.6	+1.6
	SH	+1.9	+1.1	+0.8
AQUA – PI	NH	-4.2	-1.8	-2.4
	SH	-3.0	-1.5	-1.5
CMIP spread	NH	1.8	2.7	1.4
	SH	1.8	2.1	1.1

Table 2.4: Change in hemispheric average planetary albedo and the partitioning of the changes into atmospheric ($\alpha_{P,ATMOS}$) and surface ($\alpha_{P,SURF}$) contributions in the altered climate state simulations. Each difference is taken relative to the PI simulation in the same model used to simulate the altered climate state (and at the same resolution). The last two rows show the CMIP3 inter-model spread (2σ) of the same variables.

$\alpha_{P,SURF}$ decreases (relative to the PI simulations) by approximately one third of the surface albedo change in the same regions. In the global average, however, the decrease in planetary albedo (relative to the GFDL PI simulation) is due to nearly equal decreases in $\alpha_{P,SURF}$ and $\alpha_{P,ATMOS}$ (Fig. 2.4a and b and Table 1.4). Further inspection (Fig. 2.10b) shows that the decrease in hemispheric average $\alpha_{P,ATMOS}$ in the AQUA simulation is almost entirely due to reduced atmospheric reflection in the subtropics. This surprising result is due to differences in the seasonal migration of the inter-tropical convergence zone (ITCZ) between the AQUA and PI runs; the ITCZ is remains on the equator during all seasons in the AQUA simulation while the ITCZ migrates into the summer hemisphere in the PI simulation. This causes the subtropics to be cloudier during the sunny season in each hemisphere in the PI climate resulting in a larger annual average planetary albedo compared to the AQUA simulation in which the subtropics are relatively cloud free during all seasons.

It is worth discussing how the partitioning of planetary albedo in the altered climate

state experiments would change if our partitioning methodology was systematically underestimating $\alpha_{P,SURF}$ relative to the "true" surface contribution to planetary albedo; in this case, $\alpha_{P,ATMOS}$ would be biased high relative to its "true" value (by Eq. 2.6) especially over the cryospheric regions. If our $\alpha_{P,SURF}$ values were biased low, we would expect to see large changes in $\alpha_{P,ATMOS}$ co-located with the regions of large changes in surface albedo (and with the same sign as the surface albedo change). This does not occur. In the AQUA simulation, the changes in $\alpha_{P,ATMOS}$ are very small (except in the subtropics where the changes in surface albedo are also small, Fig. 2.10). In the QUAD simulation the changes in $\alpha_{P,ATMOS}$ and surface albedo have opposite signs in the cryosphere region; $\alpha_{P,ATMOS}$increases in the high latitudes where the surface albedo has decreased relative to the PI and LGM simulations with the same model (Fig. 2.10). Thus, the partitioning of planetary albedo in the altered climate states suggests that the $\alpha_{P,SURF}$ values calculated by our methodology are not biased low.

2.5 Summary and Discussion

We have partitioned the Earth's planetary albedo into a component due to the reflection of incoming radiation by objects in the atmosphere, $\alpha_{P,ATMOS}$, and a component due to reflection at the surface, $\alpha_{P,SURF}$. In the global average, the vast majority (88%) of the observed planetary albedo is due to atmospheric processes, $\alpha_{P,ATMOS}$. We demonstrate that the primary conclusions reached in this manuscript are robust to uncertainties in the observational data sets (Appendix A) and the assumptions made in our simplified radiative transfer model (Appendix B). The CMIP3 PI ensemble inter-model average planetary albedo is also primarily due to $\alpha_{P,ATMOS}$ (87%). The inter-model spread in global average planetary albedo is large, corresponding to radiative differences at the top of the atmosphere (2σ=5.5Wm^{-2}) that exceed the radiative forcing of doubling carbon dioxide. Inter-model differences in $\alpha_{P,ATMOS}$ explain the majority (>60%) of the inter-model spread in hemispheric average planetary albedo.

Surface albedo makes a small contribution to the global average planetary albedo because

atmospheric processes attenuate the contribution of surface albedo to planetary albedo by a factor of approximately three. The atmosphere attenuates $\alpha_{P,SURF}$ relative to the surface albedo because the atmosphere is somewhat opaque to solar radiation and thus attenuates the amount of shortwave radiation incident on the TOA that reaches the surface and the amount of shortwave radiation reflected at the surface that is transmitted back to the TOA. As a consequence, the CMIP3 PI ensemble inter-model spread in planetary albedo is poorly correlated with the spread in surface albedo despite considerable inter-model differences in surface albedo.

Surface albedo decreases with global warming ($2XCO_2$ runs) in all models but the magnitude of the change varies significantly. However, the inter-model spread in the change in surface albedo is poorly correlated with the change in planetary albedo. The planetary albedo changes associated with global warming were found to be primarily due to changes in cloud albedo (93% of the inter-model spread). This result is unsurprising given that cloud albedo plays the dominant role in setting the planetary albedo in the unperturbed climate and that the surface albedo's impact on the TOA radiative budget is strongly attenuated (approximately three-fold) by the atmosphere.

Experiments with prescribed and severely altered surface albedo distributions associated with the Last Glacial Maximum and an aquaplanet demonstrated that changes in $\alpha_{P,SURF}$ were approximately one third the magnitude of the surface albedo changes, due to atmospheric attenuation. Furthermore, the changes in planetary albedo in these experiments were due to nearly equal magnitude contributions from changes in cloud properties and the prescribed changes in surface albedo. This suggests that cloud feedbacks in greatly altered climate states are likely to play as important of a role in setting planetary albedo as even zeroth order changes in surface albedo (Eastman and Warren, 2010).

The most surprising result from this study is that the differences in planetary albedo in climates that have severely altered surface albedo are relatively modest compared to the spread in planetary albedo in the PI simulations of the CMIP3 models. For example, the difference in hemispheric average planetary albedo between the simulations of the PI

world and the LGM is less than the spread in the PI simulations using the CMIP3 models. Similarly, the CMIP3 ensemble average change in planetary albedo due to global warming in the $2XCO_2$simulations is less than 30% of the inter-model spread in simulations of the present day climate. These results follow because planetary albedo is largely determined by atmospheric processes (cloud reflection) and there are large inter-model differences in cloud distributions in simulations of the PI climate. In contrast, planetary albedo is largely insensitive to surface processes. Thus, changes in surface albedo make a small contribution to planetary albedo changes relative to the large uncertainties in cloud distribution changes.

Our analysis has focused on global and hemispheric average planetary albedo. We note that surface albedo, $\alpha_{P,SURF}$, and $\alpha_{P,ATMIS}$ changes associated with global warming and paleoclimate states have a spatially non-uniform structure, often peaking at the high latitudes. The meridional structure of planetary albedo is inextricably linked to the equator-to-pole temperature gradient and the total heat transport in the climate system (Stone, 1978) and these issues are explored in the next Chapter.

Chapter 3

WHAT DETERMINES MERIDIONAL HEAT TRANSPORT IN CLIMATE MODELS?

3.1 Introduction

The total meridional heat transport (MHT) in a steady state climate system is equal to the net radiative surplus integrated over the tropics or, equivalently, the net radiative deficit integrated over the extratropics (Vonder Haar and Oort, 1973). In this regard, the MHT is equal to the equator-to-pole contrast of absorbed solar radiation (ASR) minus the equator-to-pole contrast of outgoing longwave radiation (OLR). Therefore, any change in MHT must be accompanied by a change in the equator-to-pole contrast of ASR or OLR without compensating changes in the other quantity. The magnitude of the MHT varies greatly between the state of the art coupled climate models (Lucarini and Ragone, 2011). In this Chapter we demonstrate that the inter-model spread in MHT in the models used for the IPCC's fourth assessment (International Panel on Climate Change [Solomon et al., 2007) is due to inter-model differences in the equator-to-pole contrast of ASR. We then explore the processes that control the equator to pole contrast of ASR, its variability amongst climate models, and its impact on MHT.

In a seminal paper, Stone (1978) calculated that approximately two thirds of the observed equator-to-pole contrast in ASR is due to the Earth-Sun geometry and the resulting meridional distribution of incident solar radiation at the top of the atmosphere (TOA) and the remaining one third is due to the equator-to-pole contrast in planetary albedo. Stone emphasized that the latter component was nearly energetically balanced by the equator-to-pole contrast in outgoing longwave radiation (OLR) such that the equator-to-pole contrast in net radiation was equal to the ASR contrast associated with the meridional distribution of incident radiation. Subsequent work by Enderton and Marshall (2009) demonstrated

that this result is not supported by modern observations or in climate model simulations. Enderton and Marshall (2009) found that approximately 35% of the observed equator-to-pole contrast in ASR in the Northern Hemisphere and 40% in the Southern Hemisphere is due to the equator-to-pole contrast in planetary albedo and that climate states with altered meridional distributions planetary albedo exhibit very different strengths of atmospheric and oceanic circulation (e.g., different MHT).

Partitioning of the equator-to-pole contrast in ASR into components associated with the incident radiation (the orbital geometry) and planetary albedo is useful because, while the former is externally forced, the latter is a strong function of the climate state and thus may provide important feedbacks when external forcing changes. More important, while the equator-to-pole contrast in incident solar radiation varies by approximately 5% over the entire obliquity cycle, there is little *a priori* constraint on the possible range of the equator-to-pole contrast in planetary albedo. Thus, a small perturbation in the external forcing may produce a disproportionately large change in the equator-to-pole contrast in ASR via changes in the meridional structure of planetary albedo (i.e., changes in cloud or snow/ice cover) associated with the *response* of the climate system. Hence, an assessment of the sources that contribute to the meridional distribution of planetary albedo is a prerequisite for understanding how and why the atmospheric and oceanic circulation (the MHT) will respond to external forcing.

The Earth has a pronounced equator-to-pole contrast in surface albedo due to latitudinal gradients in the fraction of area covered by ocean and land, the latitudinal gradients in land vegetation, and the spatial distribution of land and sea ice (Robock, 1980). The contribution of the equator-to-pole contrast in surface albedo to the equator-to-pole contrast in planetary albedo is still an unresolved question in climate dynamics, however, because there is considerable attenuation of the surface albedo by the atmosphere. While simplified energy balance models (EBMs) have often assumed that the local planetary albedo is a function of surface albedo only (i.e., Budyko, 1969; North, 1975), this assumption is unwarranted due to the atmosphere's influence on planetary albedo. Indeed, the step function change

of planetary albedo at the ice-edge specified by EBMs is inconsistent with the observed meridional structure of planetary albedo (Warren and Schneider, 1979) and more recent parameterizations of planetary albedo in EBMs have suggested that the atmosphere damps the influence of surface albedo on the top of atmosphere (TOA) radiative budget (Graves et al., 1993). Recent work by Donohoe and Battisti (2011a) has demonstrated that the vast majority of the global average planetary albedo is due to atmospheric as opposed to surface processes; this result suggests that the meridional gradient of planetary albedo and hence the *MHT* in the climate system may also be strongly dictated by atmospheric processes (i.e., by cloud properties).

This chapter is organized as follows. In Section 3.2, we present the inter-model spread of *MHT* in the coupled climate models used in the IPCC's fourth assesment report and how the spread in MHT relates to the equator-to-pole contrast of *ASR* and *OLR*. In Section 3.3, we diagnose the processes that determine the equator-to-pole contrast in ASR in the observations and the climate models. In Section 3.4, we examine the processes that control the inter-model spread in *OLR* and how these processes relate to equator-to-pole contrast of net radiation. We then extend this anaylsis to the change in *MHT* due to CO_2 doubling Section 3.4.3. A conclusion follows.

3.2 Meridional heat transport and the equator-to-pole contrast of absorbed solar radiation

In this section, we analyze the *MHT* in climate models and observations in terms of the equator-to-pole contrast of *ASR* and *OLR*. We demonstrate that the inter-model spread in peak *MHT* is largely determined by the equator-to-pole contrast of *ASR*.

3.2.1 Model runs and datasets used

We use data from the World Climate Research Programme's (WCRP) Coupled Model Intercomparison Project phase 3 (CMIP3) multi-model dataset: a suite of standardized coupled simulations from 25 global climate models that were included in the International Panel

Symbol	Meaning
MHT_{MAX}	Peak magnitude of meridional heat transport in each hemisphere
ASR^*	The equator-to-pole contrast in Absorbed Solar Radiation
OLR^*	The equator-to-pole contrast of Outgoing Longwave Radiation
x	Sine of latitude
a	Planetary co-albedo
S	Incident solar radiation
$\alpha_{P,ATMOS}$	Atmospheric contribution to planetary albedo
$\alpha_{P,SURF}$	Surface contribution to planetary albedo
ASR^*_{ATMOS}	The contribution of $\alpha_{P,ATMOS}$to ASR*
ASR^*_{SURF}	The contribution of $\alpha_{P,SURF}$to ASR*
$LWCF$	Longwave cloud forcing = OLR - OLR_{CLEAR}
f	Cloud fraction
C_{STRUC}	The contribution of cloud structure to OLR when clouds are present
OLR^*_{CLEAR}	Clear-sky OLR contribution to OLR*
OLR^*_{LWCF}	Contribution of LWCF to OLR*
$OLR^*_{LWCF,f}$	The contribution of cloud fraction anomalies to the inter-model spread in OLR*
$OLR^*_{LWCF,STRUC}$	The contribution of cloud structure anomalies to the inter-model spread in OLR*
TS^*	The equator-to-pole contrast of surface temperature
Q^*	The equator-to-pole contrast of vertically integrated specific humidity

Table 3.1: Variables used in this chapter.

on Climate Change's Fourth Assessment Report (https://esgcet.llnl.gov:8443/index.jsp). The set of model simulations is commonly referred to as the WCRP's CMIP3 multi-model dataset (Meehl et al., 2007). We use the pre-industrial (PI) simulations from the 15 coupled models that provided the output fields required for the analysis presented in this study (the same models used in Chapter 2 – Table 2.3). Each PI simulation is forced with temporally invariant external forcing (CO_2 is set to 280 ppm) and, in principle, represents an equilibrium climate that is in energy balance. In practice, both the global average and the local energy budgets are not balanced in the simulated climatologies (Lucarini and Ragone, 2011). Hence, we make corrections to balance the global annual mean radiative budget by adding a spatially and temporally invariant constant to the OLR field prior to performing the analysis[1]. All calculations reported here are based on solar weighted annual average fields.

The observational analysis makes use of the TOA and surface shortwave radiation data products from the Clouds and Earth's Radiant Energy System (CERES) experiment (Wielicki et al., 1996). We use long term climatologies of the CERES TOA data from Fasullo and Trenberth (2008a) that are corrected for missing data and global average energy imbalances. For the surface shortwave fluxes we use the CERES "AVG" fields which are derived by assimilating the satellite observations into a radiative transfer model to infer the surface fluxes (Rutan et al., 2001). All calculations are preformed separately for each of the four CERES instruments (FM1 and FM2 on Terra from 2000 -2005 and FM3 and FM4 on AQUA from 2002 – 2005). We then average the results over the four instruments.

3.2.2 Methodology for MHT calculation and definitions of ASR and OLR**

We determine the total (atmosphere plus ocean) zonally averaged MHT to the extratropics of each hemisphere by noting that, in an equilibrium climate, the net radiative deficit spatially integrated from latitude θ to the pole is exactly balanced by MHT into the region

[1]The only calculated field discussed here that is affected by this correction is the MHT; this correction ensures the global average heat transport divergence is zero and the resulting MHT is independent of whether the heat transport divergence is integrated from the South Pole to the North Pole or vice versa.

poleward of θ (Trenberth and Caron, 2001b; Fasullo and Trenberth, 2008b; Vonder Haar and Oort, 1973) :

$$MHT(\theta) = -2\pi R^2 \int_{x=\sin(\theta)}^{1} [ASR(x) - OLR(x)]\, dx, \tag{3.1}$$

where x is the sine of latitude. We gain insight into the processes that determine the *MHT* by decomposing the *ASR(x)* and *OLR(x)* into global averages (denoted by overbars) and spatial anomalies (defined as deviations from the global average and denoted by primes) and by setting the limit of integration to x_m=*sin*(θ_m), where θ_m is the latitude where the zonally averaged *ASR* and *OLR* are equal. Then Eq. 3.1 yields the maximum zonally averaged meridional heat transport (MHT_{MAX}):

$$MHT_{MAX} \equiv MHT(x_m) \tag{3.2a}$$

$$= -2\pi R^2 \int_{x=x_m}^{1} \left[ASR'(x) + \overline{ASR} - (OLR'(x) - \overline{OLR})\right] dx \tag{3.2b}$$

$$= -2\pi R^2 \int_{x(ASR'=OLR')}^{1} [ASR'(x) - OLR'(x)]dx \quad . \tag{3.2c}$$

Reduction to Eq. 3.2c relies on the fact that a steady climate system achieves global average radiative equilibrium:

$$\overline{ASR} = \overline{OLR} \quad . \tag{3.3}$$

Eq. 3.2 can be rewritten as

$$MHT_{MAX} \cong ASR^* - OLR^* \tag{3.4}$$

where

$$ASR^* = -2\pi R^2 \int_{x(ASR'=0)}^{1} ASR'dx \tag{3.5}$$

and

$$OLR^* = -2\pi R^2 \int_{x(OLR'=0)}^{1} OLR'(x)dx. \tag{3.6}$$

The near equality in Eq. 3.4 holds exactly if the meridional nodes of the *OLR'* and *ASR'* are co-located; in all calculations presented here the near equality holds to within 1% of the MHT_{MAX} (the average error in the approximation is 0.3%). Fig. 3.1 presents graphical representation for calculating MHT_{MAX} from Eq. 3.1 (Panel a) and from Eq. 3.4b by application of the definitions of ASR^* and OLR^* (Panels b and c respectively); the difference between the shaded areas in Panels b and c is equal to the shaded area (representing MHT_{MAX}) in Panel a.

The negative sign in Eqs. 3.5 and 3.6 are chosen so that the deficits in *ASR* and *OLR* over the extratropics render ASR^* and OLR^* as positive numbers. Eq. 3.5 and 3.6 are the *ASR* and *OLR* deficit (ASR^* and OLR^*) in the Northern Hemisphere (NH) extratropics; a similar expression with modified limits of integration holds for the Southern Hemisphere (SH). By definition, the sum of ASR^* in the two hemispheres is equal to the *ASR* surplus (relative to the global average) integrated over the tropics. Therefore, this quantity represents the difference between the radiaitve energy absorbed in the tropics and in the extratropics. In an equilbruim state, ASR^* must either be balanced radiatively by OLR^* or by a dynamic heat transport from the tropics to the extratropics (MHT_{MAX}). In this regard, ASR^* represents the equator-to-pole scale shortwave driving of the climate system and OLR^* and MHT_{MAX} are the radiative and dynamic responses to the solar forcing[2].

As a quantitative example, we calculate from the CERES data that ASR^* is 8.2 PW in the NH and that this deficit in *ASR* over the extratropics is balanced by a 2.4 PW deficit in OLR (OLR^*) and 5.8 PW of heat import via MHT_{MAX}. Similarly, in the SH extratropics an ASR* deficit of 9.0 PW is balance by a 3.2 PW deficit in OLR^* and 5.8 PW of MHT_{MAX} (Table 3.2).

---

[2] ASR^* is not a pure external forcing, but is itself a function of the climate system.

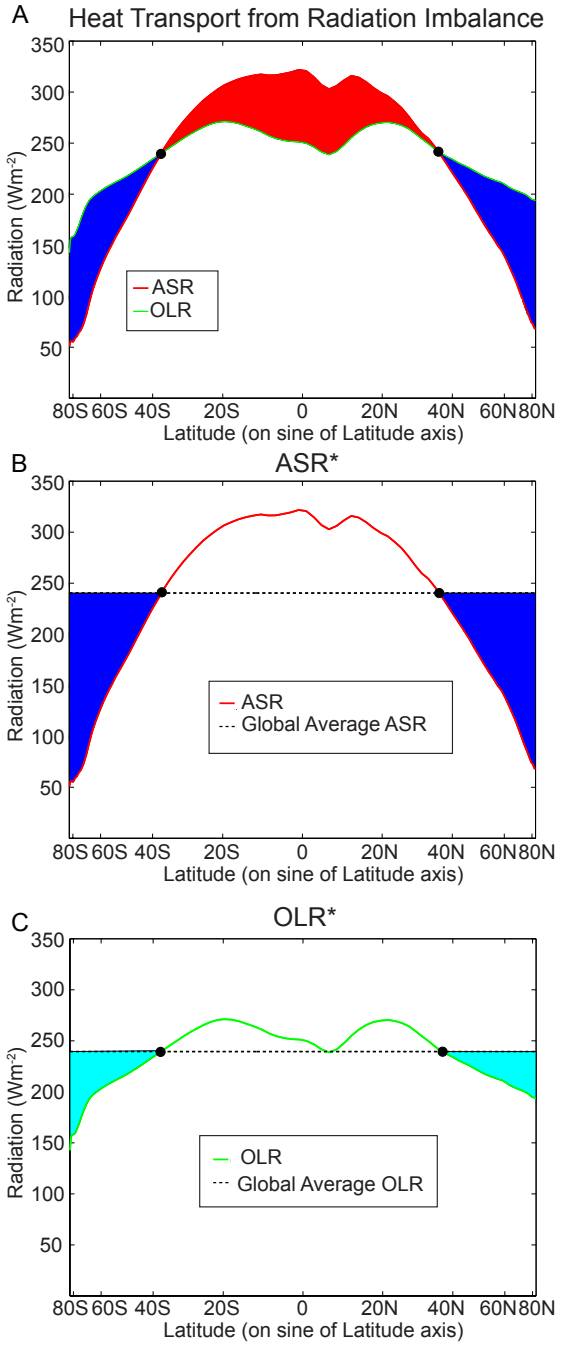

Figure 3.1: Graphical demonstration of the calculations of (a) the maximum meridional heat transport, $MHT_{MAX,}$ (b) ASR^*; and (c) OLR^* from the CERES annual average data. The x axis is the *sin* of latitude in all panels. (a) The zonal average ASR (red line) and OLR (green line). The blue (red) shaded area is the spatially integrated net radiative deficit (surplus) in the extra tropics (tropics) and equals the meridional heat import (export) from each region (MHT_{MAX}). (b) The zonal average ASR co-plotted with the global average ASR; the shaded area equals ASR^*. (c) As is (b) except for OLR and OLR^*. The black circles denote the latitude where $ASR' = 0$ in each hemisphere.

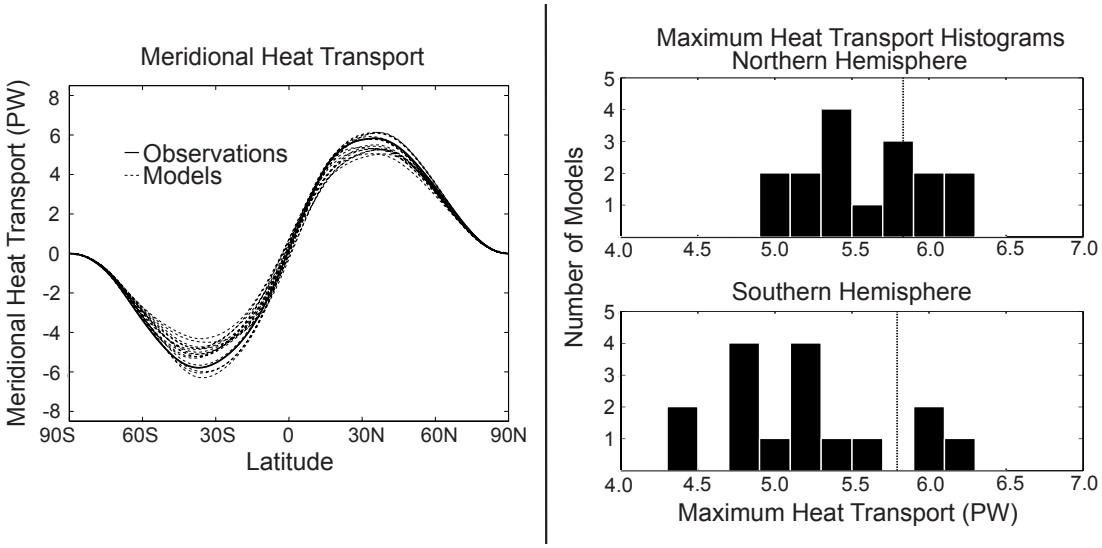

Figure 3.2: (a) Meridional structure of meridional heat transport for the observations (thick-solid line) and each of the CMIP3 PI simulations (thin-dashed lines). (b) Histogram of maximum heat transport (MHT_{MAX}) in the Northern Hemisphere. The observed value is shown by the dashed vertical line. (c) As in (b) except for the Southern Hemisphere.

3.2.3 Results

The CMIP3 models and the observations all have similar meridional structures of MHT (Fig. 3.2a) with a peak heat transport around 36° in each hemisphere. The structure and magnitude of the inter-model average MHT is in close agreement with the observational estimates of MHT in the NH[3] and has a peak value (MHT_{MAX}) of 5.6 PW (Table 3.2). The inter-model average MHT_{MAX} in the SH is 5.3 PW, which is 0.6 PW less than observed. MHT_{MAX} varies widely between models (Fig. 3.2b-c); the inter-model spread (defined throughout as two standard deviations – 2σ) in MHT_{MAX} is 0.8 PW in the NH and 1.1 PW in the SH. In the SH, the model with the largest MHT_{MAX} has approximately 50% more heat transport than the model with the smallest MHT_{MAX}.

The inter-model spread in $ASR*$ is 0.9 PW in the NH and 1.2 PW in the SH and

[3]The latter has uncertainties of approximately 20% at the latitude of peak heat transport (Wunsch, 2005).

(PW)	Total ASR^*	Incident	Net Albedo	Atmospheric	Surface	OLR^*	MHT_{MAX}
NORTHERN HEMISPHERE							
Observations	8.2	5.3	2.9	2.5	0.4	2.4	5.8
Model Average	8.1	5.2	2.9	2.4	0.5	2.6	5.5
Model Spread (2σ)	0.9	0.1	0.9	1.2	0.5	0.6	0.8
SOUTHERN HEMISPHERE							
Observations	9.0	5.3	3.7	3.5	0.2	3.2	5.8
Model Average	8.4	5.2	3.2	2.9	0.3	3.2	5.2
Model Spread (2σ)	1.2	0.1	1.2	1.4	0.4	0.5	1.1

Table 3.2: Total ASR^*, its partitioning into incident and net planetary albedo components (2^{nd} and 3^{rd} columns) by application of Eq. 3.10 and the subsequent partitioning of the planetary albedo component into atmospheric and surface contributions (4^{th} and 5^{th} columns) by application of Eq. 3.12. OLR^* and the MHT_{MAX} are also shown. The observations and CMIP3 multi-model average and spread (2 standard deviations) are shown for each hemisphere. All entries are in PWs.

is approximately twice the inter-model spread in OLR^* (0.5 PW in the NH and 0.6 PW in the SH). Inter-model differences in MHT_{MAX} are well correlated with the inter-model differences in ASR^* (Fig. 3.3a) with a R^2 value of in 0.57 the NH and 0.85 in the SH (Table 3.3), both significant at the 99% confidence interval. In contrast, MHT_{MAX} is not correlated with OLR^* in either hemisphere (Fig. 3.3b). We can understand this result as follows. The inter-model spread in MHT_{MAX} can be diagnosed from Eq. 3.4 and the statistics of OLR^* and ASR^*:

$$\sqrt{\left[\langle MHT_{MAX}\rangle^2\right]} = \sqrt{\left[\langle ASR^*\rangle^2\right] + \left[\langle OLR^*\rangle^2\right] - 2\left[\langle OLR^*\rangle \bullet \langle ASR^*\rangle\right]} \qquad (3.7)$$

where $\langle\ \rangle$s indicate the departure of the quantity from the inter-model average and the $[\ ]$ brackets are averages over all the models. Eq. 3.7 demonstrates that the inter-model spread in MHT_{MAX} is a consequence of the spread in $ASR*$, the spread in OLR^*, and the covariance between $ASR*$ and OLR^*. For example, in the limit that OLR^* and $ASR*$ are linearly independent, then the spread in MHT_{MAX} is the quadrature sum of the spread in $ASR*$ and OLR^*. In contrast, in the limit of perfect correlation between OLR^* and $ASR*$, with a regression coefficient of unity, there would be no spread in MHT_{MAX}, independent of how much OLR^* and $ASR*$ varies between the different models. These two limits correspond to what we will call the dynamic and radiative limits of the extratropical energy budget. In the dynamic limit, departures in ASR* and OLR* from the average across the models are uncorrelated and balanced by a departure in the MHT_{MAX}. In the radiative limit, the inter-model differences in ASR* are balanced by inter-model differences in OLR* and there is no inter-model spread in MHT_{MAX}.

The square root of the inter-model covariance of OLR^* and $ASR*$ is approximately the same magnitude as the spread in OLR^* and is significantly smaller than the spread in $ASR*$ (Table 3.3) suggesting that the CMIP3 models are closer to the dynamic limit than the radiative limit; inter-model anomalies in $ASR*$ and OLR^* only partially balance each other leading to a MHT_{MAX} spread that is comparable in magnitude to the $ASR*$ spread. We can understand the correlation of $ASR*$ and MHT_{MAX} and the lack of correlation

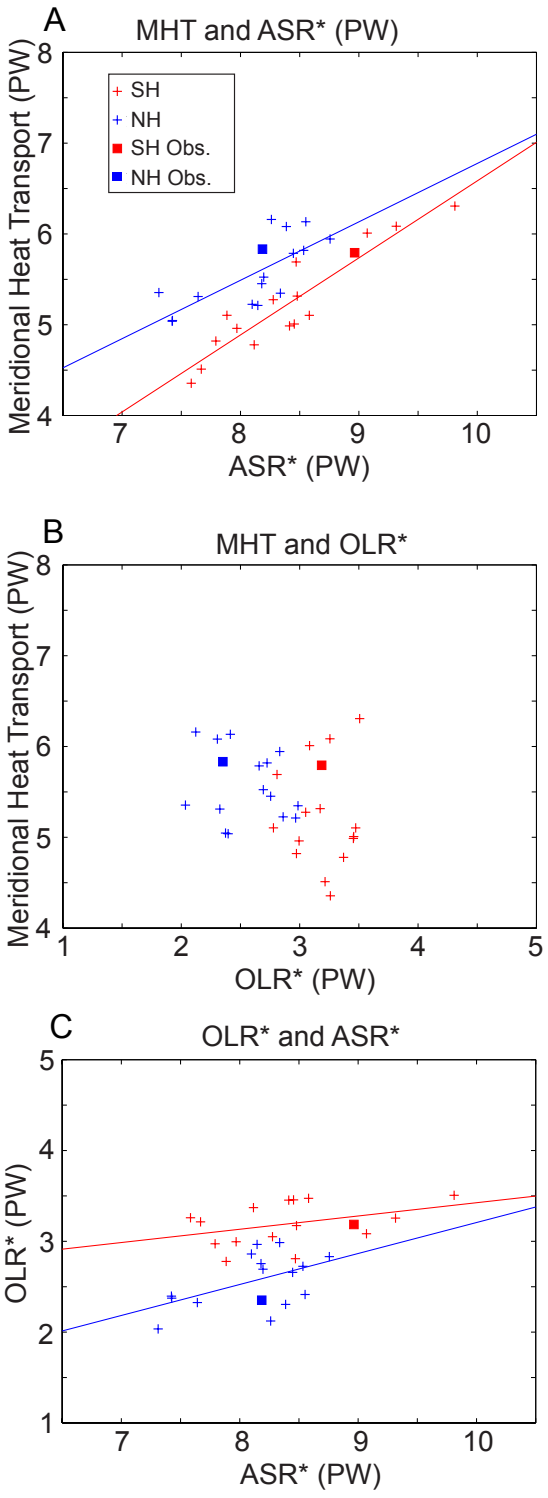

Figure 3.3: (a) Maximum heat transport (MHT_{MAX}) versus $ASR*$ in each the NH and SH (blue and red plus signs, respectively) of the CMIP3 PI model ensemble and observations (filled squares). (b) As in (a) except for MHT_{MAX} versus OLR^*. (c) As in (a) except for OLR^* versus $ASR*$. The blue and red lines are the linear best fits in the SH and NH and are only shown where significant.

Inter-model Spread, 2σ (PW)		
Field	NH	SH
$2\sqrt{\left[\langle ASR* \rangle^2\right]}$	0.90	1.20
$2\sqrt{\left[\langle OLR* \rangle^2\right]}$	0.58	0.46
$2\sqrt{[\langle ASR* \rangle \bullet \langle OLR* \rangle]}$	0.50	0.44
$2\sqrt{\left[\langle MHT_{MAX} \rangle^2\right]}$	0.78	1.12

R^2 (and regression coefficients when significant) between variables		
Fields	NH	SH
MHT_{MAX} vs. ASR*	0.57 (0.64)	0.85 (0.85)
MHT_{MAX} vs. OLR*	0.02	0.00
OLR* vs. ASR*	0.28 (0.36)	0.15 (0.15)
MHT_{MAX} vs. $ASR*_{ATMOS}$	0.63	0.84
ASR* vs. $ASR*_{ATMOS}$	0.80 (0.88)	0.93 (0.82)
ASR* vs. $ASR*_{SURF}$	0.09	0.21(-1.32)

Table 3.3: (Top rows) The spread (2σ) in the extratropical energy budget (Eq. 3.4b) in the PI simulations by the CMIP3 models. All terms are in units of PW. (Bottom rows) Statistical relationships between the inter-model spread of the variables considered in this study. The squared correlation coefficients (R^2) and regression coefficients (listed in parenthesis when significant) are calculated separately in each hemisphere for the ensemble of 15 models listed in Table 2.3.

between OLR^* and MHT_{MAX} from the statistics of $ASR*$ and $OLR*$. Multiplying Eq. 3.4 by $ASR*$, averaging over all models, and dividing by the standard deviation of $ASR*$ and MHT_{MAX} (from Eq. 3.7) gives

$$R_{MHT,ASR^*} \equiv \frac{[\langle ASR^* \rangle \bullet \langle MHT_{MAX} \rangle]}{\sqrt{\left[\langle ASR^* \rangle^2\right]}\sqrt{\left[\langle MHT_{MAX} \rangle^2\right]}} \tag{3.8a}$$

$$= \frac{\left[\langle ASR^* \rangle^2\right] - [\langle ASR^* \rangle \bullet \langle OLR^* \rangle]}{\sqrt{\left[\langle ASR^* \rangle^2\right]}\sqrt{\left[\langle ASR^* \rangle^2\right] + \left[\langle OLR^* \rangle^2\right] - 2\,[\langle ASR^* \rangle \bullet \langle OLR^* \rangle]}} \tag{3.8b}$$

where R_{MHT,ASR^*} is the correlation coefficient between MHT_{MAX} and $ASR*$ across the models. A similar expression holds for R_{MHT,OLR^*}. In the dynamic limit where OLR* and ASR* are uncorrelated, the fraction of the MHT_{MAX} variance explained by OLR^* and $ASR*$ is proportional to the variance of each variable and the fractional variance explained by each variable would sum to unity. In this limit 70% of the inter-model variance of MHT_{MAX} in the NH would be explained by inter-model differences in $ASR*$ and the remaining 30% would be explained by inter-model differences in OLR^*. (In the SH, 87% of the MHT_{MAX} variance would be explained by ASR* and 13% by OLR*). In our specific case, however, the covariance between $ASR*$ and OLR^* reduces the variance in MHT_{MAX} explained by ASR* from 70% to 57% in the NH and from 87% to 85% in the SH. Similarly the variance in MHT_{MAX} that is explained by OLR* is reduced from 30% in the dynamic limit to 0% in the NH and from 13% to 02% in the SH. The near zero correlation between MHT_{MAX} and OLR^* can be understood from the competing effects of the two terms in the numerator of Eq. 3.8b. Averaged over the ensemble members, a one unit anomaly in OLR^* is accompanied by an approximately one unit anomaly in $ASR*$, because the OLR^* variance and covariance between $ASR*$ and OLR^* are approximately equal (Table 3.3). Thus, the typical magnitude of an $ASR*$ anomaly associated with a given OLR^* anomaly nearly balances the OLR^* anomaly's impact on the extratropical energy budget leading to

no correlation between OLR^* and MHT_{MAX}.

In summary, the MHT_{MAX} spread in climate models is due to $ASR*$ differences between the models because the inter-model spread in $ASR*$ exceeds that in OLR^* and $ASR*$ and OLR^* are only weakly correlated; the models are closer to the dynamic limit than the radiative limit, especially in the SH. In the remainder of this chapter, we will analyze the physical processes that determine $ASR*$, OLR^*, their inter-model spread, and covariance.

3.3 The cause of inter-model spread in $ASR*$

We now describe a method for partitioning $ASR*$ into components due to incident radiation at the TOA (the Earth-Sun geometry) and the meridional gradient of planetary albedo. We then further partition the planetary albedo contribution to $ASR*$ into components due to atmospheric and surface reflection and apply this methodology to the CMIP3 simulations.

3.3.1 $ASR*$ partitioning into incident and planetary albedo contribution

3.3.1.1 Methods

$ASR*$ is non-zero due to both the meridional gradient in incident solar radiation and to the meridional gradient in the planetary albedo. We can partition $ASR*$ into these two component contributions by writing the zonal average ASR as the product of the planetary albedo and incident solar radiation and then breaking each term into a global average and a spatial anomaly:

$$ASR(x) = a(x)S(x) = (\bar{a} + a'(x))(\bar{S} + S'(x)) = \bar{a}\bar{S} + \bar{a}S'(x) + a'(x)\bar{S} + a'(x)S'(x) \quad (3.9)$$

where *a(x)* is the co-albedo (one minus albedo), overbars denote a spatial average, and primes indicate spatial anomalies[4]. $ASR*$ can be calculated from Eq. 3.9 by subtracting

[4]An alternative approach to dividing the fields into a global mean and spatial anomaly is to expand the variables in terms of even Legendre polynomials in each hemisphere, as was done in Stone (1978), North (1975), and Enderton and Marshall (2009). Our $ASR*$ and component contributions to ASR*

the global average of each term and integrating over the extratropics:

$$ASR^* = -2\pi R^2 \left[\bar{a} \int_{x(ASR'=0)}^{1} S'(x)dx + \bar{S} \int_{x(ASR'=0)}^{1} a'(x)dx \right.$$

$$\left. + \int_{x(ASR'=0)}^{1} \left[S'(x)a'(x) - \frac{1}{2} \int_{-1}^{1} S'(x)a'(x)dx \right] dx. \right. \quad (3.10)$$

The first term on the right hand side of Eq. 3.10 represents the equator-to-pole contrast in incident solar radiation multiplied by the global average co-albedo and is primarily a function of the Earth-Sun geometry; it is the equator-to-pole contrast of ASR that would exist if there were no meridional variations in planetary albedo. The second term is the contribution of inhomogeneities in planetary albedo to ASR* in the absence of spatial variations of incident solar radiation (Fig. 3.4a). The last term is the covariance of the spatial anomalies in planetary albedo and incident radiation. The covariance contributes to a positive global average ASR because the high latitude regions have high albedos but receive a deficit of solar radiation such that the global average planetary co-albedo ($\bar{a}$) is smaller than the global average solar weighted planetary coalbedo. Similarly, the last term in Eq. 3.10 makes a negative contribution to $ASR*$ because the high planetary albedo regions receive less incident radiation than the global average value that appears in the second term of Eq. 3.10 such that the contribution to $ASR*$ due to the meridional gradient in planetary albedo is overestimated by the second term alone. Therefore, we can interpret the covariance term

---

are proportional to the second Legendre coefficients provided that the spatial structure of ASR projects entirely onto the zeroth and second Legendre polynomials. The total ASR contrast calculated by these two methods agree to within 2%; the first order terms agree to within 5% of each other, and the second order term (the covariance) agrees to within 30%. The discrepancy is larger for the second order term because, even if the planetary albedo and incident solar radiation were fully captured by the first two Legendre polynomials, the covariance projects primarily on the 4^{th} Legendre polynomial and only secondarily onto the 2^{nd} polynomial (i.e. note the spatial structure of the covariance term in Fig. 3.4b). In this regard, our index of the meridional difference is more accurate than that obtained by expansion in terms of Legendre polynomials truncated at the 2^{nd} order term , although the primary conclusions reached here are independent of the methodology employed.

as a correction to the planetary albedo's contribution to *ASR**.

Eq. 3.10 divides $ASR*$ into an incident component due to the Earth-Sun geometry that exists in the absence of any meridional gradient in planetary albedo (the first term, red line in Fig. 3.4a,b) and a component that owes its existence to the meridional gradient in albedo (the sum of the second and third terms, Fig. 3.4b). Hence, in the remainder of this study, we will define *the net planetary albedo contribution to ASR** to be the sum of the second and third terms[5].

3.3.1.2 Results

In the observations, spatial variations in planetary albedo contribute 2.9 PW to $ASR*$ in the NH via Eq. 3.10, representing 35% of the total $ASR*$ (8.2 PW – Table 3.2 and Fig. 3.4d). In the SH, spatial variations in planetary albedo contribute 3.7 PW to $ASR*$ (41% of the total $ASR*$ of 9.0 PW). The inter-model average planetary albedo contribution to $ASR*$ in the NH is nearly identical to the observations (Table 3.2) whereas the models have a smaller equator-to-pole-contrast in planetary albedo in the SH than is observed resulting in smaller $ASR*$ values (by 0.5 PW on average) relative to Nature.

The planetary albedo contribution to $ASR*$ varies widely between models ($2\sigma = 0.9$ PW in the NH and 1.2 PW in the SH). In contrast, the incident contribution to $ASR*$ varies by less than 1% among the different CMIP3 models. The small inter-model spread in the incident contribution to ASR* is due to primarily to inter-model differences in global average planetary albedo and secondarily to small inter-model differences in the solar constant. The inter-model spread in the planetary albedo contribution to $ASR*$ explains 99% of the spread in ASR* in both hemispheres. Thus, the inter-model differences in $ASR*$ are a consequence of the inter-model differences in the meridional profile of planetary albedo.

---

[5]It is equally valid to interpret Eq. 3.10 as consisting of a component that exists in the absence of a meridional gradient in solar insolation (the second term) and a component owing its existence to the meridional gradient of solar insolation (the sum of the first and third terms). The interpretation is contingent on the phrasing of the question. In this regard, the grouping of the terms we adopt in this paper is a lower limit assessment of the planetary albedo gradient's contribution to ASR*.

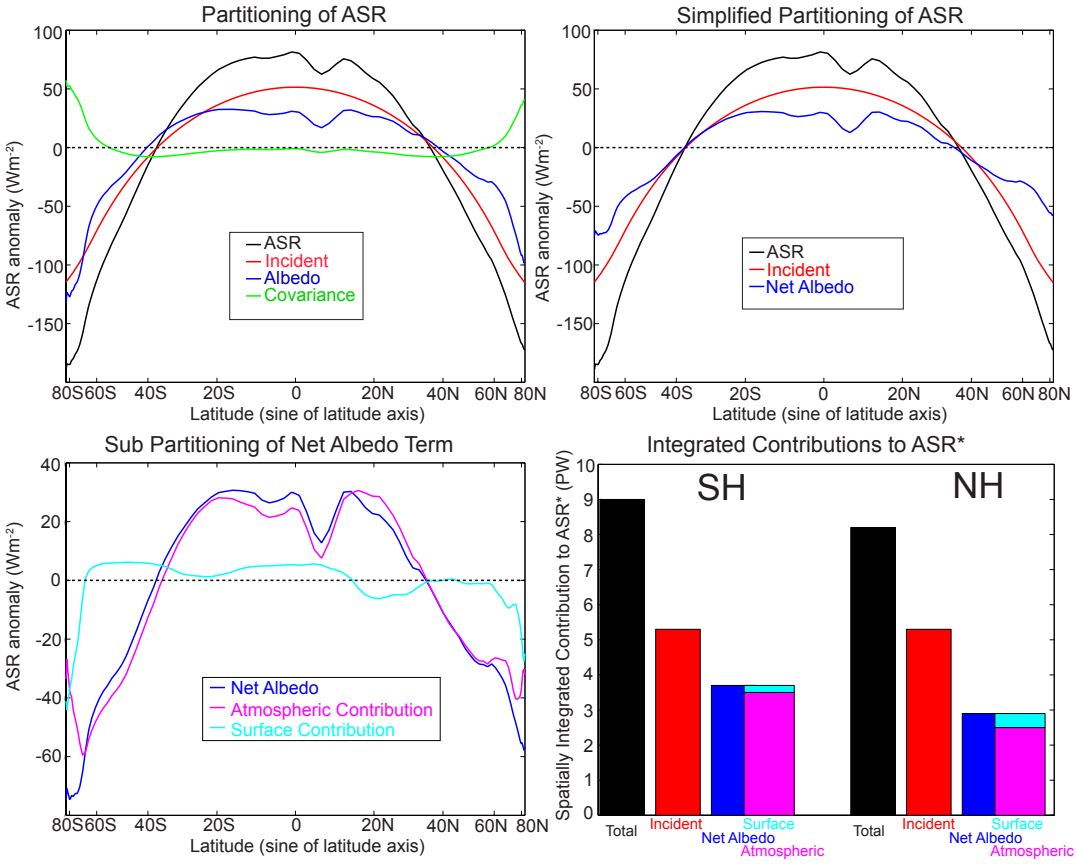

Figure 3.4: (a) CERES Zonal average ASR anomalies from the global average (black) partitioned into incident (red), albedo (blue), and covariance (green) terms via Eq. 3.10. (b) As in (a), except combining the albedo and covariance terms into a net albedo term (blue) as discussed in the text. (c) The subdivision of the net albedo term into atmospheric (magenta line) and surface reflection (cyan line) terms as discussed in Subsection 3.3.2. (d) The contribution of each of the terms to $ASR*$ in each hemisphere, calculated from the spatial integral of the curves over the extra-tropics (colors are the same as the curves in the previous panels).

3.3.2 Partitioning of planetary albedo into atmospheric and surface components

3.3.3 Methodology

We use the method of Donohoe and Battisti (2011a) to partition the planetary albedo into a component due to reflection off of objects in the atmosphere and a component due to surface reflection. In short, their method builds a simplified radiative transfer model at each gridpoint that accounts for atmospheric absorption, atmospheric reflection, and surface reflection for an infinite number of passes through the atmosphere. By assuming that the atmosphere is isotropic to shortwave radiation, the simplified model provides analytical expressions for the upwelling and downwelling shortwave fluxes at both the surface and top of the atmosphere in terms of the incident radiation, the fractions of atmospheric reflection and absorption during each pass through the atmosphere, and the surface albedo. The equations can be solved for given the radiative fluxes at the TOA and the surface. The atmospheric contribution to the planetary albedo is equal to the fraction of radiation reflected during the first downaward pass through the atmosphere and will be denoted as $\alpha_{P,ATMOS}$. The surface contribution to planetary albedo is equal to the fraction of incident radiation that is reflected at the surface and eventually escapes to space and will be denoted as $\alpha_{P,SURF}$.

We calculate $\alpha_{P,ATMOS}$ and $\alpha_{P,SURF}$ for both the models and observations using annual average radiative fields. We have also performed the calculations on the climatological monthly mean data from the observations and then averaged the monthly values of $\alpha_{P,ATMOS}$ and $\alpha_{P,SURF}$ to obtain the annual average climatology. The zonal average $\alpha_{P,ATMOS}$ calculated from monthly data agree with those calculated directly from the annual average data to within 1% of $\alpha_{P,ATMOS}$ at each latitude.

3.3.3.1 Results

In both the models and observations, the vast majority (over 85%) of the global average planetary albedo is due to $\alpha_{P,ATMOS}$. *The surface contribution to planetary albedo,* $\alpha_{P,SURF}$, is approximately one third of the surface albedo because the atmosphere opacity

attenuates the amount of incident solar radiation that reaches the surface and the amount of radiation that is reflected at the surface that escapes to space. These results are discussed at length in Donohoe and Battisti (2011a). Here, we focus on the implications of these results on the inter-model spread in $ASR*$ and MHT_{MAX}.

The contribution of $\alpha_{P,ATMOS}$ and $\alpha_{P,SURF}$ to spatial anomalies in ASR and $ASR*$ can be assessed by first dividing the planetary coalbedo (a) into separate atmospheric and surface components and then writing each component in terms of a global average quantity ($^-$) and the spatial departure from the global average ($'$):

$$a(x) = 1 - \alpha_{P,ATMS}(x) - \alpha_{P,SURF}(x)$$

$$= 1 - \bar{\alpha}_{P,ATMOS} - \bar{\alpha}_{P,SURF} - \alpha^{'}_{P,ATMOS}(x) - \alpha^{'}_{P,SURF}(x) \quad (3.11)$$

We then substitute the expression for *a(x)* in Eq. 3.11 into 3.9 to define the atmospheric and surface reflection contributions to spatial anomalies in ASR (Fig. 3.4c). The vast majority of the meridional gradient in ASR associated with planetray albedo inhomogeneities is due to $\alpha_{P,ATMOS}$ (Fig. 3.4c); $\alpha_{P,SURF}$ only contributes substantailly to spatial anomalies in ASR in the region poleward of 70° which composes a small fractional area of the extratropical domain. Substituting Eq. 3.11 into Eq. 3.10 yields the contribution of $\alpha_{P,ATMOS}$ to ASR^*, ASR^*_{ATMOS} :

$$ASR^*_{ATMOS} = 2\pi R^2 \bar{S} \int_{x(ASR'=0)}^{1} \alpha^{'}_{P,ATMOS}\, dx$$
$$+ 2\pi R^2 \int_{x(ASR'=0)}^{1} \left[\alpha^{'}_{P,ATMOS}\, S^{'} - \frac{1}{2} \int_{-1}^{1} \alpha^{'}_{P,ATMOS} S^{'}\, dx \right] dx, \quad (3.12)$$

where we have again grouped the linear and covariance terms together to calculate the total contribution of the spatial structure in $\alpha_{P,ATMOS}$ to $ASR*$ ($ASR*_{ATMOS}$). A similar

expression is used to calculate the contribution of $\alpha_{P,SURF}$ to ASR^* which we define as ASR^*_{SURF}. In the observations ASR^*_{ATMOS} is found to contribute 2.5 PW to ASR^* while ASR^*_{SURF} is found to contribute 0.4 PW to ASR^* in the NH (Table 3.2). In the SH, ASR^*_{ATMOS} contributes 3.5 PW to ASR^* while ASR^*_{SURF} contributes 0.2 PW to ASR^*. These results suggest that, even if the equator-to-pole gradient in surface albedo were to greatly diminish (e.g., in an ice-free world) the equator-to-pole scale gradient in ASR would decrease by less than 5% in each hemisphere, neglecting any major changes in the atmospheric reflection or absorption.

In the inter-model average, the breakdown of ASR^* in the NH into components associated with ASR^*_{ATMOS} and ASR^*_{SURF} is similar to that in Nature; the CMIP3 average ASR^*_{ATMOS} (ASR^*_{SURF}) is 2.4 PW (0.5 PW) while that observed is 2.5 PW (0.4 PW). In the SH, the CMIP3 ensemble average ASR^*_{ATMOS} is 2.9 PW which is one standard deviation smaller than the observed value of 3.5 PW and the ensemble average ASR^*_{SURF} is 0.3 PW, which is in close agreement with the observations (0.2 PW). These results suggest that the model bias towards smaller than observed MHT_{MAX} in the SH (Fig. 3.2) is a consequence of smaller than observed equator-to-pole gradient in shortwave cloud reflection (ASR^*_{ATMOS}).

Fig. 3.5 shows a scatter plot of the total ASR^* against (a) ASR^*_{ATMOS} (b) ASR^*_{SURF} from the CMIP3 models (plus signs) in the northern (blue) and southern (red) hemispheres. There is a remarkably large range in the simulated ASR^* ($2\sigma = 0.9$ PW and 1.2 PW in NH and SH respectively, see Table 3.2). Almost all of the inter-model spread in ASR^* is due to ASR^*_{ATMOS}; ASR^*_{ATMOS} (2 sigma = 1.2 PW and 1.4 PW in the NH and SH) is highly correlated with the total ASR^* ($R^2 = 0.94$), and the best-fit slope in each hemisphere is nearly unity. In comparison, the inter-model spread in ASR^*_{SURF} is small ($2\sigma = 0.5$ PW and 0.4 PW in the NH and SH, respectively) and not correlated with total ASR^*.

We take two limiting models for how the meridional structure of atmospheric and surface reflection contribute to ASR^*: "Model A" in which the surface albedo is spatially invariant so that ASR^* is determined entirely by the spatial structure of atmospheric reflection and

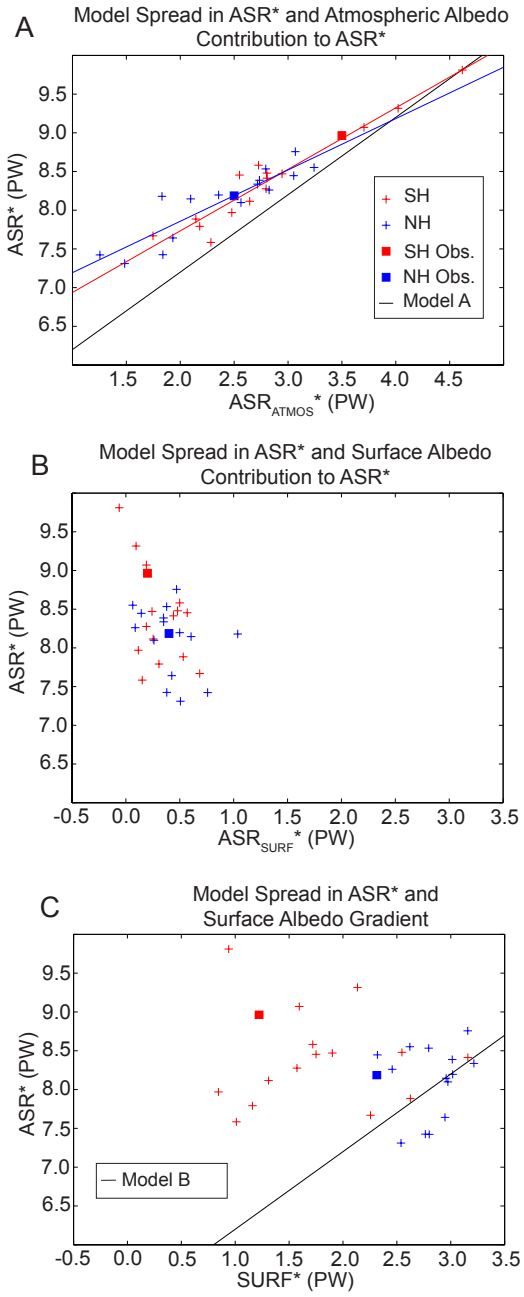

Figure 3.5: (a) ASR^* versus atmospheric reflection contribution to ASR^*(ASR^*_{ATMOS}) in each the NH and SH (blue and red plus signs) of the CMIP3 PI model ensemble and observations (filled squares). The theoretical prediction of "Model A", as discussed in the text, is given by the black line. (b) As in (a) except plotted against surface albedo contribution to ASR^* (ASR^*_{SURF}). (c) As in (b) except for the surface albedo gradient ($SURF^*$). The theoretical prediction of "Model B", as discussed in the text, is given by the black line. The blue and red lines are the linear best fits in the SH and NH and are only shown where significant.

"Model B" in which the atmosphere is transparent to shortwave radiation so that ASR^* is determined entirely by the surface albedo gradient. In the case of "Model A", ASR^* would equal the sum of the ASR^*_{ATMOS} and the incident (geometric) component of 5.2 PW (black line, Fig. 3.5a). "Model A" is an excellent fit to the inter-model spread in ASR^*. "Model A" slightly under predicts ASR^* in all cases because ASR^*_{SURF} is positive in all models (the vertical offset between the black line and the individual model results in Fig. 3.5a). This suggests that, while surface processes do play a role in determining ASR^*, the majority of the inter-model spread in ASR^* (94%) is explained by differences in atmospheric reflection.

At the other end of the spectrum, if the atmosphere were indeed transparent to shortwave radiation ("Model B"), ASR^* would be equal to the incident (geometric) contribution plus the surface reflection contribution given by the global average solar insolation times the surface albedo anomaly integrated over the extratropics (plus a second order term):

$$SURF^* = \bar{S} \int_{x(ASR'=0)}^{1} \alpha' dx + \int_{x(ASR'=0)}^{1} \left[\alpha' S' - \frac{1}{2} \int_{-1}^{1} \alpha' S' dx \right] dx, \tag{3.13}$$

where α' is the spatial departure of surface albedo from the global average surface albedo. $SURF^*$ is the contribution of the surface albedo to ASR^* if the atmosphere were transparent to shortwave radiation ("Model B"). The theoretical prediction of "Model B" is co-plotted with results from the CMIP3 PI simulations in Fig. 3.5c. "Model B" is clearly a poor description of the CMIP3 ensemble. Surface albedo plays a negligible role in determining the inter-model differences in ASR^* because the surface albedo is strongly attenuated by the atmosphere (reflection and absorption) and the inter-model spread in atmospheric reflection overwhelms the surface albedo contribution to planetary albedo spread.

These results demonstrate that differences in atmospheric reflection are, by far, the primary reason for the remarkable spread in ASR^* in the CMIP3 ensemble of PI simulations. We previously demonstrated that the vast majority of the inter-model differences in MHT_{MAX} are due to inter-model differences in ASR* (Section 3.2). As a consequence, inter-

model differences in ASR^*_{ATMOS} explain 63% of the inter-model variance of MHT_{MAX} in the NH and 84% of the inter-model variance of MHT_{MAX} in the SH (Fig. 3.6).

3.4 Processes controlling the inter-model spread of OLR^*

In the previous sections we concluded that the CMIP3 ensemble features large differences in ASR^* (due to cloud reflection differences) that are only weakly compensated by differences in OLR^* leading to large inter-model spread in MHT_{MAX}. This result is surprising because cloud longwave and shortwave radiative forcing are known to compensate for each other in the tropics (Kiehl, 1994; Hartmann et al., 1979). In this section, we ask why the inter-model spread in ASR^* and OLR^* do *not* compensate for each other. We first analyze the processes that cause the inter-model spread in OLR (Subsection 3.4.1). We then diagnose the processes that cause the inter-model spread in OLR^* (Subsection 3.4.2) and relate the results to the inter-model spread of ASR^* (Subsection 3.4.3).

3.4.1 Inter-model spread in OLR

OLR is a consequence of both clear sky processes (i.e. temperature and specific humidity) and cloud properties (i.e. cloud optical thickness and height). We partition the inter-model spread in OLR into cloud and clear sky contributions. We then further sub-partition the cloud contribution into cloud fraction and cloud structure components and the clear-sky contribution into surface temperature and specific humidity components.

We diagnose the cloud contribution to OLR as the longwave cloud forcing (LWCF, Kiehl, 1994):

$$LWCF = OLR_{CLEAR} - OLR, \tag{3.14}$$

where OLR is the total-sky OLR and OLR_{CLEAR} is the clear-sky OLR. We decompose the inter-model spread in OLR into clear sky and cloud components as follows: at each latitude, the inter-model differences in the zonal average OLR_{CLEAR} and -LWCF are regressed against the inter-model differences in total OLR. The regression coefficients are then rescaled by the spread (2σ) of total OLR at each latitude to give the clear sky and cloud

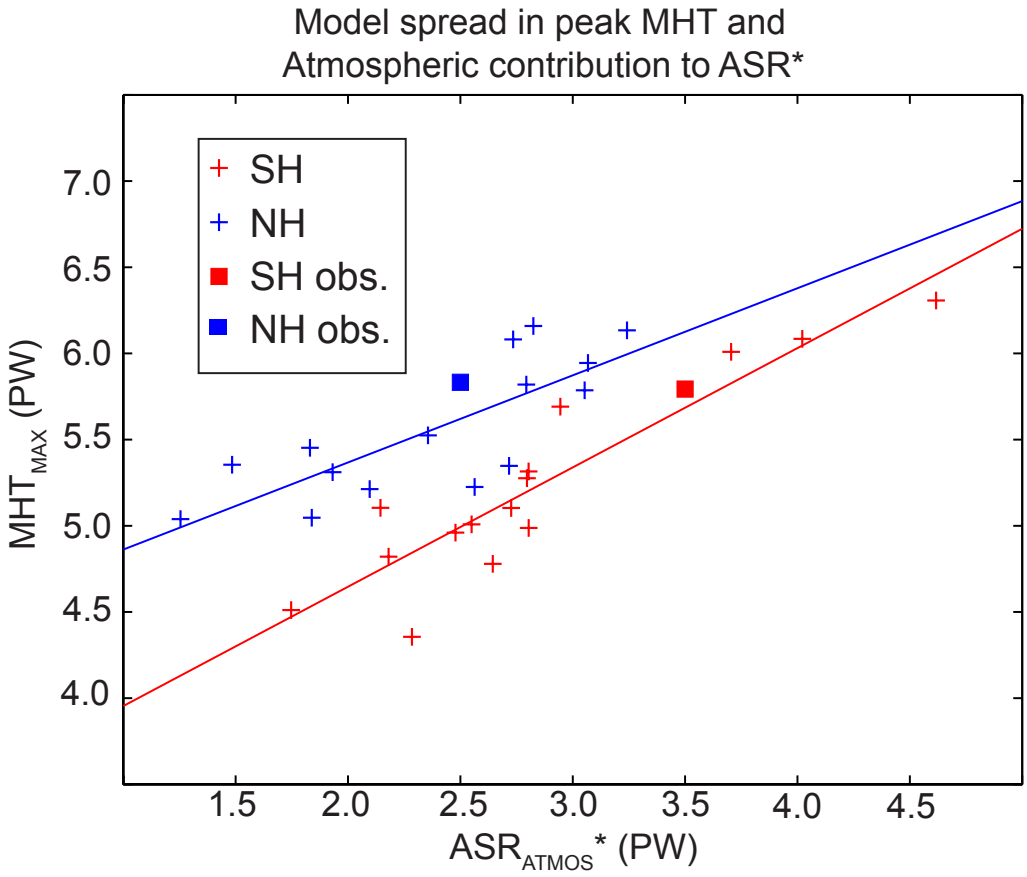

Figure 3.6: MHT_{MAX} versus atmospheric reflection contribution to ASR^* (ASR^*_{ATMOS}) in each the NH and SH (blue and red plus signs) of the CMIP3 PI model ensemble and observations (filled squares). The blue and red lines are the linear best fits in the SH and NH and are only shown where significant.

contribtions to the OLR spread. By construction, the clear-sky and cloud contributions to the OLR spread add to the total-sky OLR spread (Fig. 3.7).

In the tropics, the inter-model spread in OLR is almost entirely due to differences in *LWCF* (Fig. 3.7a). In contrast, the inter-model spread in OLR in the polar regions is almost entirely due to differences in OLR_{CLEAR}. In the subtropics, *LWCF* and OLR_{CLEAR} contribute nearly equally to the *OLR* spread. In the SH storm track region, *LWCF* contributes more the *OLR* spread than OLR_{CLEAR} while the opposite is true in the NH storm track region.

We further divide the inter-model spread in *LWCF* into components due inter-model differences in cloud fraction and cloud structure. The total-sky *OLR* can be written as the cloud fraction (f) weighted sum of the *OLR* when the scene is clear (OLR_{CLEAR}) and the *OLR* when the scene is cloudy (OLR_{CLOUD}):

$$\begin{aligned} OLR &= (1-f)OLR_{CLEAR} + f(OLR_{CLOUD}) \\ &= OLR_{CLEAR} + f(OLR_{CLOUD} - OLR_{CLEAR}). \end{aligned} \quad (3.15)$$

Plugging Eq. 3.14 into Eq. 3.15 and rearranging, we find an expression for *LWCF* in terms of the cloud fraction (f) and cloud OLR properties:

$$LWCF = f(OLR_{CLEAR} - OLR_{CLOUD}) \equiv f(C_{STRUC}). \quad (3.16)$$

Eq. 3.16 states that *LWCF* is a consequence of how often the scene is cloudy and the optical properties of the cloud (C_{STRUC}). For example, two models with the same f could have very different *LWCF* due to different cloud top heights (Hartmann et al., 1992). The inter-model spread in *LWCF* is divided into components due to inter-model differences in f and C_{STRUC} by decomposing f and C_{STRUC} into the ensemble average ($\tilde{}$) and model departures from the ensemble average($\langle\ \rangle$) at each latitude:

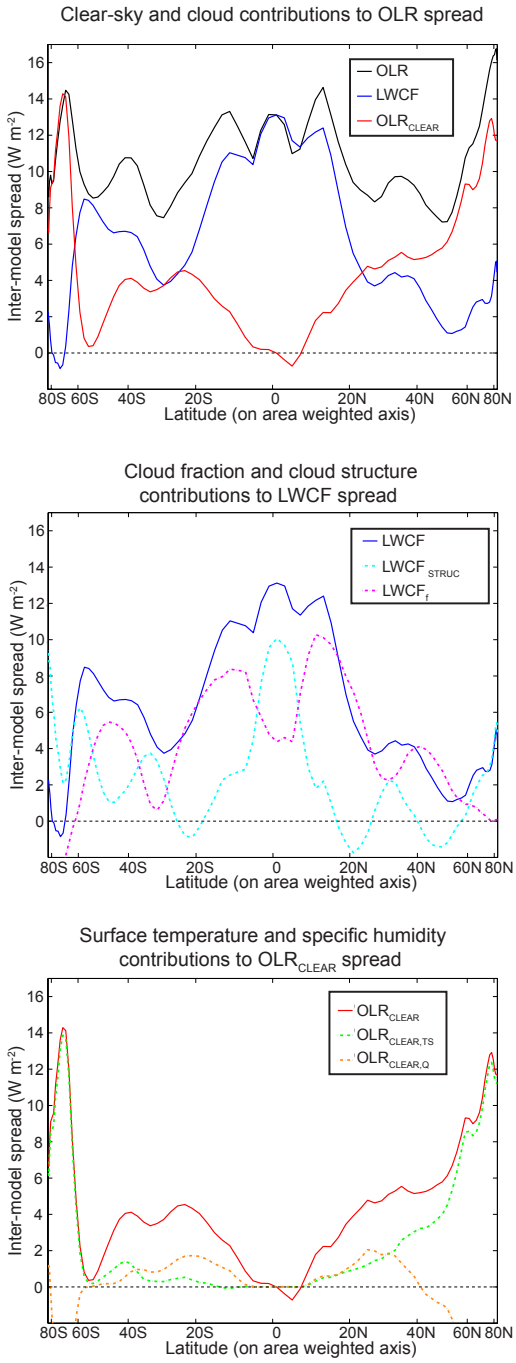

Figure 3.7: (a) CMIP3 inter-model spread in OLR decomposed in cloud ($LWCF$) and clear sky (OLR_{CLEAR}) components as described in the text. (b) The LWCF contribution to the inter-model spread in OLR decomposed into cloud fraction ($LWCF_f$) and cloud structure ($LWCF_{STRUC}$) components. (c) The OLR_{CLEAR} contribution to the inter-model spread in OLR decomposed into components that are linearly congruent with the surface temperature spread ($OLR_{CLEAR,TS}$) and the vertically integrated specific humidity spread ($OLR_{CLEAR,Q}$).

$$LWCF = (\tilde{f} + \langle f \rangle)(\tilde{C}_{STRUC} + \langle C_{STRUC} \rangle)$$
$$= \tilde{f}\tilde{C}_{STRUC} + \tilde{f}\,\langle C_{STRUC} \rangle + \langle f \rangle\,\tilde{C}_{STRUC} + \langle f \rangle\,\langle C_{STRUC} \rangle\,. \quad (3.17)$$

The first term on the right hand side does not contribute to the inter-model spread in *LWCF*. The second and third terms correspond to the contribution of cloud structure differences and cloud fraction differences to the inter-model spread in *LWCF*. The last term is substantially smaller than the other terms at all latitudes (not shown).

Inter-model differences in f are responsible for the majority of the inter-model *OLR* spread in the subtropics and SH storm track region and approximately 50% of the inter-model *OLR* spread in the NH storm track region (Fig. 3.7b). Differences in C_{STRUC} are responsible for the vast majority of the inter-model spread of *LWCF* in the deep tropics. In the polar regions (poleward of 60°), inter-model differences in *LWCF* are uncorrelated with the cloud fraction spread suggesting that cloud optical properties (as opposed to cloud amount) determines *LWCF* in this region (Curry and Ebert, 1992).

The contribution of OLR_{CLEAR} to the *OLR* spread is subdivided into components that are linearly congruent (Thompson and Solomon, 2002) with the inter-model spread in surface temperature and vertically integrated specific humidity as follows. The correlation coefficient between inter-model differences in OLR_{CLEAR} and surface temperature (or the negated specific humidity) is multiplied by the OLR_{CLEAR} spread at each latitude. The inter-model differences in surface temperature explain the vast majority of the inter-model spread in OLR_{CLEAR} in the NH extratropics and make the largest contribution to the *OLR* spread in the polar regions of both hemispheres (Fig. 3.7c). This spatial structure mimics the inter-model spread in surface temperature spread ($R^2 = 0.95$) which features values of approximately 7 K in the polar regions (2σ) and less than 2 K equatorward of 40° (not shown). The regression coefficient between surface temperature and OLR_{CLEAR} for all gridpoints and models considered together is 2.1 W m^{-2} K^{-1} which is consistent with other

estimates of the linear parameterization of OLR with surface temperature (Warren and Schneider, 1979). We understand these results as follows. Per unit perturbation of surface temperature, the OLR changes by approximately 2 W m^{-2} with some regional dependence[6]. Thus, the OLR_{CLEAR} spread scales as the surface temperature spread times approximately 2 W m^{-2} K^{-1} with higher temperatures corresponding to larger OLR values.

We also expect OLR_{CLEAR} to be negatively correlated with the water vapor content of the upper atmosphere due to the greenhouse effect. Indeed, inter-model differences in vertically integrated water vapor explain a portion of the OLR_{CLEAR} spread in the sub-tropics that was not previously explained by inter-model differences in surface temperature(Fig. 3.7c) with higher vapor content corresponding to lower OLR values due to the raising of the effective emission level. In the high latitudes the opposite is true; high vapor content corresponds to more OLR due to the positive correlation between upper tropospheric water vapor and surface temperature (not shown) that is absent in the subtropics. The inter-model differences in high latitude water vapor content are highly correlated with surface temperature differences and the inter-model differences in water vapor explain a negligible amount of the inter-model spread in OLR$_{CLEAR}$ beyond the spread expected from the water vapor and surface temperature covarince and the relationships between surface temperature and OLR$_{CLEAR}$; removing the inter-model differences in water vapor that are linearly congruent with the inter-model differences in surface temperature to define the "residual water vapor" content results in s near zero correlation between inter-model differences in OLR$_{CLEAR}$ and the "residual water vapor" in the high latitudes (not shown).

In summary, the inter-model spread in OLR is a consequence of nearly equal contributions from clear-sky and cloud processes with the cloud processes playing a dominant role in the lower latitudes and clear-sky processes dominating the extratropics. The cloud contribution is due to differences in both cloud fraction and cloud structure while the clear-sky contribution is primarily due to surface temperature differences with the exception of the

[6]The regression of surface temperature onto OLR$_{CLEAR}$ at each latitude shows larger values in the dry subtropics and lower values in the high latitudes.

subtropics where inter-model differences in water vapor also play a role.

*3.4.2 Inter-model spread in OLR**

The contributions to the *OLR* spread that were discussed in the previous subsection are projected onto the inter-model spread in OLR^* in this subsection. The spread in OLR^* is a consequence of the magnitude of spread in the component contributions to *OLR* (previously discussed) and the spatial decorrelation length scale of those processes. For instance, even though cloud fraction explains a large fraction of the *OLR* spread at each latitude, it would be poorly correlated with the spread in OLR^* if the cloud fraction anomalies were local (poorly correlated with anomalies at adjacent latitudes) as opposed to regional or global. Sliding one point correlation maps of the inter-model differences OLR_{CLEAR} and *LWCF* suggest that inter-model differences in both fields are regional in scale (not shown); individual models tend to have OLR_{CLEAR} and *LWCF* anomalies that extend over the entire tropical region, storm-track region, or polar regions with no significant correlation between anomalies in one region and the other region. The meridional de-correlation length scale (where the spatial auto-correlation is equal to e^{-1}) of the OLR_{CLEAR} anomalies is of order 15° latitude in the extratropics ($\approx 30°$ in the tropics) and is slightly longer than that of *LWCF*.

We define OLR^*_{CLEAR} and OLR^*_{LWCF} for each model by substituting OLR_{CLEAR} and *-LWCF* into the integrand of Eq. 3.6 with the limits of integration defined from the total *OLR* field. The inter-model spread in OLR^*_{CLEAR} is 0.52 PW (0.52 PW) and the inter-model spread in OLR^*_{LWCF} is 0.50 PW (0.48 PW)in the NH (SH – Table 3.4). The near equality of the clear-sky and cloud contribution to OLR^* spread is consistent with the relative contributions of OLR_{CLEAR} and *LWCF* to the *OLR* spread at each latitude (Fig. 3.7) and the fact that both inter-model differences OLR_{CLEAR} and *LWCF* have similar decorrelation length scales. In the NH (SH), 44% (35%) of the inter-model variance in OLR^* is due to differences in OLR^*_{CLEAR} and 40% (23%) is due to differences in OLR^*_{LWCF} (Table 3.4).

	NH		SH	
	Spread – 2σ	R^2	Spread – 2σ	R^2
Division of OLR* into clear and cloud components Correlations with OLR*				
OLR^*_{CLEAR}	0.52 PW	0.44	0.52 PW	0.35
OLR^*_{LWCF}	0.50 PW	0.40	0.48 PW	0.23
Division of OLR^*_{LWCF} into fraction and structure components Correlation with OLR^*_{LWCF}				
$OLR^*_{LWCF,f}$	0.44 PW	0.47	0.50 PW	0.30
$OLR^*_{LWCF,STRUC}$	0.38 PW	0.39	0.52 PW	0.19
OLR^*_{CLEAR} correlation with TS* and Q*				
TS*	3.0 K	0.81	1.8 K	0.85
Q*	2.6 kG m^{-2}	0.12	1.6 kG m^{-2}	0.08

Table 3.4: Division of OLR* spread into clear sky (OLR^*_{CLEAR}) and cloud components (OLR^*_{LWCF} – top rows) and the subsequent division of the cloud contribution into cloud fraction ($OLR^*_{LWCF,f}$)and cloud structure ($OLR^*_{LWCF,STRUC}$) components (middle rows). The bottom rows show the correlation of the OLR^*_{CLEAR} spread with the equator-to-pole contrast of surface temperature (TS*) and specific humidity (Q^*).

We further subdivide OLR^*_{LWCF} into cloud fraction and cloud structure components by use of Eq. 3.17. Inter-model differences in cloud fraction and cloud structure make nearly equal contributions to the inter-model spread in OLR^*_{LWCF} (Table 3.4). This result is consistent with the previous conclusion that cloud structure and cloud fraction make comparable magnitude contributions to the spread in $LWCF$ with some regional dependence (Fig. 3.7) and that inter-model differences in cloud fraction and cloud structure are regional in scale (have similar decorrelation length scales – not shown).

The relationship between the equator-to-pole gradient in surface temperature and OLR^*_{CLEAR} is analyzed by defining TS^*, the surface temperature anomaly (from the global average) averaged over the extratropics:

$$TS^* = \frac{\int_{x(OLR'=0)}^{1} TS'(x)dx}{\int_{x(OLR'=0)}^{1} dx} \tag{3.18}$$

Inter-model differences in TS^* explain 81% (85%) of the inter-model spread in OLR^*_{CLEAR}

(Table 3.4). The regression coefficient between TS^* and OLR^*_{CLEAR} is 0.21 PW K^{-1} which corresponds to 2.0 W m^{-2} OLR_{CLEAR} anomaly per unit temperature anomaly averaged over the polar cap; this number is consistent with linear parameterizations of OLR from surface temperature (Warren and Schneider, 1979). A similar quantity for the equator-to-pole contrast in specific humidity, Q^*, can be defined by substituting the vertically integrated specific humidity into the integrand of Eq. 3.18. Q^* is not significantly correlated with OLR^*_{CLEAR} in either hemisphere (Table 3.4).

In summary the inter-model spread in OLR^* is a consequence of nearly equal magnitude contributions from clear-sky and cloud processes. Inter-model differences in both cloud structure and cloud fraction contribute to the spread in OLR^*_{LWCF} and the vast majority of the OLR^*_{CLEAR} spread is due to inter-model differences in the surface temperature gradient.

3.4.3 Relationship between OLR^* and ASR^*

We gain further insight into why inter-model differences in OLR^* and ASR^* do *not* compensate for each other by analyzing the meridional structure of ASR and OLR anomalies associated with a "typical" ASR^* anomaly from the ensemble average. We regress a normalized index of ASR^* onto the inter-model spread in zonal average ASR, OLR, *-LWCF* and OLR_{CLEAR} (Fig. 3.8). The resulting ASR curve shows the anticipated structure of an ASR^* anomaly with anomalously high values in the tropics and low values in the extratropics; both tropical and extratropical anomalies in $\alpha_{P,ATMOS}$ contribute to a "typical" ASR^* anomaly. In contrast, the OLR anomaly associated with an ASR^* anomaly only has appreciable magnitude in the tropics that is due to *-LWCF* anomalies of the same sign as the ASR anomalies. We interpret this result as the compensation between *-LWCF* and shortwave cloud forcing in the tropics (Kiehl, 1994; Hartmann et al., 1979): the same cloud properties that increase the reflection of shortwave radiation also reduce OLR by raising the effective longwave emission level (more positive LWCF). This compensation is not complete over the tropics for the inter-model spread (c.f. the magnitude of the OLR and ASR curves in the

tropics in Fig. 3.8). Over the extra-tropics, there is little compensation between ASR and OLR anomalies in a "typical" ASR^* anomaly because (i) the OLR spread is a consequence of both clear-sky and cloud properties in this region whereas the ASR spread is primarily due to cloud properties and (ii) the cloud properties that determine the inter-model spread in $\alpha_{P,ATMOS}$ are different from the cloud properties that determine the OLR spread[7]. As a consequence, ASR and OLR anomalies are poorly correlated with eachother over the extratropics leading to ASR^* and OLR^* spread that is only partially compensating.

sectionSimulated change in meridional heat transport due to CO_2 doubling

The diagnostics that were used in the previous sections to analyze the inter-model spread in MHT are applied to the simulated changes in MHT_{MAX} due to CO_2 doubling in this Section.

3.4.4 Model runs used

Here we analyze the output from the "1pctto2x" simulations in the CMIP3 archive (Meehl et al., 2007) that were also analyzed in Subsection 2.4.1. The initial conditions for each model come from the equilibrated pre-industrial (PI) simulations. Atmospheric CO_2 is increased at 1% per year until CO_2 has doubled relative to the PI concentration (70 years). The simulations are then run forward for an additional 150 years with carbon dioxide fixed at twice the PI concentration. We average the model output over the last 20 years of these simulations (years 201-220) and compare the climatological fields to their counterparts in that model's PI simulation. Theses runs will be referred to as the $2XCO_2$ and PI runs respectively.

---

[7]The inter-model spread in $\alpha_{P,ATMOS}$ in the Southern Ocean is poorly correlated with cloud fraction whereas the spatial variations in $\alpha_{P,ATMOS}$ within a given model is well correlated with cloud fraction. This result suggests that inter-model variations in the parameterization of cloud albedo as opposed to cloud fraction differences are responsible for the $\alpha_{P,ATMOS}$ spread.

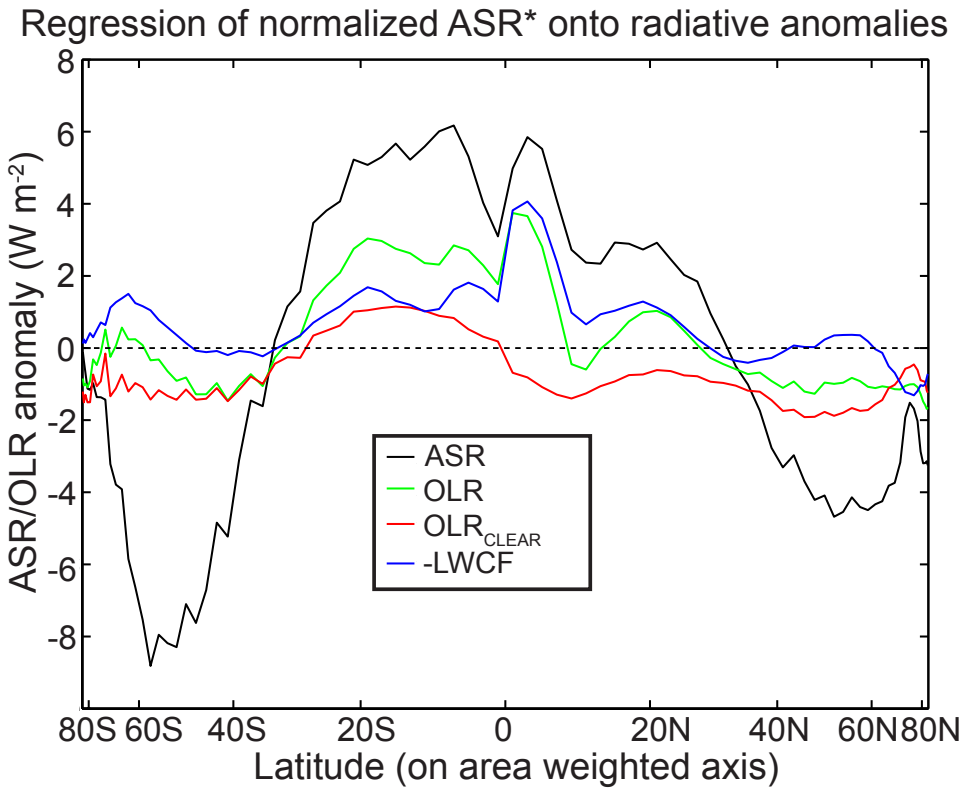

Figure 3.8: .

Regression of the normalized inter-model spread in ASR* on to the inter-model anomalies of ASR (black), OLR (green), OLR_{CLEAR}(red), and -$LWCF$ (blue). The resulting curves are the radiative anomalies associated with a one-standard deviation ASR^* anomaly.

	NH ensemble Average	SH ensemble Average	NH ensemble Spread (2σ)	SH ensemble Spread (2σ)
ΔASR*	-0.08	+0.08	0.33	0.26
ΔASR*$_{ATMOS}$	+0.05	+0.13	0.35	0.28
ΔASR*$_{SURF}$	-0.13	-0.05	0.09	0.07
ΔOLR*	-0.15	+0.06	0.20	0.12
ΔMHT$_{MAX}$	+0.07	+0.02	0.20	0.24
ΔOLR*$_{CLEAR}$	-0.27	+0.04	0.25	0.16
ΔOLR*$_{LWCF}$	+0.12	+0.02	0.14	0.11

Table 3.5: Modeled change in the quantities considered in this study due to CO_2 doubling ($2XCO_2$ – PI). Both the CMIP3 ensemble average change and the inter-model spread in the change are given.

3.4.5 Results

*3.4.5.1 Changes in ASR**

The CMIP3 ensemble average change in ASR^* due to doubling CO_2 (hereafter ΔASR^*) is -0.08 PW in the NH and +0.08 PW in the SH (Table 3.5). The inter-model spread in ΔASR^* (0.33 PW in the NH and 0.26 in the SH) is more than a factor of three larger than the ensemble average ΔASR^*. As a result, the ensemble average change in ASR^* is *not* significantly different from zero in either hemisphere as assessed by a one sample T-test of ΔASR^* (at the 99% confidence interval). We partition these changes in ASR^* between changes in surface and atmospheric reflection below using the methodology outlined in Subsection 3.3.2.

The poleward retreat of the cryosphere in the $2XCO_2$ runs results in a hemispheric average (area weighted) decrease in surface albedo of 0.012 in the NH and 0.006 in the SH in the ensemble average. The hemispheric average surface albedo decreases in all ensemble members (not shown). The surface albedo decreases are primarily in the cryosphere regions and, thus, the meridional structure of the surface albedo change projects negatively onto $SURF^*$; in the ensemble average, $SURF^*$ decreases by 0.7 PW in the NH and 0.4 PW in SH. These changes correspond to 12% and 8% decreases in $SURF^*$ relative to the PI climate.

The corresponding changes in ensemble average ASR^*_{SURF}(hereafter ΔASR^*_{SURF}) are much more modest than the changes in $SURF^*$ (-0.13 PW in NH and -0.05 PW); the atmosphere severely attenuates the effect of the surface albedo changes on the shortwave fluxes at the TOA. Nonetheless, ΔASR^*_{SURF} is negative in all ensemble members (the axis of Fig. 3.9b) and the inter-model spread is small compared to the ensemble average. Thus, the projected retreat of the cryosphere leads to a small reduction in the equator-to-pole gradient in ASR that is robust across the suite of models (significant at the 99% confidence interval).

In contrast, the simulated changes in ASR^*_{ATMOS} due to CO_2 doubling (hereafter ΔASR^*_{ATMOS}) vary widely between models leading to an ensemble average change that is ambiguous in sign (the axis of Fig. 3.9a). The inter-model spread in ΔASR^*_{ATMOS} exceeds that in ΔASR^*_{SURF} by a factor of approximately four in both hemispheres (Table 3.5). As a consequence, the inter-model spread in ΔASR^* is well correlated with ΔASR^*_{ATMOS} ($R^2 = 0.94$ in the NH and 0.91 in SH) and is insignificantly correlated with ΔASR^*_{SURF}. Furthermore, the sign of ΔASR^* is ambiguous in sign despite the decrease in ΔASR^*_{SURF} in all models. The large inter-model spread in ΔASR^*_{ATMOS} overwhelms the small but more predictable change in the equator-to-pole gradient of ASR due to the retreat of the cryosphere (Fig. 3.9c); although all models have negative values on the ASR^*_{SURF} axis, the large spread on the ASR^*_{ATMOS} ordinate lead to inter-model spread across the total ASR^* zero contour.

3.4.5.2 Changes in OLR^*

The ensemble average change in OLR^* due to CO_2 doubling (herafter ΔOLR^*) is -0.15 PW in the NH and +0.06 in the SH and is significant in both hemispheres. We partition the change in OLR into clear-sky (OLR_{CLEAR}) and cloud forcing components ($LWCF$) as was done in Section 3.4 and then project the OLR changes onto the definition of OLR^*; the clear-sky and cloud component contributions to ΔOLR^* will be denoted as ΔOLR^*_{CLEAR} and ΔOLR^*_{LWCF} respectively.

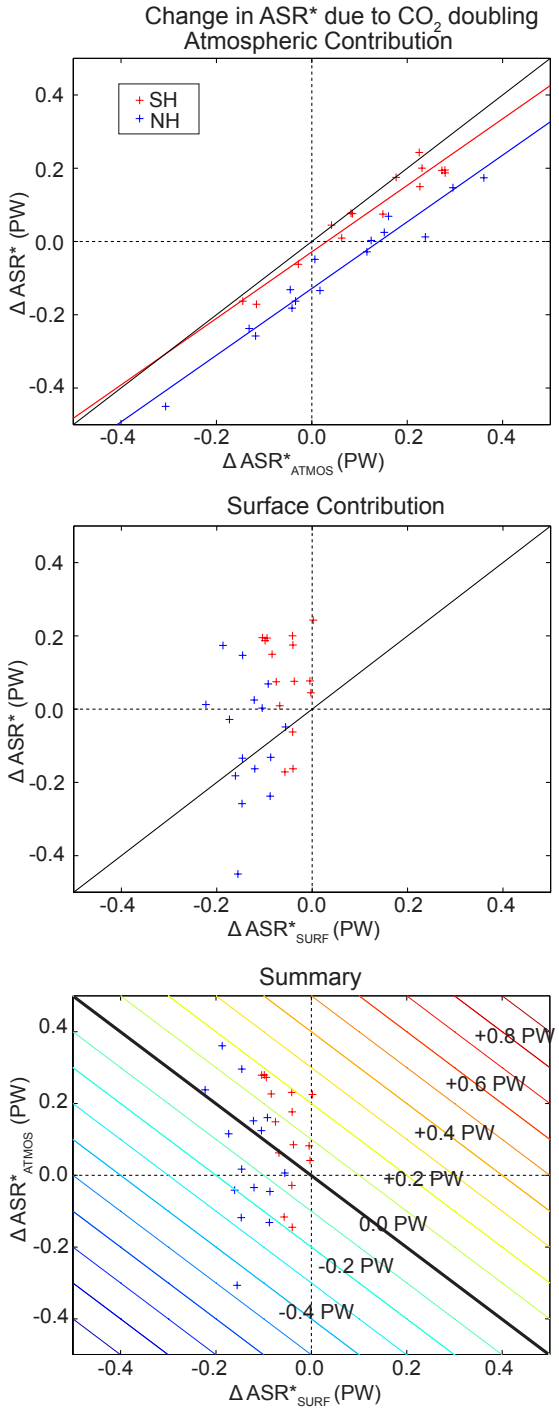

Figure 3.9: Change in ASR^* and atmospheric/surface contributions to ASR* due to CO_2 doubling in the CMIP3 ensemble. (a) ΔASR^* versus ΔASR^*_{ATMOS}. (b) ΔASR^* versus ΔASR^*_{SURF}. (c) ΔASR^*_{ATMOS} versus ΔASR^*_{SURF}. The red (blue) crosses are the simulated changes in the SH (NH). The red and blue lines are the linear best fits and are only shown when significant. The black line is the 1:1 line. The colored contours in (c) are the change in total ASR^*.

In the NH hemisphere, the ensemble average decrease in OLR^* is due a 0.27 PW reduction $\Delta OLR^*{}_{CLEAR}$ that is partially counter-balanced by and increase in $\Delta OLR^*{}_{LWCF}$ (Table 3.5). The largest changes in OLR in the NH are in the Arctic where polar amplification of the surface temperature change leads to large increases in OLR_{CLEAR} and a robust ensemble average increase in summertime cloudiness (Holland and Bitz, 2003) results in a smaller enhancement of $LWCF$ (leading to reduced OLR). As a result, Arctic amplification results in a net reduction of OLR^* in the NH that is robust across the CMIP3 ensemble. The inter-model spread in $\Delta OLR*$ in the NH is also primarily due to inter-model differences in $\Delta OLR^*{}_{CLEAR}$ ($R^2 = 0.68$) and is insignificantly correlated with $\Delta OLR^*{}_{LWCF}$.

In contrast to the NH, the CMIP3 ensemble average $\Delta OLR^*{}_{CLEAR}$ is positive (0.04 PW) in the SH and leads to a net increase in $OLR*$. Changes in $LWCF$ make a smaller contribution to $\Delta OLR*$ in the SH in both the ensemble average and spread (Table 3.5). The enhancement of $OLR*_{CLEAR}$ is associated with a reduction of OLR_{CLEAR} in the extratropical Southern Ocean, between 45°S and 60°S, where the increase in surface temperature due to CO_2 doubling is achieves a global minimum value (Boe et al., 2009) as a consequence of ocean heat storage (International Panel on Climate Change [Griggs and , eds.).

Thus, the hemispheric contrast of $\Delta OLR*$ is due to clear-sky processes and reflects the anticipated meridional structure of the surface temperature response to enhanced CO_2 concentrations with Arctic amplification in the NH and reduced warming over the SH extratropics. As a consequence, the ensemble spread in $\Delta OLR*$ is highly correlated ($R^2 = 0.79$) with the change in the equator-to-pole gradient of surface temperature, $TS*$, when both hemispheres are considered simultaneously.

3.4.5.3 Changes in MHT_{MAX}

The change in MHT_{MAX} due to CO_2 doubling (hereafter ΔMHT_{MAX}) is not significantly different from zero in either hemisphere; the inter-model average ΔMHT_{MAX} is more than a factor of three smaller than the spread in ΔMHT_{MAX} and is more than an order of magnitude smaller than the inter-model spread in MHT_{MAX} in the PI simulations that

were previously discussed.

ΔMHT_{MAX} is equal to the difference between ΔASR^* and ΔOLR^*. As such, we can understand the ensemble behavior of ΔMHT_{MAX} in terms of the statistics of ΔASR^* and ΔOLR^* that were previously discussed. We demonstrated that ΔASR^* varies widely between ensemble members due to the large uncertainty in the cloud response and that the ensemble average (and spread of) ΔOLR^* is small (as compared to the ΔASR^* spread) and follows the anticipated clear-sky response to the meridional structure of surface temperature change. As a consequence, the inter-model spread in ΔMHT_{MAX} is well correlated with ΔASR^* ($R^2 = 0.68$ in the NH and 0.82 in the SH) and is insignificantly correlated with ΔOLR^*. Furthermore, the robust ensemble average ΔOLR^* and $\Delta ASR^*{}_{SURF}$ are overwhelmed by the large spread in $\Delta ASR^*{}_{ATMOS}$ resulting in a ΔMHT_{MAX} that is ambiguous in sign between the different models. This point is summarized in Fig. 3.10c which shows the contours (colors) of ΔMHT_{MAX} in the ΔASR^*-ΔOLR^* plane. In the NH, all ensemble members have negative ΔOLR^* (are below the zero axis) that would lead to enhanced MHT_{MAX} (shift towards red contour values) in the absence of ASR^* changes. However, the spread in ΔASR^* (spread along the axis) results in ΔMHT_{MAX} max that spreads across the zero ΔMHT_{MAX} contour (the thick black line). This result suggests that the more predictable climate feedbacks such as the surface albedo feedback and the Planck feedback associated with polar amplification have a small impact on the equator-to-pole gradient of radiative forcing (and hence, on the strength of the atmospheric and oceanic circulation) as compared to that of the more unpredictable shortwave cloud feedback.

Our diagnoses of the MHT from the TOA atmosphere radiative budget assumes that the climate system is in radiative equilibrium. This assumption is not valid; the TOA is out of radiative balance 150 years after CO_2 doubling and the atmosphere/ocean temperatures are still evolving toward their equilibrium temperatures. Therefore, ΔMHT_{MAX} assessed by our methodology includes the spatial divergence of heat storage in the ocean (and in the atmosphere, to a lesser extent) as well as genuine changes in the atmosphere and ocean heat transport. For example, ocean heat storage that is isolated to the extratropics would be

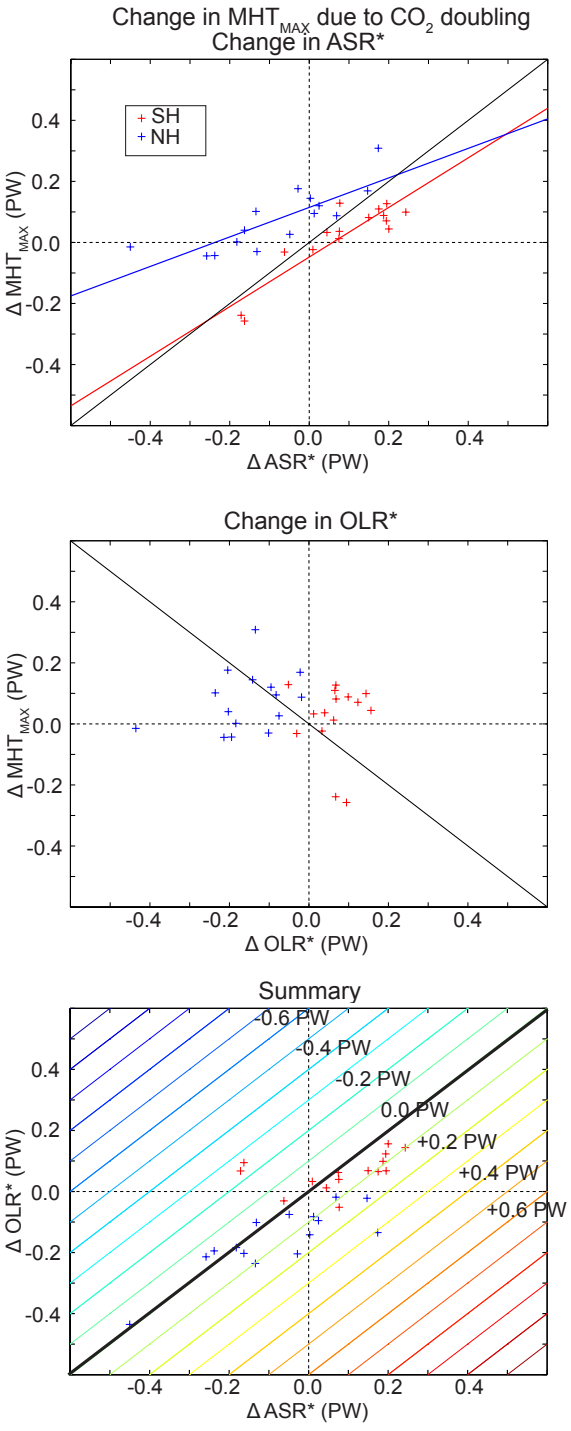

Figure 3.10: As in Fig. 3.9 except for (a) ΔMHT_{MAX} versus $\Delta ASR*$ (b) ΔMHT_{MAX} versus $\Delta OLR*$ and (c) $\Delta OLR*$ versus $\Delta ASR*$. The black line in (b) is the -1:1 line and can be intepreted as the expected $\Delta\mathrm{MHT}_{MAX}$ if there was no $\Delta ASR*$. The colored lines in (c) are the contours of ΔMHT_{MAX} and the thick black line in the zero contour

interpreted in our framework as a divergence of ocean heat transport over the polar cap and a negative oceanic contribution to ΔMHT_{MAX}. Indeed, there is a robust ensemble average increase in atmospheric heat transport in both hemispheres that comes at the expense of reduced ocean heat transport/transient storage in the extratropics (Hwang and Frierson, 2011; Held and Soden, 2006). It is unclear whether the decrease in heat transport reflects a genuine change in the ocean heat transport or merely the spatial structure of transient heat storage; it is possible that the enhanced atmospheric heat transport is a transient effect that does not persist in the equilibrium climate (Hwang et al., 2011). The point we emphasize here is that, in order to change the total heat transport in the equilibrium case, the meridional structure of the radiative fields must change. In this study, we have demonstrated that the uncertainty in the shortwave cloud feedback overwhelms the changes that are robust across the ensemble members (i.e. the surface albedo feedback or the anticipated polar amplification) in determining the change in meridional heat transport due to CO_2 doubling.

3.5 Summary and Discussion

The peak *MHT* in the climate system was diagnosed as the difference between the equator-to-pole gradient of *ASR* (ASR^*) and *OLR* (OLR^*). 65% (59%) of the observed ASR^* in the NH (SH) is a consequence of the meridional distribution of incident solar radiation at the TOA while the remaining 35% (41%) is due to the meridional distribution of planetary albedo. We have demonstrated that the vast majority (86% and 94% in the NH and SH) of the meridional gradient of planetary albedo is a consequence of atmospheric as opposed to surface reflection. These results suggest that surface albedo plays a significantly smaller role in setting equator-to-pole gradient in *ASR* than atmospheric reflection (e.g. cloud distribution).

The total equator-to-pole gradient in absorbed solar radiation, *ASR*,* and its partitioning into atmospheric and surface albedo components found in the observations is well replicated in the multi-model mean of the CMIP3 PI model simulations in the NH. How-

ever, in the SH, the ensemble average ASR^* is smaller than that observed due to a smaller than observed equator-to-pole gradient in $\alpha_{P,ATMOS}(ASR^*_{ATMOS})$. As a consequence, the ensemble average MHT_{MAX} is 0.6 PW smaller than the observed value in the SH.

The CMIP3 simulations of the PI climate system exhibit a remarkably large spread (of order 1 PW or 20%) in MHT_{MAX} that exceeds the projected change under global warming by a factor of approximately five (Hwang and Frierson, 2011). This spread is due to inter-model differences in the equator-to-pole gradient in ASR (ASR^*) and is uncorrelated with inter-model differences in the equator-to-pole gradient in OLR (OLR^*). The inter-model spread in ASR^* results from model differences in the meridional gradient of α_P that are primarily (94%) due to differences in cloud reflection ($\alpha_{P,ATMOS}$). As a consequence, total heat transport in the climate models is primarily determined by the optical properties of the atmosphere (Fig. 3.6); inter-model differences in cloud reflection of shortwave radiation explain 84% of the inter-model spread in MHT_{MAX} in the SH and 63% of the spread in NH (Table 3.3). Our definition of MHT_{MAX} in terms of ASR^* and OLR^* is useful tool for analyzing the MHT_{MAX} and its inter-model spread because the meridional contrast of ASR and OLR are governed by different physical processes in the models; ASR^* is primarily controlled by cloud reflection where as cloud fraction, cloud structure, and surface temperature all contribute to OLR^*.

Our results indicate that, in the present climate, the peak MHT_{MAX} is mainly determined by the shortwave optical properties of the atmosphere (i.e., cloud distribution) and suggests that MHT_{MAX} is largely insensitive to subtleties in the model dynamics that contribute to the heat transport (Stone, 1978). We can understand this result in the context of simplified energy balance models. In the annual mean, the extratropical deficit in ASR, ASR^*, is balanced by the sum of OLR anomalies relative to the global mean (OLR^*) and meridional heat transport into the extratropics (MHT_{MAX}). If the heat transport is diffusive along the surface temperature gradient and the OLR anomaly is proportional to the surface temperature anomaly from the global mean (as in Budyko, 1969; Sellers, 1969, amongst others) then both the extratropical OLR anomaly and MHT_{MAX} are proportional

to the same equator-to-pole temperature gradient. The ratio between MHT_{MAX} and OLR^* is then dictated by the relative efficiencies of large scale heat diffusion and radiation to space which is commonly called δ in the literature (see Rose and Marshall, 2009, for a review). If two climate models had different δ values yet the same ASR^*, MHT_{MAX} would differ between the models and the inter-model spread in ASR^* and OLR^* would be anti-correlated. For example, a more diffusive model (e.g. a model with more vigorous baroclinic eddies) would have more MHT_{MAX} and less OLR^* and vice versa. In contrast, if δ were nearly equal among climate models but ASR^* varied, then the MHT_{MAX} and OLR^* would be proportional to ASR^* with a regression coefficient dictated by the relative efficiency of dynamic and radiative heat exports (equal to $\frac{\delta}{\delta+1}$ and $\frac{1}{\delta+1}$ – Donohoe and Battisti, 2011b). The positive correlation between ASR^* and OLR^* (Fig. 3.3c) suggests that the CMIP3 suite of climate models all have a similar δ value such that MHT_{MAX} is dictated by ASR^* which in turn, we have demonstrated is controlled by the meridional distribution of the simulated clouds. Furthermore, the relatively steep slope between MHT_{MAX} and ASR^* (a regression coefficient of 0.64 in the NH and 0.85 in the SH – Fig. 3.3a) as compared to the relatively shallow slope between OLR^* and ASR^* (a regression coefficient of 0.36 in the NH and 0.15 in SH– Fig. 3.3c) suggests that δ is greater than unity; the dynamic export of heat out of the tropics (MHT_{MAX}) is a more efficient pathway for achieving local energy balance than is the radiative export of energy anomalies (OLR). Thus, per unit ASR^* anomaly imposed by the modeled cloud distribution, the extratropical energy budget will be balanced primarily by a MHT_{MAX} anomaly and secondarily by an OLR^* anomaly. These ideas are further explored in the conclusion of this thesis (Chapter 5).

Chapter 4

A HEURISTIC MODEL OF THE SEASONAL CYCLE IN ENERGY FLUXES AND CLIMATE

4.1 Introduction

A fundamental property of the Earth's climate system is the equator to pole gradient in solar insolation entering the atmosphere, leading to a gradient in absorbed solar radiation (ASR). While some of the gradient in solar radiative heating is ameliorated by the equator to pole gradient in the outgoing longwave radiation (OLR), the latter gradient is substantially weaker than the former (Fig. 4.1a) leading to regions of net radiative gain in the tropics and loss in the extratropics. Ultimately, almost all atmospheric and oceanic motions derive their energy from gradients in net radiation. In the annual mean there can be no net energy storage in a stable climate system and the top of atmosphere net radiative surplus (deficit) over the tropics (extratropics) most be exactly balanced by energy export (import) by way of atmospheric and oceanic motions. From the perspective of the atmosphere, the annual mean oceanic heat transport divergence manifests itself as an annual mean surface heat flux (SHF) and plays a substantially smaller role in the high latitude energy balance than does the atmospheric heat flux divergence.

The dominant spatial pattern in the top of atmosphere radiation – and hence in the atmospheric and oceanic heat flux divergence – is an equator to pole gradient. Hence, it is convenient to spatially integrate each quantity over equal area domains equatorward and poleward of 30° which we will define as the tropics and the extratropics, and subtract the global annual average. In the annual average (Table 4.1, first row), for example, the Northern Hemisphere (NH) extratropics receive a 7.9 PW deficit of ASR, relative to the global average. This deficit is partially offset by an OLR deficit of 2.2 PW that acts as an effective energy gain. The regional energy balance therefore requires an atmospheric and oceanic

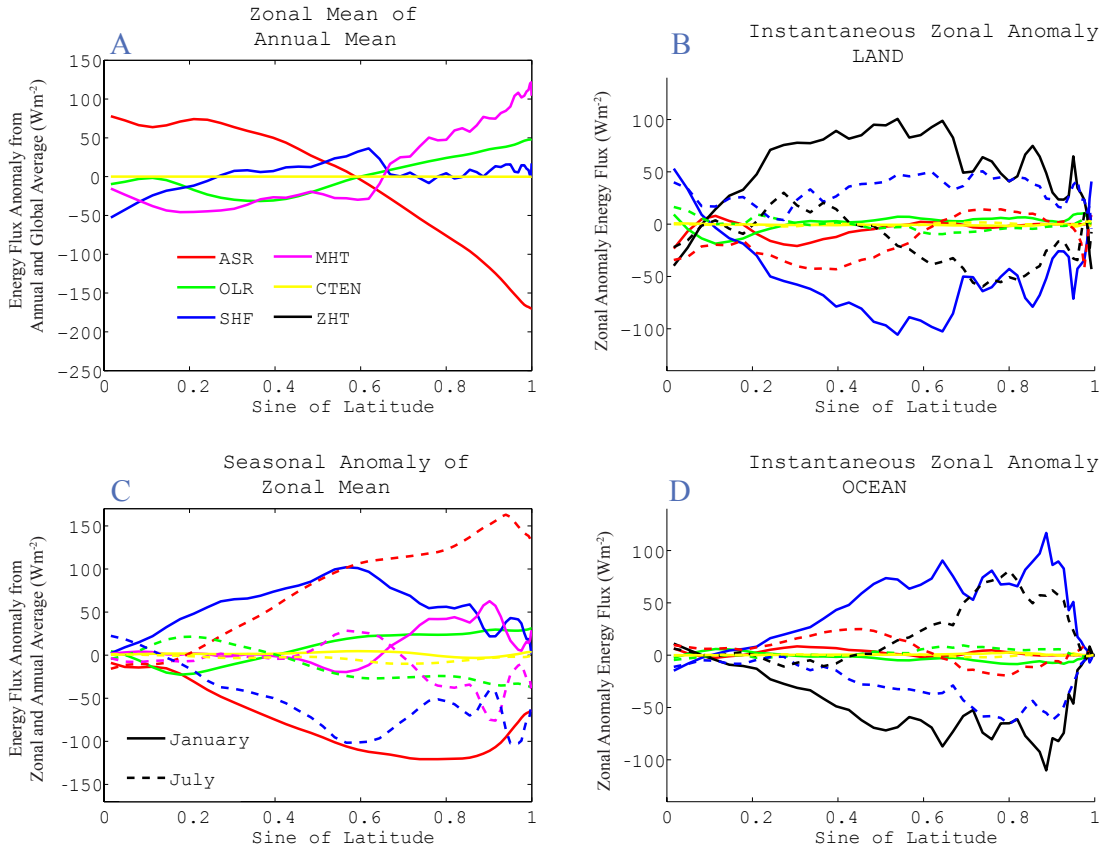

Figure 4.1: (a) Zonal and annual averaged energy flux for ASR (red), OLR (green), SHF (blue), MHT (magenta), and CTEN (yellow). The global and annual average has been removed from each term. (c) Zonal averaged, seasonal anomaly energy flux for January (solid lines) and July (dotted lines). Energy flux terms separately over (b) land and (d) ocean areas for January (solid lines) and July (dotted lines). The zonal averaged heat flux divergence has been removed from all terms in (b) and (d). Also shown in (b) and (d) is the zonal heat flux (ZHT, black) over land and ocean, respectively. Data is for the Northern Hemisphere, and data sources are noted in Section 4.2.3

heat transport divergence of 5.7 PW; this is equivalent to the total heat transport across 30°N by Gauss's Theorem: 4.3 PW coming from atmospheric meridional heat transport (MHT) and the remaining 1.4 PW entering the atmosphere by way of an annual mean SHF resulting from meridional ocean heat transport.

On seasonal time scales, the extratropics experience modulations in incoming solar radiation that are comparable in magnitude to the annual average insolation received in those regions; high latitude regions receive little or no solar insolation during the winter and upwards of 500 W/m^2 of daily mean insolation during the summer (150% of the globally averaged value and the maximum daily mean insolation value of anywhere on the planet). In contrast to the annual mean energy balance, the climate system does not achieve a balance between net radiation and meridional heat transport on seasonal time scales: energy is stored in either the surface (land or ocean) or the atmospheric column. For example, during the summer when the high latitudes absorb more solar insolation (than their annual mean value), a pseudo energy balance[1] can be achieved by: (i) increasing OLR and thus reducing the net radiation, (ii) reducing the atmospheric meridional heat transport, (iii) storing energy in the atmospheric column, thereby inducing a column averaged temperature tendency (CTEN), or (iv) storing energy beneath the surface/atmosphere interface (i.e. in the ground or ocean) by way of a SHF anomaly. The climatological and zonal averaged structures of these terms are shown for January and July in Fig. 4.1c, after removal of the zonal and annual averaged value from each term. We note that the seasonal imbalances are of comparable magnitude to the annually averaged balance and that the predominant high latitude balance is achieved between excess ASR being balanced by changes in SHF with adjustments in OLR and MHT playing a secondary role and CTEN anomalies being approximately an order of magnitude smaller. In the framework of our extratropical and tropical regions, the extratropical seasonal ASR anomalies are of order 15 PW, and are

[1]We use the term pseudo energy balance to refer to the fact that the system is not in equilibrium and is gaining or losing energy on seasonal time scales. We therefore define a closed system with respect to the atmosphere by including a term that accounts for negative the vertically integrated atmospheric energy tendency, or the energy that is stored locally.

balanced by compensating anomalies in SHF, OLR, MHT and CTEN in an approximate ratio of 9:3:2:1. Understanding the relative magnitudes and controls of the seasonal energy partitioning amongst these processes on a global scale is the basis of this paper.

In addition to the large anomalies in the zonally averaged seasonal energy fluxes, there are equally large seasonal departures in the zonal anomaly energy balances over the land and ocean at a common latitude (Fig. 4.1c and d). Because the heat capacity of the ocean mixed layer (the layer that changes temperature seasonally) is much greater than that of the land surface layer, the majority of the seasonal energy storage and therefore the seasonal anomalies in SHF occur over the ocean. Consequently, the seasonal cycle of atmospheric temperature over the ocean is strongly buffered, leading to a warmer atmosphere over the ocean as compared to the atmosphere over land at the same latitude during the winter and vice versa during the summer. Furthermore, because the atmosphere is remarkably efficient at transporting mass and heat zonally, there is a large seasonal cycle in the zonal energy flux down the land-ocean temperature gradient. For example, during the winter, the atmosphere overlaying the extratropical ocean receives 8 PW more SHF from the ocean than the atmosphere overlaying the extratropical land mass receives from the land; this excess surface heat flux over the ocean is balanced a nearly equivalent quantity of zonal energy export to the land (Table 4.1).

The annually averaged energy balance has been studied extensively and both the fundamental constraints on the system and the balance achieved by the Earth are well documented in the literature. Stone (1978) realized that, because the meridional structure of solar-insolation and the outgoing longwave radiation (dictated by the local temperature) is dominated by the equator to pole gradient, the heat transport must be smooth and peaked in the mid-latitudes in order to achieve a balance with the net radiation. However, given a specified equator to pole gradient in solar insolation, these *a priori* constraints say very little about the relative magnitude of total heat transport and outgoing longwave radiation gradients (Enderton and Marshall, 2009) ; in the context of the extratropical domain defined in this paper, while the 7.9 PW deficit in ASR must equal the sum of total heat transport

		Spatially Integrated Energy Divergence (PW)					
		ASR	-OLR	SHF	MHT	ZHT	-CTEN
Annual and area averaged minus global annual average	Annual	-7.9	2.2	1.4	4.3		0
January minus annual average	January	-13.9	3	8.4	2.3		0.2
July minus annual average	July	15.8	-3.4	-9.8	-1.8		-0.8
Average over OCEAN minus average over land (instantaneous)	January	0.6	-0.8	8.6	0	-8.6	0.2
	July	-0.2	0.4	-5.2	0	5	0

Table 4.1: Energy flux terms spatially integrated over the Northern Hemisphere extratropics. Note that each term has been integrated over the extratropical domain, and so is reported here in PW.

and the extratropical OLR deficit, the relative partitioning of the latter two is unknown *a priori* and determined by their relative sensitivities to temperature gradients. Trenberth and Caron (2001b) and Wunsch (2005) have documented the balance in the Earth's climate system and find that approximately 5.5 PW of heat is transported across 35^0, in fair agreement with our values from Table 4.1 over a slightly different domain. This suggests that the meridional heat transport is more sensitive to temperature gradients than outgoing longwave radiation; we will re-examine this point in the body of the text.

On seasonal time scales, less theoretical and observational work has appeared in the literature. Fasullo and Trenberth (2008a) have documented the seasonal cycle of the global mean energy balance, the meridional structure of the energy fluxes (Fasullo and Trenberth, 2008b) including the associated observational errors and seasonal balances over the land and ocean separately. We take these calculations as a foundation for the present work and attempt to understand, in a highly simplified framework, what dynamical and radiative processes control the seasonal cycle of the radiative and dynamical energy fluxes between

the various components of the climate system. Furthermore, we ask which of the dominant seasonal energy balances are dictated by the physics of the system versus the specific geometry of the Earth's climate system. Our tool of choice for these tasks is a seasonal energy balance model (EBM), linearized about a global annual mean basic state.

EBMs have been used extensively to study the annual mean climate system (e.g., Budyko, 1969; Sellers, 1969; North, 1975) and the seasonal climate (e.g., Sellers, 1973; North and Coakley, 1978; Thompson and Schneider, 1979). These models are useful because they reduce the climate system to a minimal number of control parameters and diagnostic variables, thus making the model behavior (in our case, the flow of energy) easily tractable. Our seasonal EBM adopts similar elements to those previously documented but has a simplified meridional structure, allowing us to isolate the equator-to-pole scale seasonal energy processes and illuminate the sensitivity of those processes to model parameters. Our focus is more on the seasonal, global scale flow of energy in the system, as discussed in this section, and less on the intricate meridional structures.

The outline of the paper is as follows. We describe the EBM and additional data used in this work in Section 4.2. In Section 4.3, we document aquaplanet simulations with our energy balance model and compare the seasonal energy flow to slab ocean aquaplanet atmospheric general circulation model (AGCM) simulations with different ocean depths. In Section 4.4, we explore the implications for climate of the seasonal cycle of energy flow between the land and ocean domains and the sensitivity of the climate to the specified fractional land cover. A summary and discussion follows.

4.2 Models and data sets used in this Chapter

We describe in Subsection 4.2.1 below the zonally symmetric aquaplanet seasonal EBM used in this study as well the seasonal EBM that includes a simple representation of land-ocean contrasts (further details are provided in Appendix C). We then briefly describe an aquaplanet AGCM that is coupled to a slab ocean to complement the results from the aquaplanet EBM in Subsection 4.2.2. The data sets used in this study are listed in

Subsection 4.2.3.

4.2.1 Seasonal energy balance models

The physics and numerics of the EBMs are briefly documented in this subsection. The parameterizations chosen are based on linear regressions between the EBM variables (surface and atmospheric temperatures) and the energy fluxes in the observational record or, in some cases, in GCM simulations; a more detailed description of all the parameterizations is provided in Appendix C.

4.2.1.1 Single comuln basic state

The zonally symmetric (aquaplanet) and zonally asymmetric (incorporating land-ocean contrasts) EBMs are cast as (linear) anomaly models about a basic resting state atmosphere that is in radiative-convective equilibrium with the annual, global mean absorbed solar radiation (239 W m^{-2}). In the vertical, the energy balance model consists of three atmospheric levels and a single surface layer. The emissivity (ε) of each atmospheric layer is determined by the local temperature, an assumed fixed relative humidity of 75% and, CO_2 concentration of 350 ppm according to Emanuel (2010) parameterization. The basic state is calculated assuming the following: (i) the prescribed absorbed solar radiation is absorbed entirely at the surface; (ii) the surface layer behaves as a black body, absorbing all of the incident longwave radiation from the atmospheric layers and emitting radiation according to the surface temperature's Planck function; (iii) each atmospheric layer absorbs and emits longwave radiation according to its emissivity (and equivalent absorbtivity).

The latent heat flux (LH) between the surface and the atmosphere is parameterized as

$$LH = B_{LH}(T_S - C_{LH}), \tag{4.1}$$

where T_s is the surface layer temperature B_{LH} is 4 W m^{-2} K^{-1} and C_{LH} is 270 K (see Appendix C for details on the values of these and other parameterizations and coefficients).

This flux is removed from the surface layer and distributed in a 9:9:2 ratio amongst the lowest, middle, and highest atmospheric layers, roughly mimicking tropical observations (S. et al., 2006). Similarly, the sensible heat flux (SENS) is parameterized as

$$SENS = B_{SENS}(T_S - T_{A1} - C_{SENS}), \tag{4.2}$$

where T_{A1} is the lowest atmospheric layer temperature, B_{SENS} is 3 W m^{-2} K^{-1} and C_{SENS} is assessed to be 6 K from the data using 900 hPa as the reference level for the lowest atmospheric layer (Appendix C) but is adjusted to 24 K in the model (because our lowest level is higher in the atmospheric column). The sensible heat flux operates between the surface layer and lowest atmospheric layer only.

The single column atmosphere produces a basic state that is in radiative-convective equilibrium with the annual, global mean absorbed solar radiation (239 W m^{-2}) that has the following temperature structure:

$$\overline{T_S} = 287K, \overline{T_{A1}} = 262K, \overline{T_{A2}} = 248K, \overline{T_{A3}} = 225K. \tag{4.3}$$

The corresponding surface energy balance is +239 W m^{-2} ASR, -170 W m^{-2} net longwave radiation, –69 W m^{-2} latent heat flux, and negligible sensible heat flux with the signs defined relative to the surface layer. The lower, middle, and highest atmospheric layers have emissivities of 0.66, 0.38, and 0.29 respectively. This system represents a simplified global annual mean radiative convective balance. Next, we linearize the EBM about this basic state to form the seasonal zonally symmetric (aquaplanet) and asymmetric (land-ocean contrast) EBMs.

4.2.1.2 Linearized three-box (aquaplanet) energy balance model

We now build a model consisting of three meridional boxes representing the tropical and extratropical regions on a spherical planet with boundaries at 30°N and 30°S. Each meridional box has three atmospheric layers and a surface layer, linearized about the global annual

	$[B_{OLR}]$	$B_{LW\uparrow,S}$	B_{SENS}	B_{LH}	B_{MHT}	B_{ZHT}	$[B_{LW\downarrow}]$	$[B_{LW\uparrow}]$
Coefficient value ($Wm^{-2}K^{-1}$)	2.6	5.3	3	4	3.4	10	2.2	1.9

Table 4.2: Summary of sensitivity coefficients used in the seasonal EBM.

mean basic state described in the previous section. The layer emissivities are fixed at their basic state values. The anomalous longwave radiation (LW') emitted by each layer takes the form of

$$LW_N^{'} = C_{WV}\varepsilon_N 4\sigma\overline{T_N}^3 T_N^{'} \equiv C_{WV}\varepsilon_N B_{OLR,N} T_N^{'}, \tag{4.4}$$

where σ is Planck's constant $\varepsilon_N$is the layer's emissivity (unity for the surface), $B_{OLR,N}$ is the local change in emitted longwave radiation per unit change of temperature (units of W m^{-2} K^{-1}) expected from the Planck function and $C_{WV}$is a water vapor feedback factor (0.65 in the atmospheric layers and 1.0 at the surface) intended to capture the water vapor feedback as discussed in Appendix C. If an entire region were to warm uniformly in the vertical, the change of OLR with temperature is 2.6 W m^{-2} K^{-1}, a value we will denote by *[B_{OLR}]* (brackets represent a vertical average); approximately 30% of the radiation escaping to space originates from the surface layer. This value is analogous to our model's inverse climate sensitivity and is slightly higher than other values published in the literature (see Warren and Schneider, 1979, for a review).

The linearized SENS and LH fluxes do not depend on C_{LH} and C_{SENS}, so all of the surface energy flux anomalies are given by the surface temperature perturbations times the parameters B_{LH} and B_{SENS}; these can be readily by compared to the efficiency of surface longwave radiation loss, $B_{LW\uparrow,S}$, of 5.3 W m^{-2} K^{-1} (Table 4.2) to assess the relative magnitudes of surface radiative, latent heat flux and sensible heat flux anomalies[2].

The heat transport between the tropical and extratropical boxes is by horizontal diffusion

[2]The values of C_{LH} and C_{SENS} have no direct effect on the linearized EBM since these terms only show up in the basic state equations and are therefore removed from the linearized system.

between the atmospheric layers in adjacent boxes. The vertically averaged atmospheric energy transport divergence reduces to the expression

$$MHT_{N,S} = B_{MHT}\left(\left[T'_T\right] - \left[T'_{N,S}\right]\right), \tag{4.5}$$

where the subscripts refer to the northern (N) and southern (S) extratropical and tropical (T) regions respectively, the brackets denote a vertical average, and B_{MHT} is the diffusive coefficient, equal to 3.4 W m^{-2} K^{-1} corresponding to a diffusion value (D) of 0.95a ^{2} W m^{-2} K^{-1} (a is the Earth's radius) as described in Appendix C.

The ocean mixed layer depth is pre-specified in each set of experiments (we will explore the model sensitivity to this parameter in 4.3.2) and each atmospheric layer has an equal mass and therefore heat capacity. The model is initialized at the boreal autumnal equinox and run forward with time varying solar insolation for several years until it converges to steady seasonal cycle. We compute the amplitude of the seasonal cycle as the amplitude of the annual harmonic.

4.2.1.3 Linearized, six-box energy balance model that includes land-ocean contrast

We take the 3-box model described in the previous Subsection and divide each meridional box into ocean and land subdomains, with specified land fractions. The linearized column energetics are unchanged from before except that the latent heat flux over land is set to zero. The MHT is assumed to be zonally invariant and is determined from atmospheric temperatures, zonally averaged over the land and ocean subdomains.

The atmosphere over the land and ocean sub-domains at the same meridian communicate by way of a zonal heat flux divergence:

$$ZHT_{O,L} = \frac{B_{ZHT}\left([T_{L,O}] - [T_{O,L}]\right)}{F_{O,L}}, \tag{4.6}$$

where the subscripts refer to the ocean (O) and land (L) subdomains at the given meridian, B_{ZHT} has a value of 10 W m^{-2} K^{-1} (see appendix C.5), and $F_{O,L}$ is the ocean or land

fraction in each meridional domain. By definition, the zonal heat flux between the ocean and land and vice versa, must be equal an opposite. However, the zonal heat flux divergence, which is more relevant for the local energetics, scales inversely as the fractional area of surface type. The land surface layer is given a heat capacity of one third of the atmospheric column and we fix the ocean mixed layer depth at 60 meters in this series of experiments. The control six-box run specifies land fractions (F_L) of 10%, 25%, and 50% in the southern extratropical, tropical, and northern extratropical regions respectively, mimicking the Earth. Experiments in Section

4.2.2 Aquaplanet atmospheric general circulation model (AGCM) simulations

We utilize an ensemble of aquaplanet AGCM simulations coupled to a slab ocean for comparison to our EBM predictions in Section 4.3. The ensemble members have prescribed slab ocean depths of 2.4, 6, 12, 24, and 50 meters. The model integrations are preformed with the Geophysical Fluid Dynamics Lab Atmospheric Model version 2.1 (Delworth et al., 2006) featuring a finite volume dynamical core (Lin, 2004) with M45 L24 resolution. Each model is forced by seasonally varying solar insolation with zero eccentricity and 23.439° obliquity, and is run for ten years which is sufficient to converge on a steady climatology. The model climatology is taken from the last five years of the integrations. The heat transport divergence is calculated as the residual of the sum of the net radiation, surface energy flux (SHF), and (minus) the storage term CTEN.

4.2.3 Observational data

The radiation data used in the introduction to this Chapter (4.1) and for comparison in Section 4.4 is from ERBE satellite data (Barkstrom and Hall, 1982) and has been adjusted for discontinuities in the observational system and diurnal aliasing (Fasullo and Trenberth, 2008a). The atmospheric heat transport and integrated column energetics are taken from updated calculations (http://www.cgd.ucar.edu/cas/catalog/) preformed by the National Center for Atmospheric Research according to methodology of Trenberth and Caron (2001a);

we utilize fields that are derived from the National Center for Environmental Prediction reanalysis data to compute the observed seasonal energetics. The surface heat flux climatology is determined from the residual of the column energy tendency, top of the atmosphere net radiation, and heat flux convergence. All quantities discussed in the subsequent sections and figures are spatially averaged equatorward and poleward of 30°.

4.3 Aquaplanet simulations from the energy balance model and AGCM

In the introduction, it was shown that seasonal cycle in energy fluxes to the extratropical atmosphere is dominated by large amplitude oscillations in ASR, compensating oscillations in SHF of comparable magnitude, and changes in MHT, OLR, and CTEN playing a decreasingly important role in the regional seasonal energetics. We now attempt to answer the following questions:

(i) Why is the predominant seasonal balance in the observed climate system between ASR and SHF?

(ii) Can we imagine a climate system where the seasonal cycle of ASR is mostly balanced by another term (for example, OLR or MHT)?

(iii) What parameters control the partitioning of energy fluxes?

(iv) What controls the seasonal cycle of atmospheric and surface temperatures?

We force the linearized EBM with seasonally varying absorbed shortwave radiation (details in Subsection 4.3.2) and examine the seasonal cycle of energy fluxes. We begin our analysis with a brief discussion of the annual mean energy balance. We then present the temperature and energetics climatology as a function of ocean mixed layer depth in our aquaplanet EBM and the aquaplanet AGCM simulations.

4.3.1 Annually averaged energy balance

In the annual mean, there can be no heat storage in either the surface layer or atmospheric column in an equilibrated climate system. Therefore, in our EBM, the prescribed global anomaly ASR in the extratropics of -7.9 PW must by balanced by meridional heat import

and the negative of OLR anomalies (OLR is an energy loss). The EBM steady state solution is independent of the layer's heat capacity and consists of 5.5 PW of meridional heat import and 2.4 PW of energy gain by anomalously low OLR. These values compare reasonably well with the observations (Table 4.1) although the latter is complicated by both land-ocean contrast and ocean heat transport.

What determines the ratio of MHT to OLR anomalies in maintaining the extratropical annual mean energy balance? If we assume that all four vertical layers in both North and South extratropical regions have the same global temperature anomaly, ΔT, global mean energy balance then requires that the tropical layers have an equal and opposite temperature anomaly (so global mean OLR is unchanged). If the annual mean system has minimal vertical structure, the MHT acts across a temperature difference of $2\Delta T$ where as the OLR anomaly is proportional to ΔT. This, coupled with the relative sensitivities of the respective MHT and OLR energy fluxes to temperature anomalies, suggest that

$$\frac{\overline{MHT}}{\overline{OLR}} \approx \frac{2B_{MHT}}{[B_{OLR}]} = \frac{7.5(\frac{D}{a^2})}{[B_{OLR}]} = 2.6, \tag{4.7}$$

where D is the temperature diffusivity of the system[3]. The ratio 2.6 is close to the actual value from the EBM of 2.3: the difference is due to the vertical structure in the true steady state solution which has larger temperature anomalies at the surface than those aloft (ΔT is 8.6 K for the surface and 6.4 K averaged over the atmosphere). This ratio plays a critical role in determining whether the system reaches a diffusive or a radiative equilibrium; in the limits of D approaching zero and infinity, the annual mean heat transport into the extratropics is 0 and 7.9 PW, respectively.

4.3.2 Seasonal temperatures and energy fluxes

It is widely recognized that the thermal inertia of the ocean plays a critical role in buffering the seasonal cycle of atmospheric and surface temperature (e.g., Hartmann, 1994). We

[3]The conversion between D and B_{MHT} is discussed in Appendix C.4

explore the role of ocean heat storage on seasonal energetics in an ensemble of aquaplanet EBM and AGCM simulations with varying ocean mixed layer depths. The seasonal cycle of solar insolation in the GCM runs has no precessional cycle. The seasonal ASR anomalies used to force the EBM are prescribed from a Fourier expansion of the 12 meter depth GCM seasonal ASR anomalies, averaged over each meridional domain, truncated at the semi-annual component (inclusive).

The amplitude of the seasonal cycle in surface and atmospheric temperatures decreases (roughly inversely) with mixed layer depth in the EBM; results from the aquaplanet GCM agree remarkably well with those from the EBM (Fig. 4.2a).

The amplitude and relative importance of the various energy flux terms that balance the ASR in the extratropics are also a strong function of the mixed layer depth (Fig. 4.2b). For deeper mixed layer depths, the seasonal cycle in ASR in the extratropic (amplitude 18.6 PW) is primarily balanced by SHF while, at shallower mixed layer depths, the seasonal cycle of MHT, OLR, and CTEN play a more prominent role in maintaining the seasonal pseudo energy balance. The seasonal amplitude of each energy flux term as a function mixed layer depth in the aqua planet GCM is qualitatively captured by the EBM simulations, as is the relative magnitude of one term compared to another term.

Understanding the qualitative behavior of the seasonal energy fluxes as the ocean deepens in the EBM is straightforward. All ASR anomalies go directly into the surface layer, and are only communicated to the atmospheric layers via latent, sensible, and radiative energy flux anomalies. Therefore, ASR anomalies only make their way to the atmosphere by heating the surface layer and consequentially changing the upward energy flux. As the ocean mixed layer deepens, more of the solar energy goes into heating the surface layer, appearing as a SHF anomaly to the atmosphere, and less of the solar energy enters the atmosphere, because the seasonal surface temperature anomaly is reduced.

The partitioning of the net energy entering the atmosphere into MHT, OLR, and CTEN is also readably understandable within our model framework. Ultimately, all atmospheric energy fluxes result from temperature anomalies within the atmosphere, with the magnitude

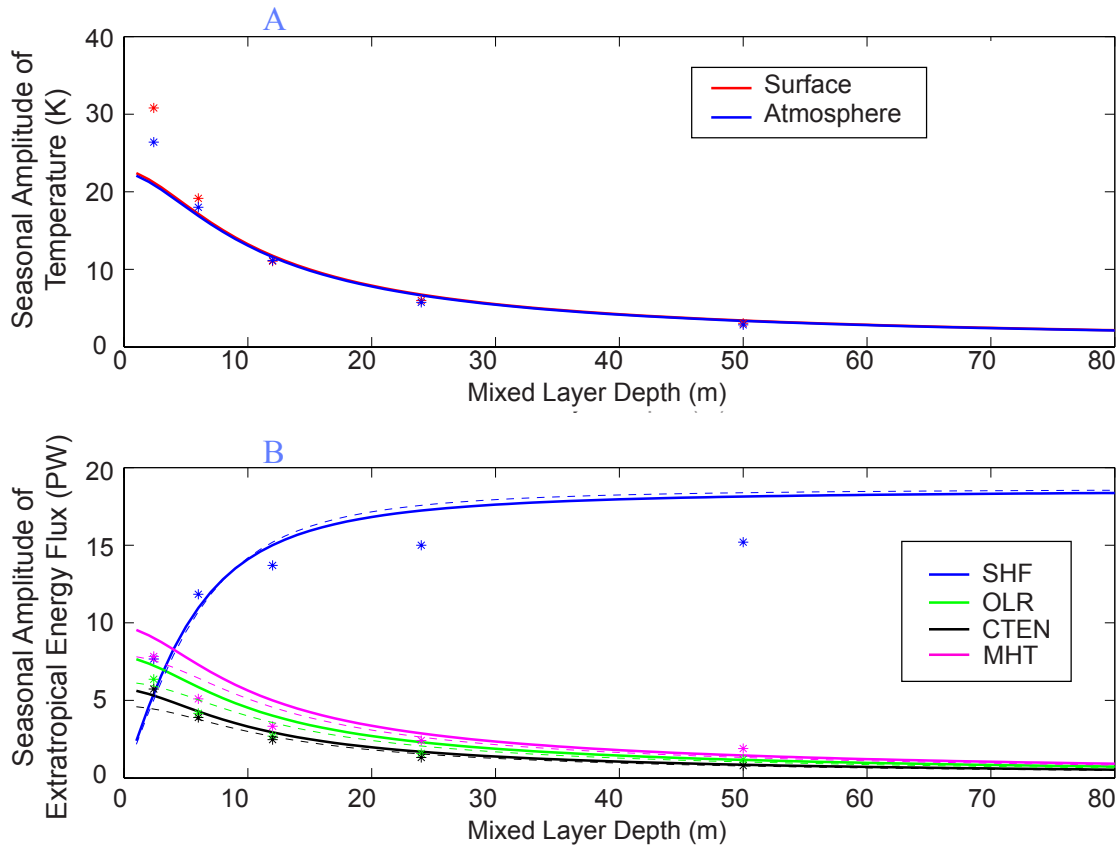

Figure 4.2: (a) Seasonal amplitude of surface and vertically averaged atmospheric temperature in the extratropics as a function of mixed layer depth in the ensemble of aquaplanet EBM runs. The solid lines are from the EBM, asterisks are the aqua-planet GCM simulation. (b) As in (a) except for the seasonal energetics in the extratropics. The dashed lines are discussed in Subsection 4.3.2.

of the various energy fluxes dictated by the B coefficients for the respective processes. The column tendency pseudo-energy flux complicates this framework because it is governed by temperature tendencies as opposed to temperature anomalies. We can compose an effective B_{CTEN} by assuming that the seasonal temperature cycle is composed entirely of the annual Fourier component. The derivative of the temperature scales as the amplitude of the temperature anomalies times the radial frequency of the annual cycle, resulting in

$$B_{CTEN} = \frac{2\pi[C_P]}{1 \text{ year}} = 2.0 \text{ W m}^{-2} \text{ K}^{-1}, \tag{4.8}$$

where C_P is the atmospheric heat capacity. The pseudo energy flux associated with CTEN will temporally lag the MHT and OLR signals, but only by a small phase as discussed later in this section. The relative amplitudes of the seasonal MHT:OLR:CTEN is then given by

$$MHT : OLR : CTEN = B_{MHT} : [B_{OLR}] : B_{CTEN}, \tag{4.9}$$

or approximately 7:5:4 in our model[4]. This relationship is remarkably consistent for all mixed layer depth EBM simulations. Furthermore, the aquaplanet AGCM ensemble also has a consistent MHT:OLR:CTEN seasonal amplitude ratio of approximately 14:11:10 in all the ensemble runs , suggesting that these linear ideas may be applicable to more complicated model integrations. The precise ratios of energy flux amplitudes differ between the EBM and aquaplanet AGCM. Most notably, the CTEN and OLR amplitudes are nearly equal in the AGCM, suggesting that the AGCM's *[B_{OLR}]* is closer to 2 W m^{-2} K^{-1} (since B_{CTEN} is essentially fixed by the atmospheric mass).

In the EBM, the ratio of the seasonal amplitude of the extratropical surface temperature to the atmospheric temperature is remarkably constant at 1.01; the same ratio in the aquaplanet AGCM has an average of 1.06 and varies slightly amongst the ensemble members (standard deviation of 0.06). We can understand these results in the model framework

[4]Note that we use B_{MHT} instead of $2B_{MHT}$ (as was used for the annual mean) because the tropical temperatures have a minimal seasonal cycle.

by first noting that the atmospheric temperatures are very nearly in pseudo-equilibrium with the energy input from the surface; in the absence of other energy inputs, atmospheric temperatures would approach equilibrium with an e-folding time scale of

$$\tau_{atmos} = \frac{[C_P]}{[B_{LW\uparrow}] + [B_{LW\downarrow}] + B_{MHT} + B_{SENS}} = 11 \text{ days}, \tag{4.10}$$

where $[B_{LW\uparrow}]$ and $[B_{LW\downarrow}]$are the change in upwelling and downwelling longwave radiation leaving the atmosphere per unit temperature change of the atmospheric column and have values of 1.9 and 2.2 W m^{-2} K^{-1} respectively (Table 2). Since the atmosphere is in pseudo-equilibruim on seasonal time scales, the input of energy into the atmosphere by way of the sensible heat, latent heat, and surface radiative fluxes must equal the export of energy from the extratropical atmosphere via longwave radiation, CTEN, and MHT. Assuming the seasonal tropical temperature changes are small, each of these quantities can be expressed in terms of either the surface or atmospheric temperature anomaly resulting in the expression

$$\frac{\left|T_S'\right|}{\left|[T_A']\right|} = \kappa = \frac{B_{SENS} + B_{MHT} + [B_{LW\uparrow}] + [B_{LW\downarrow}] + B_{CTEN}}{B_{SENS} + B_{LH} + B_{LW\uparrow,S}} = 1.0 \tag{4.11}$$

We can understand the physical basis of Eq. 4.11 by taking the not so hypothetical example of reducing the efficiency of surface heat export (the denominator of Eq. 4.11) by, say, reducing the LH feedback as would happen over a land surface. In this case, as the insolation heats up the surface, less energy is fluxed from the surface to the atmosphere (than with the LH feedback turned on). Consequently, more of the energy from ASR is retained in the surface and the seasonal amplitude of the surface temperature will increase; the component of the coupled system (surface and atmosphere) that is least efficient at exporting energy, will experience the largest temperature anomalies. The above argument is supported by experiments whereby the EBM parameters are tweaked and the κ values predicted by Eq. 4.11 are verified by the EBM integrations (not shown). The parameters of our aquaplanet EBM suggest that the atmosphere and ocean surface are nearly equally efficient at exporting heat, resulting in equal amplitudes of the temperature seasonal cycles. The aquaplanet

AGCM simulations also have atmosphere and surface temperature seasonal cycles that are nearly equivalent in magnitude. We will revisit this analysis using a more realistic system that includes zonal land-ocean contrast in Section 4.4 and find that atmosphere is substantially more efficient than the surface at exporting heat in the presence of zonal asymmetries in surface heat capacity.

We now attempt to understand the seasonal amplitudes of the various extratropical energy flux terms: the ocean storage, MHT, OLR, and atmospheric storage (BCTEN). To begin, we calculate the amplitude of the energy tendency within the ocean mixed layer per unit of temperature change, approximating the temperature anomalies as the annual harmonic:

$$B_{OC} = \frac{2\pi \mathrm{C}_{H_2O}\rho_{H_2O}H}{1 \text{ year}}. \tag{4.12}$$

As the ocean warms seasonally, it fluxes more energy to the atmosphere above and the atmosphere comes into equilibrium fairly rapidly, balancing the enhanced energy input radiatively, dynamically, and through storage. The ocean heat uptake and surface heat flux to the atmosphere is in phase quadrature, because the ocean cannot flux additional heat to the atmosphere until the ocean heats up. In contrast, the seasonal cycle in the atmospheric terms (CTEN, MHT, and OLR) are nearly in phase with each other. Taking into account these phase relationships, the seasonal amplitudes of all the energy fluxes must sum to the prescribed seasonal amplitude of extratropical ASR anomalies:

$$|ASR|'^2 = (B_{CTEN} + B_{MHT} + [B_{OLR}]^2)|T_A'|^2 + B_{OC}^2|T_S'|^2 \tag{4.13a}$$

$$= |T_A'|^2[(B_{CTEN} + B_{MHT} + [B_{OLR}])^2 + (KB_{OC})^2] \tag{4.13b}$$

where straight brackets denote the seasonal amplitude. The second equality (Eq. 4.13b) follows from application of Eq. 4.11. The first and second terms in the brackets of Eq. 4.13a can be identified as the quantity of seasonal energy that enters the extratropical atmosphere

to drive seasonal changes in MHT, CTEN, and OLR and the quantity of seasonal energy that is stored in the extratropical ocean. This equation ratio allows the amplitudes of SHF, MHT, OLR, and CTEN to be determined uniquely as a function of ocean mixed layer depth and the other model parameters. The amplitude of each of the seasonal energy flux terms using the pseudo steady state approximations (Equations 4.8-4.13) are shown in Fig. 4.2 (dashed lines), and are comparable to those from the EBM (solid lines) and the aquaplanet GCM simulations. The agreement between the pseudo-equilibrium predictions and the EBM output is not exact because the modeled atmosphere is not completely in steady state, especially for the simulations with a shallow ocean mixed layer. Nonetheless, the general agreement suggest that the ideas presented above are applicable to the EBM and that we can approximately solve for the systems behavior, given the model control parameters, without performing numerical integrations.

4.4 Land-ocean simulations with the six-box energy balance model

In the observations, zonal asymmetries in seasonal energetics that result from land-ocean contrasts are comparable in magnitude to the zonal mean seasonal energetics. Here, we explore these processes in our six-box EBM model framework. We start by looking at a control run, intended to simulate the land configuration in each hemisphere in the real world and forced by the observed seasonal cycle of ASR. In addition to analyzing the seasonal energetics over the land and ocean domains, we also ask how the different land fractions in the NH and Southern Hemisphere (SH) affect the globally averaged and zonal mean seasonal energetics. We then explore the impact of land and ocean fraction on the seasonal energy balance in an ensemble of EBM runs.

4.4.1 Globally averaged energetics

The planet currently receives more solar insolation during the boreal winter, when it is closest to the sun, corresponding to approximately 6 PW of additional insolation arriving at the top of the atmosphere (Berger, 1978). The seasonal cycle of global averaged ASR

is in phase with the incoming insolation but substantially smaller in magnitude (of order 3 PW) due to seasonal changes in the planets effective albedo[5] (Fasullo and Trenberth 2008a). Global mean OLR is in phase with Northern Hemisphere insolation (Fig. 4.3) and is therefore out of phase with the ASR, resulting in a net radiation into the climate system during boreal winter that exceeds the global ASR seasonal amplitude in magnitude. This radiative imbalance is primarily balanced by ocean heat uptake (SHF), with CTEN playing a smaller role.

Our land-ocean EBM qualitatively reproduces the phasing of the various components of the global mean seasonal energetics. In the NH, the enhanced land fraction causes a larger seasonal magnitude of surface temperature and greater seasonal heat flux to the atmosphere leading to larger seasonal magnitudes in OLR and CTEN than those in the Southern Hemisphere (SH), where most of the ASR enters the ocean mixed layer. Thus, the global mean OLR and CTEN phasing is essentially dictated by the hemispheric differences in land fractions, independent of the precessional phasing. We can verify this behavior in the EBM by shifting the precession by six months: the phasings of OLR and CTEN are unchanged (not shown) and the dominant global mean energy balance features an increased ASR during the boreal summer that is balanced by an increased OLR, with seasonal ocean heat storage playing a much smaller role. This experiment suggests that global averaged seasonal energetics may have been very different in different paleoclimate states.

4.4.2 Zonal mean energetics

The observed and EBM control simulation of the seasonal energy fluxes averaged over the land and ocean sub-domains in each meridional box are shown in Fig. 4.4. The asymmetry between Hemispheres is primarily due to the hemispheric differences in extratropical land fraction and, in small part, to the precessional signal in the prescribed ASR. Most notably,

[5]The seasonal cycle of effective, or insolation-area weighted, albedo is dominated by a semi-annual oscillation associated with the solar insolation shifting from the tropics to the extratropics where the albedo is larger. The seasonal cycle of *in situ* surface property changes make smaller contributions to effective albedo.

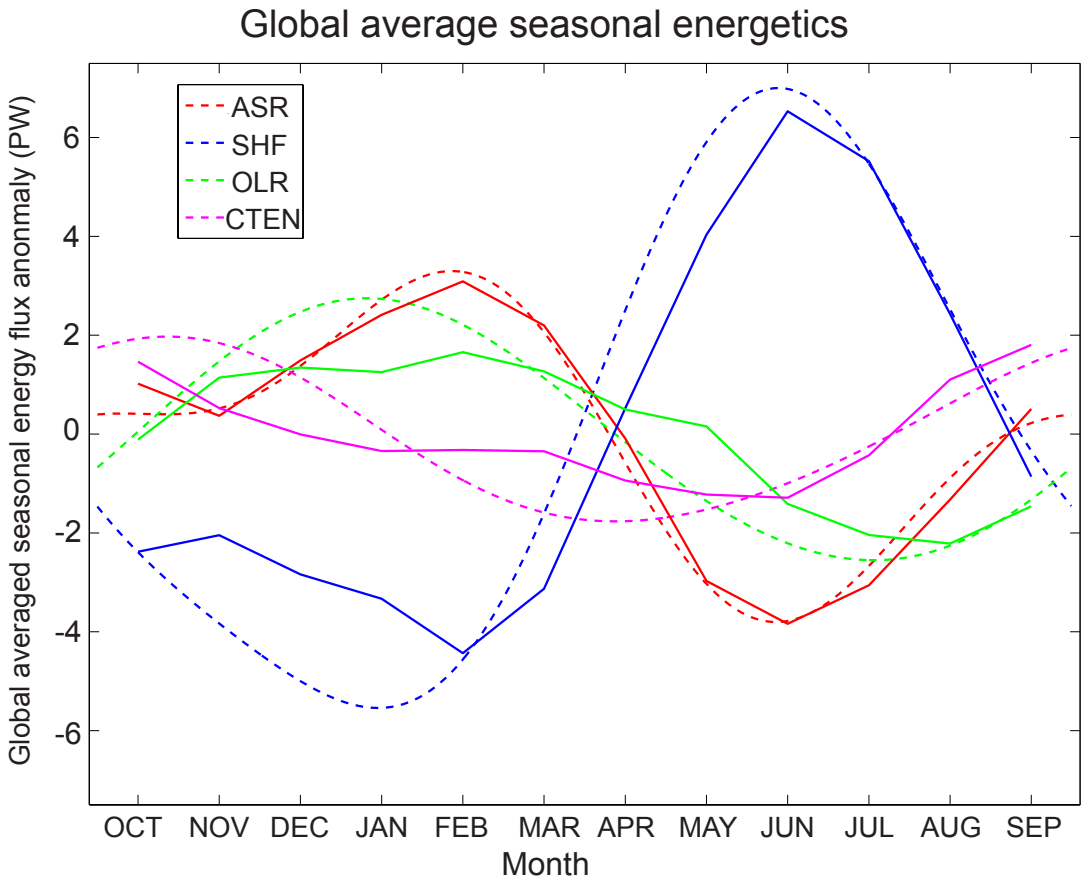

Figure 4.3: Global averaged seasonal energetics. All values are globally integrated seasonal anomalies from the global annual mean in PW. The dotted lines are the control six-box EBM simulation and the solid lines are the monthly mean observations.

the EBM seasonal amplitude of SH SHF is 14.5 PW as compared to 9.9 PW in the NH, which compares favorably to the observed amplitudes of 13.4 and 10.2 PW respectively. This result follows from the fact that the ocean surface layer must absorb a much larger quantity of energy than land before it achieves the same temperature anomaly as the land surface and subsequently fluxes a similar amount of energy to the atmosphere. Hence, a greater fraction of the seasonal ASR anomaly is fluxed to the atmosphere in the NH compared to the SH, producing greater amplitudes in the seasonal cycle of OLR, CTEN, and MHT in the NH compared to the SH. These results agree favorably with the observations.

Fig. 4.4 also illustrates the magnitude of errors induced by neglecting ocean heat transport in our EBM. By definition, the annual mean EBM SHF in each meridional domain is zero. The annual averaged SHF in nature is balanced by the vertically integrated ocean heat transport convergence. The ocean heat transport into the NH and SH extratropical boxes contribute to mean offsets between the observed and EBM simulated SHF seasonal cycles of +1.4 and +0.9 PW respectively. These numbers are significant and certainly impact the annually averaged energetics. They are, however, an order of magnitude smaller than the seasonal SHF anomalies, suggesting that the ocean's influence on *zonally averaged* climate is primarily through its thermal inertia, and secondarily by way of its dynamical heat flux (Seager et al., 2002).

4.4.3 Land-ocean energetics

The seasonal cycle of energy fluxes from the EBM control run for the land and ocean subdomains are shown in Fig. 4.5. Over the ocean in the NH, the SHF is of opposite sign and larger in magnitude than the ASR: during the summer, more energy gets put into ocean storage than is received from the sun, with the additional energy coming primarily from the zonal transport of heat (ZHT) away from the warmer land subdomain. In contrast, the predominance of ocean in the SH reduces the magnitude of ZHT in the ocean subdomain (because there is a larger area to distribute the heat fluxed from land to ocean) and the dominant seasonal balance is between ASR and SHF only, with limited seasonal cycles in

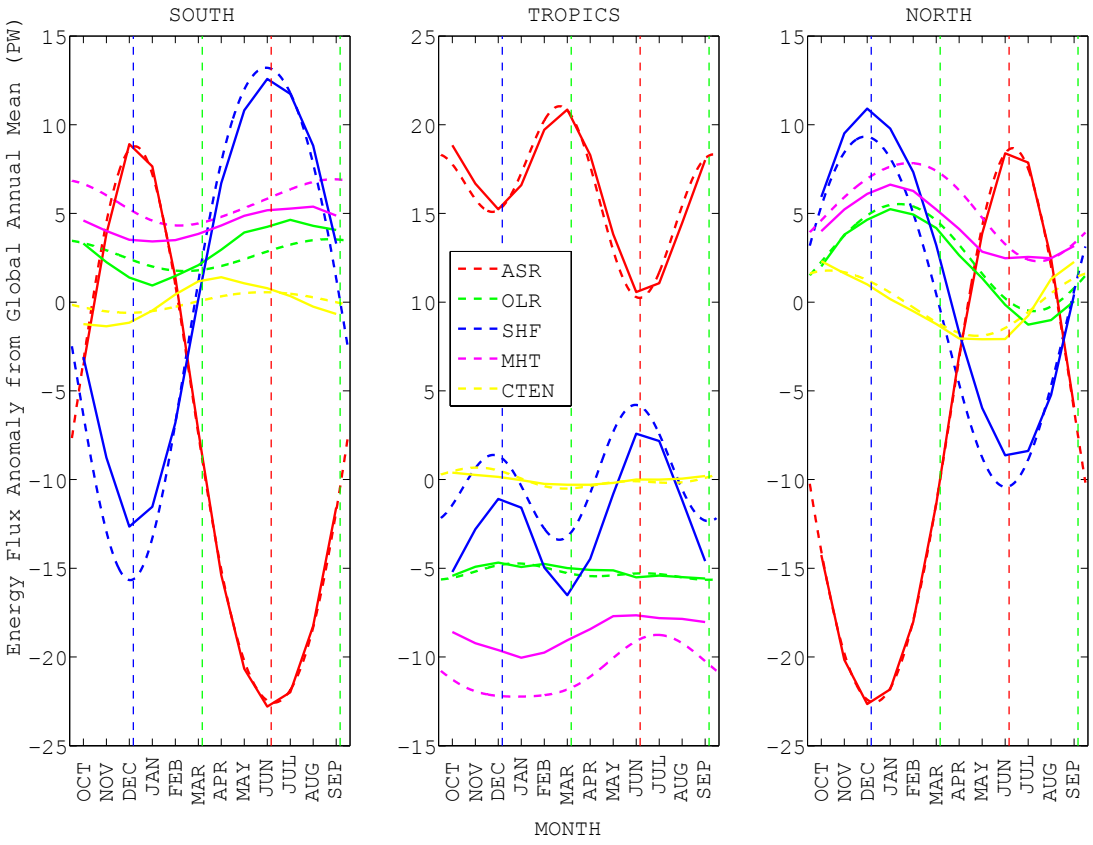

Figure 4.4: Seasonal cycle of energy fluxes over the tropical and extratropical domains. All values are anomalies relative to the global annual average in PW. The dashed lines are the six-box control EBM simulation and the solid lines are the monthly mean observations. The dashed vertical lines represent the solstices (blue and red) and equinoxes (green).

MHT, OLR, and CTEN. The SH ocean sub-domain behaves similarly to the aqua-planet EBM simulation with a 60 meter mixed ocean depth.

Over the extratropical land sub-domains, there is very little seasonal storage in the surface layer. Therefore, the majority of the energy entering the system through ASR finds its way into the atmosphere where it must be fluxed away (ZHT and MHT), radiated to space (OLR), or stored (CTEN). The seasonal magnitude of these terms, assuming they are all in phase, must add to the seasonal amplitude of ASR. The relative partitioning of energy across these terms is not as simple as the ratio of the B coefficients, however, because the ZHT relies on the land-ocean atmospheric temperature contrast and the temperatures above the ocean are also evolving seasonally. Furthermore, the MHT is determined by the zonal average atmospheric temperature in our formulation of the EBM. Hence, changes in meridional diffusion due to extratropical temperature changes in the land (ocean) sub-domain lead to smaller (larger) changes in MHT than would be expected based on the value of B_{MHT} because the magnitude of atmospheric temperature changes in the ocean (land) sub-domain are smaller (larger). Nonetheless, we can recognize that an isolated, instantaneous atmospheric temperature perturbation in the extratropical land-subdomain will induce energy flux changes that are proportional to the respective B coefficients. B_{ZHT} divided by land fraction has values of 20 and 100 Wm^{-2} in the NH and SH respectively; ZHT is therefore responsible for 65% and 90% of the total instantaneous atmospheric energy flux adjustment in the respective hemispheres. It is therefore not surprising that the large ASR anomalies over land are primarily compensated for by ZHT, and more so in the SH than in the NH. ZHT is the fastest (most sensitive) process in the climate system and, thus, the amplitude of the seasonal cycle over land in the extratropical SH and throughout the extratropical NH domain hinges critically on the land-ocean temperature contrast.

4.4.4 Land fraction experiments

The previous subsection suggested that the fractional land area (F_L) in the NH and SH had a profound effect on the local energetics. We now explore this parameter space more

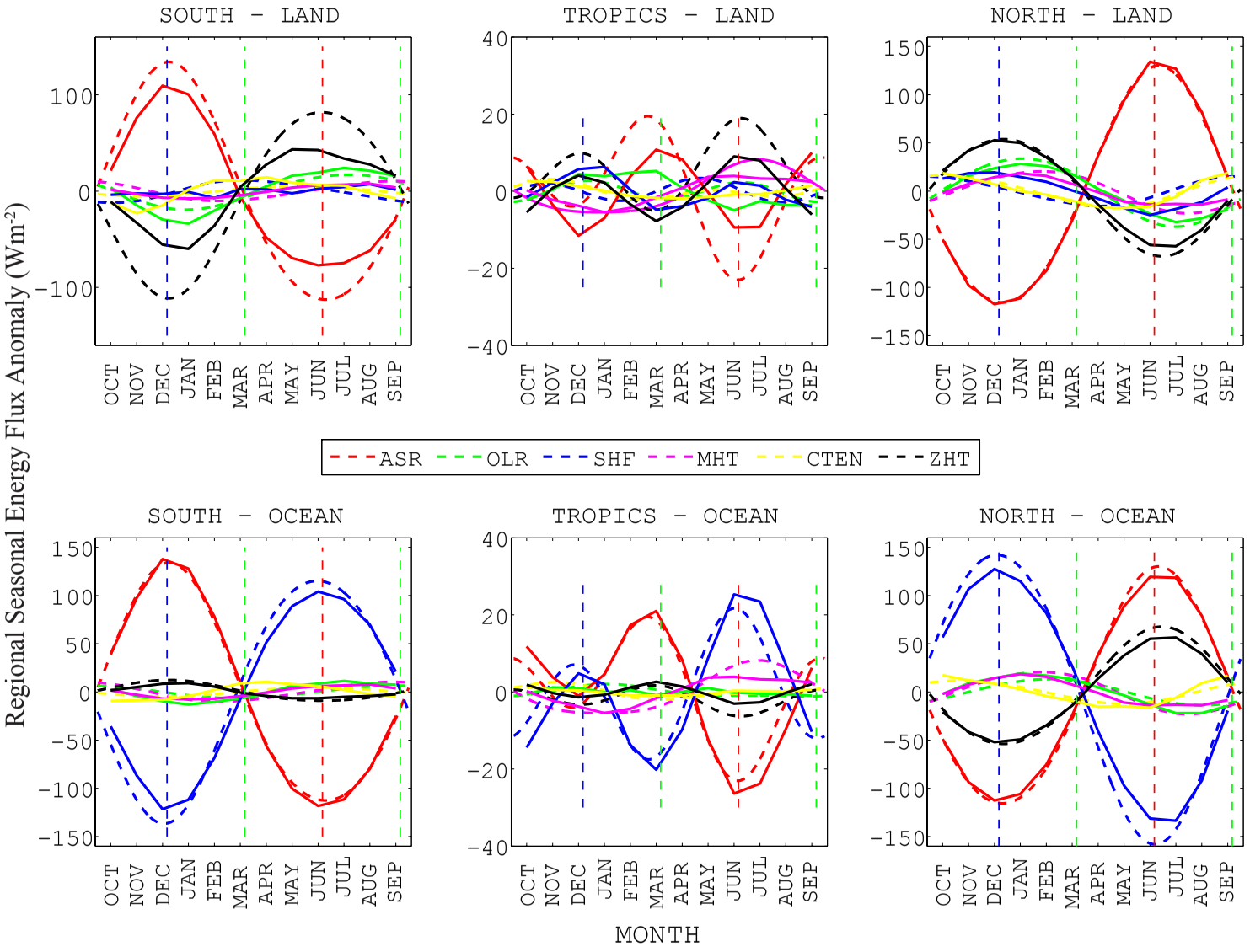

Figure 4.5: Seasonal energetics of the six-box EBM control run over the six subdomains. All values are seasonal anomalies from the local annual average in W m^{-2}. The dashed lines are the control six-box EBM simulation and the solid lines are the monthly mean observations.

completely in an ensemble of EBM integrations with varying extratropical land fractions (symmetric about the equator), forced by ERBE derived seasonal ASR anomalies. Fig. 4.6 summarizes the seasonal amplitudes of the temperatures and energetics over the extratropical sub-domains as a function of F_L.

4.4.4.1 Description of results

The energy balance model shows that the amplitude of the surface temperature over land doubles from 15 to 30C as the land fraction increases from near zero to near one. Increasing the land fraction causes an even larger increase in the amplitude of the seasonal cycle of atmospheric temperatures over land and ocean: from about 3 K at near zero land fraction to 16 K with nearly all land. The amplitude of the seasonal cycle in ocean temperature spans from 3 K with nearly all ocean to 5 K with a very large land fraction. The qualitative aspects of the climate response is not surprising: increasing the land fraction causes the seasonal cycle of temperatures to increase because a greater fraction of the seasonal ASR anomalies are delivered straight to the atmosphere by surface heat fluxes – nearly in phase with the ASR – and less is stored in the ocean (to be released to the atmosphere six months out-of-phase with the ASR).

The partitioning of the energy flux between the various processes as a function of land fraction over land and ocean is shown in Fig. 4.6b and c, respectively. The sensitivity in the seasonal cycle of climate as a function of land fraction (displayed in Fig 6a and discussed above) is largely due the zonal advection of energy. With no zonal advection, the amplitude of the seasonal cycle in atmospheric temperature over land would greatly exceed that over ocean, and lead the latter by about three months. Zonal advection balances out the temperature differences, mainly moving the excess (deficit) insolation in summer (winter) to the atmosphere overlaying the ocean in a matter of days. As the land fraction becomes small, this export term becomes very large (105W m^{-2})– nearly canceling the seasonal excess in ASR (120 W m^{-2}). Of course, the exported energy over land is a source of energy for the atmosphere over the ocean, a portion of which is emitted downward to

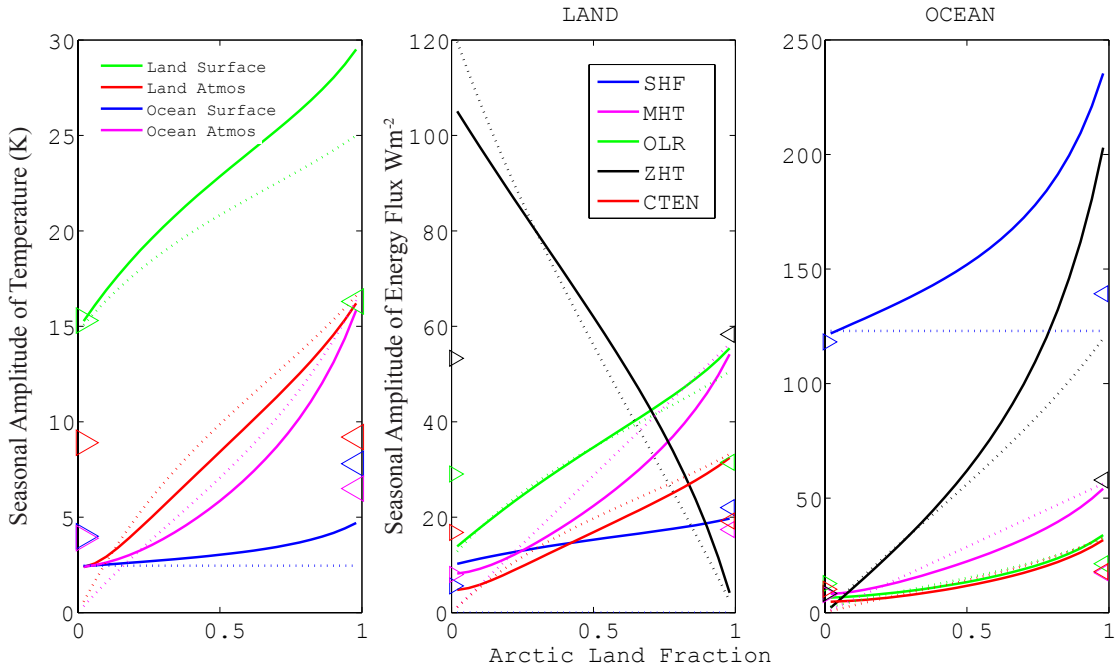

Figure 4.6: (a) Seasonal amplitude of surface and vertically averaged atmospheric temperatures over the land and ocean extratropical sub-domains as a function of F_L. (b) and (c) seasonal amplitude of energy fluxes over the extratropical land and ocean subdomains as a function of F_L. The solid lines are the results from the numerical integrations of the EBM. The dotted lines are the values based on pseudo-steady state ideas described in Subsection 4.4.4.2. The triangles on the left (right) side are the observations in the SH (NH).

add (in phase) with the seasonal cycle in ASR – enhancing the seasonal cycle of surface temperature in the ocean: the greater the land fraction, the more energy is exported from land to ocean (in phase with the ASR).

Finally, the seasonal cycle in the amplitude of the MHT and OLR also increase with increasing land fraction, in the net and over ocean and land. This result follows simply because the seasonal cycle in the surface temperature over land increases with increasing land fraction. This increases the amplitude of the seasonal cycle of heat flux to the atmosphere (in phase with the surface temperature and ASR) and so too an increase in the amplitude of the atmospheric temperature over land (and by zonal advection, over ocean). Hence,

increasing land fraction causes the seasonal cycle of both OLR and MHT to increase (the latter follows because the seasonal cycle of air temperature in the tropics is small). In the next section, we perform a scaling analysis to understand the qualitative and quantitative relationships between the fraction of land and the amplitude of the seasonal cycle in climate and the partitioning of energy fluxes between the various terms that are shown in Fig. 4.6.

4.4.4.2 Analysis of results

Perhaps the most robust result is that, independent of the F_L, the seasonal amplitude of surface temperature exceeds that of atmospheric temperature in the land sub-domain, where as the opposite is true over the ocean. For example, with 50% land, the ratio of $\mathrm{T}_S/\mathrm{T}_A$ is about 2.7 in the land subdomain and 0.5 in the ocean subdomain. This result seems physically intuitive given the reduced thermal inertia of the land surface as compared to the ocean leading to large land surface temperature tendencies. There is a compensating process, however: the enhanced seasonal amplitude of surface temperature, *ceteris paribus*, will induce proportionally larger amplitude seasonal energy fluxes from the surface to the atmosphere. Nonetheless, we still expect that the seasonal amplitude of surface and atmospheric temperature to be governed by equation 4.11, modified to account for both the ZHT between the land and ocean subdomains and the lack of LH over land:

$$\frac{|T'_{S,L}|}{|[T'_{A,L}]|} \equiv \mathrm{K}_L \tag{4.14a}$$

$$= \frac{B_{SENS} + B_{MHT}(F_L + \Delta(1-F_L)) + [B_{LW\uparrow}] + [B_{LW\downarrow}] + B_{CTEN} + \frac{B_{ZHT}(1-\Delta)}{F_L}}{B_{SENS} + B_{LW\uparrow,S}} \tag{4.14b}$$

with Δ the ratio of atmospheric temperature anomaly over ocean to that over land:

$$\Delta = \frac{[T_{A,O}]}{[T_{A,L}]}. \tag{4.15}$$

We can evaluate the effect of removing the LHF only, by setting $F_L$and Δ to one in 4.14, in which case K_L becomes 1.5, substantially smaller than the typical ratio of approximately 3 realized in the EBM simulations (Fig. 4.6a). Clearly, the land-ocean coupling plays a critical role in setting κ_L by moving excess energy fluxed to the atmosphere from the seasonally heated land surface to the ocean domain before the atmospheric column heats up. Though solving Eq. 4.14 requires knowledge of Δ, Δ must be less than one due to the greater fraction of ASR making its way into the atmosphere over land via the surface heat flux. Hence, ZHT greatly increases the seasonal amplitude of the surface temperature relative to atmospheric temperature (κ_L) in the land subdomain in 4.14.

Over ocean, the amplitude of the seasonal surface temperature to atmospheric temperature K_O is again given by a modified version of equation 4.11:

$$\frac{\left|T'_{S,O}\right|}{\left|\left[T'_{A,O}\right]\right|} = \mathrm{K}_O = \frac{B_{SENS} + B_{MHT}(F_L\Delta^{-1} + (1-F_L)) + [B_{LW\uparrow}] + [B_{LW\downarrow}] + B_{CTEN} + \frac{B_{ZHT}(1-\Delta)}{F_L}}{B_{LH} + B_{SENS} + B_{LW\uparrow,S}}. \tag{4.16}$$

The ZHT decreases K_O by adding energy to the atmosphere overlaying the ocean during the warm season. Essentially, because the atmospheric temperature anomalies have a greater magnitude over land (Δ<1), the direction of ZHT is dictated by the atmospheric temperatures in the land subdomain, thus acting as a negative (positive) feedback to atmospheric temperatures in the land (ocean) domain.

We can make some progress in understanding the coupled system by noting that, in the limit of a small F_L, the ocean sub-domain behaves similarly to the 60 meter aquaplanet. In this case Eq. 4.13 states that 85% of the seasonal energy from ASR is stored in the slab ocean. If we assume that the dominant balance is between ASR and SHF over the ocean and remove this energy balance, the resulting system of equations for the seasonal amplitude of energetics over land and ocean subdomains can be expressed by the matrix equation

$$\left(\frac{-B_{ZHT}}{F_L} - F_L B_{MHT} - B_{CTEN} - [B_{OLR}]\right) \left|[T'_{A,L}]\right| + \left(\frac{B_{ZHT}}{F_L} - (1-F_L)B_{MHT}\right) \left|[T'_{A,O}]\right| = |ASR'| \tag{4.17}$$

$$\left(\frac{B_{ZHT}}{F_L} - F_L B_{MHT}\right) \left|[T'_{A,L}]\right| + \left(-\frac{B_{ZHT}}{1-F_L} - (1-F_L)B_{MHT} - B_{CTEN} - [B_{OLR}]\right) |[T'_{A,O}] = 0 \tag{4.18}$$

where the Eq. 4.17 and Eq. 4.18 correspond to the energy balance in the atmosphere above the land and ocean sub-domains respectively. (In deriving Eq. 4.17 and 4.18, we have assumed that all of the ASR in the land domain is passed immediately to the atmosphere via the surface heat flux). The solution to 4.17 and 4.18 determines the seasonal amplitudes of atmospheric temperatures in the ocean and land subdomains and hence Δ (see Eq. 4.15). The seasonal amplitude of the surface temperature in the land and ocean subdomains is then obtained using Eqs. 4.14 and 4.16 respectively. Lastly, the seasonal energetics can be calculated by way of the temperatures and the B coefficients; all curves based on these equations are co-plotted in Fig. 4.6 and agree qualitatively with the EBM simulations[6].

The critical control parameter in the system is the land-ocean atmospheric temperature difference that governs the ZHT. In our pseudo equilibrium assumptions, the only external source of seasonal energy to the atmosphere is in the land subdomain (over the ocean subdomain, ASR goes into the ocean heat storage). This quantity of energy is fixed by the specified land fraction and ASR, and is a constraint to the land-ocean temperature contrast; the magnitude of the total zonal heat flux can not exceed the energy supplied at the source (ASR over land), otherwise the induced temperature changes would reverse the land sea temperature gradient driving the flux. In reality, less energy than the ASR integrated over the F_L is available to transport zonally because MHT, OLR, and CTEN also scale with atmospheric temperature anomalies according their respective B coefficients which are smaller than B_{ZHT}, but not negligible. Thus, as the $F_L$is increased, more energy is made available to the atmosphere to drive seasonal changes in ZHT to the ocean domain, as well as changes in MHT, OLR, and CTEN in both the ocean and land domain (Fig. 4.6)

There are limitations to the pseudo-equilibrium solution, mainly that we have assumed all of the

[6]In the pseudo steady state balance, the seasonal cycle of ocean temperature (and thus the ocean SHF) is necessarily and unrealistically unchanging with land fraction (the blue dotted curves in Fig. 4.6a,c).

ASR is absorbed in the ocean, thereby fixing the seasonal amplitude of the surface ocean temperature. Surprisingly, this assumption underestimates the ocean heat storage in the EBM; the presence of land ensures that, during the summer, the ocean surface layer absorbs more energy than is provided by the sun locally, especially as we increase the F_L. If we were to instantly turn off the EBM's heat transport in the middle of the summer, the atmosphere over the ocean would cool. This result is also true in the NH of the observed climate system. Essentially, a portion of the energy that is absorbed by the atmosphere over the land sub-domain during the summer finds it's way to storage below the ocean surface, just as a portion of the energy that is fluxed to the atmosphere from the ocean surface in the winter warms the continental atmosphere. Because the seasonal cycle is nearly symmetric about the equinoxes, these processes must be reflexive; a portion of solar insolation over the continent must find its way into the ocean mixed layer in order for the ocean to moderate the seasonal cycle over the continent.

We then can ask, what conditions must be met in order for the atmosphere to flux energy to the ocean? Energy is fluxed from the ocean surface to the atmosphere by way of latent and sensible heat fluxes and efficient (blackbody) radiation. In contrast, the atmosphere fluxes energy to the underlying ocean as a less efficient radiator, and via sensible heat fluxes. Therefore the seasonal amplitude of the atmospheric temperature must exceed that of surface temperature in order for the net flux to be from the atmosphere to the ocean in the summer. We can calculate the K_O that must be deceeded in order to have a net flux into the ocean by setting the net seasonal SHF to zero:

$$K_{O,crit} < \frac{B_{SENS} + [B_{LW\downarrow}]}{B_{SENS} + B_{LH} + B_{LW\uparrow,S}} = 0.37. \tag{4.19}$$

The EBM achieves $K_O$values below this critical value for $F_L > 0.7$. In reality, the atmosphere can drive a heat flux into the ocean with a substantially higher kappa value (i.e., with a substantially lower land fraction), because the atmospheric temperatures are nearly in phase with ASR in the coupled system, where as the ocean temperatures lag the ASR by a couple of months.

4.5 Summary and discussion

We have formulated a very simple EBM model to understand the gross energetics of the seasonal climate system – in particular, the relative importance of the processes that flux of energy between the tropics and the extratropics, and between the land and ocean regions. The advantage of this formulation is that the magnitude of the various energy fluxes can be understood in terms of their

respective sensitivities (B coefficients). We have shown that the dominant processes that control the annual averaged and seasonal cycle of energy fluxes can be deduced from the model control parameters and pseudo steady state ideas.

In the annual mean, the extratropics receive anomalously low (compared to the global average) absorbed solar radiation (ASR) that is balanced by meridional heat transport (MHT), outgoing longwave radiation (OLR), and surface heat fluxes (SHF) associated with ocean heat transport in approximately a 6:3:2 ratio. The ratio between MHT and OLR is well replicated and easily understood in terms of the B coefficients in our EBM, which are derived from solving the basic state and parameterizations derived from observations and AGCMs.

On the seasonal time scale, the majority of the extratropical ASR anomalies go into seasonal ocean storage, with smaller quantities of energy entering the atmosphere to drive seasonal changes in MHT, OLR, and the tendency in atmospheric energy storage (CTEN). The ratio of these component terms can be understood in terms of the relative B coefficients in our aqua-planet EBM framework. Furthermore, the fraction of energy supplied by ASR that goes into seasonal ocean storage versus that entering the atmosphere (to drive seasonal anomalies in OLR, MHT, and CTEN) is a strong function of mixed layer depth. This framework suggests that the energy flux processes that balance the seasonal cycle in ASR (and hence, the seasonal cycle of surface and atmospheric temperature) in the observed climate system is just as much a consequence of the ocean mixed layer depth as it is the Earth-Sun geometry. For example, as the ocean mixed layer depth decreases, the extratropical ASR anomalies become primarily balanced by MHT, OLR and CTEN, with SHF playing a much smaller role; at ocean depths of less than 15 meters, the seasonal amplitudes of MHT, OLR, and the surface and atmospheric temperatures exceed the annual mean extratropical anomaly in magnitude, implying that the equator to pole temperature and OLR gradients reverse sign during the peak of summer, and the atmosphere transports heat from pole to equator. This is not an artifact of the simplicity of our EBM: the aqua-planet GCM simulations with less than 12 meters ocean depth also exhibit this property. This result suggest that, as the equator to pole insolation gradient reverses in the summer, the only thing preventing the surface climate from following suite is the seasonal ocean heat storage. If this storage term were limited (i.e. in a snowball Earth), the Earth would exhibit an enhanced seasonal cycle in both temperature and meridional heat transport, the summer poles would momentarily exhibit the hottest climate on the planet, and heat would be exported from the poles to the tropics.

Land-ocean contrast in the zonal direction has a similar impact on the magnitude of the seasonal

energetics as does the equator to pole insolation differences. This result is understandable in our model framework. Our model parameters suggests that nearly all of the ASR over the ocean goes into seasonal storage beneath the surface, where as nearly all the ASR over land enters the atmosphere immediately. Concurrently, the zonal atmospheric heat transport between the ocean and land is remarkable fast and efficient, transporting large quantities of energy from the seasonally warm sector to the seasonally cold sector. This transport acts to limit the seasonal cycle of temperature over land, and enhances the seasonal oceanic heat storage relative to the heat that would be stored considering local radiation alone. The land fraction plays a critical role in governing the magnitude of these processes. Essentially, the larger the fraction of the domain that is land, the larger effect it has on the ocean domain and vice versa. A large land domain leads primarily to more seasonal energy put into the atmosphere, driving seasonal changes in MHT, OLR, and CTEN above both land and ocean, and secondarily to more ZHT to the ocean that is taken up is seasonal heat storage. A large ocean domain limits the net seasonal flux of energy to the atmosphere, thereby moderating the seasonal cycle of temperature, OLR, MHT, and CTEN, over both land and ocean.

Our results suggest that, on seasonal time scales, the local radiative (or other energy flux) perturbations exert a profound non-local effect on the coupled land-ocean climate system. For example, if a region of the Arctic ocean that is usually ice covered in the winter becomes open ocean in a warmer world, the immediate effect is an additional heat flux out of the ocean in the winter. In fact, this change is a larger energetic anomaly than turning on the summer Sun over the region, because the magnitude of seasonal heat storage exceeds the local seasonal cycle of ASR (Subsection 4.4.4) and therefore, is substantially larger than the radiative impact due to the albedo change of the melted ice. While the immediate impact is to warm the local atmosphere, our model framework tells us that, based on the B coefficients in the system, the majority of the energy (approximately 70% in the NH) will be fluxed zonally to the land domain. There, it will induce changes in MHT, OLR, CTEN, and the energy fluxed to the surface both radiatively and sensibly with the latter components composing approximately 40% of the initial heat that was fluxed zonally. At face value, only 30% of the initial energy perturbation finds its way to the land surface. However, where as the initial perturbation will have a small impact on ocean temperatures, the equivalent amount of heat will have a large impact on the land surface, which has essentially no heat capacity and must come to radiative-convective equilibrium with the additional downwelling energy flux. Within our model framework, melting 10% of the extratropical winter ice would cause the average land surface temperature to increase by 0.6 K. While our EBM is far too simple to be used to make such

predictions in the real climate system, it provides a framework for understanding seasonal energy balances such as these.

Chapter 5

CONCLUSION/DISCUSSION

The global scale energy fluxes in the climate system can be understood in terms of the spatio/temporal gradients of the energy entering the system (ASR) and the relative efficiencies of energy export. In Chapter 2, we demonstrated that, in the hemispheric average, ASR is primarily controlled by cloud reflection and only secondarily by surface reflection. In Chapter 3, we demonstrated that the equator-to-pole contrast of ASR (ASR^*) is also primarily controlled by atmospheric reflection (and varies significantly between models). Unsurprisingly, the same processes that control the global average ASR also control the meridional structure of ASR and thus the large scale forcing of the atmospheric and oceanic circulation in the climate system.

The equator-to-pole contrast of energy entering the climate system (ASR^*) must be balanced by the equator-to-pole gradient of energy radiated to space (OLR^*) and the energy transported between the tropics and extratropics (MHT_{MAX}) in an equilibrium system; the surplus of energy entering the tropics (relative to the global average) must be ameliorated by the sum of radiative and dynamic energy exports. As such, the ratio of MHT_{MAX} to OLR^* is equal to the relative efficiency of dynamic and radiative energy export on the equator-to-pole scale (hereafter,δ) and is of order 2 in both the observations and the models (Table 3.2). This suggests that dynamic energy export is a more efficient pathway toward achieving equilibrium on the equator-to-pole scale as compared to radiative energy export. It is therefore unsurprising that the large inter-model spread in ASR^* is primarily balanced by model differences in MHT_{MAX} and only secondarily by model differences in OLR^* (Chapter 3). In terms of the inter-model spread, a typical ASR^* anomaly is balanced by $MHT_{MAX}$and OLR^* anomalies in a ratio of approximately 2:1 (as assessed by the regression coefficients between MHT_{MAX}/OLR^* and ASR^* – Table 3.3). Thus, given the inter-model spread in ASR^* (from clouds), the inter-model spread in $MHT_{MAX}$and OLR^* behaves as we would expect based on the relative energy export efficiencies diagnosed from the observed climatology.

More formally, we can understand the conclusions reached in Chapter 3 in terms of the energy export efficiencies introduced in Chapter 4. In the annual average, the MHT_{MAX} into the extratropics in each climate model is equal to

$$MHT_{MAX} = ASR * \frac{MHT_{MAX}}{MHT_{MAX} + OLR*} \approx ASR * \frac{\delta}{\delta + 1}. \tag{5.1}$$

The first equality holds because the denominator of the middle expression is equal to $ASR*$ by Eq. 3.4. In the second approximate equality, δ is the ratio of the dynamic and radiative energy export efficiencies. In the annual average,

$$\delta = \frac{2B_{MHT}}{B_{OLR}} \approx \frac{MHT_{MAX}}{OLR*}, \tag{5.2}$$

(Chapter 4) and the near equality holds if both the $OLR*$ and MHT_{MAX} are linear functions of the temperature gradient. These equations provide a crucial link between the concepts discussed in Chapter 4 and the results presented in Chapter 3.

Eq. 5.1 demonstrates that inter-model differences in MHT_{MAX} are a consequence of inter-model differences in $ASR*$ or the relative efficiencies of the dynamic and radiative energy exports. We now explore the expected behavior of the inter-model spread in MHT_{MAX} in the hypothetical limits of model invariant $ASR*$ ("Limiting Model A") and model invariant energy export efficiency ("Limiting Model B").

"Limiting Model A": If all models had the same $ASR*$ value, then inter-model differences in MHT_{MAX} would be a direct consequence of inter-model differences in δ; models with more efficient meridional energy diffusion (B_{MHT}) or less efficient radiative exports (B_{OLR}) would have larger MHT_{MAX} values. MHT_{MAX} and $OLR*$ would be perfectly anti-correlated with a regression coefficient of negative 1.

"Limiting Model B": If B_{MHT} and B_{OLR} were model invariant but $ASR*$ differed between models, then MHT_{MAX} and $OLR*$ would be perfectly correlated with $ASR*$ (and each other) with the regression coefficients proportional to the relative magnitudes of B_{MHT} and B_{OLR} (and adding to unity). For example, if the dynamic energy export was 4 times more efficient than the radiative energy export in all models, then a model with a 1 unit anomaly in $ASR*$ would be balanced 0.8 units of MHT_{MAX} anomaly and 0.2 units of $OLR*$ anomaly; the regression coefficient between the inter-model spread in MHT_{MAX} ($OLR*$) would equal $\frac{\delta}{\delta+1}$ ($\frac{1}{\delta+1}$).

The large inter-model spread in $ASR*$ suggests that "Limiting Model A" is a poor fit to the inter-model spread in MHT_{MAX}. The correlation coefficients between MHT_{MAX}, $OLR*$, and $ASR*$ (Table 3.3) suggest that "Limiting Model B" is a descent, but far from perfect, description of the inter-model spread of MHT_{MAX}. We analyze these ideas more explicitly by plotting the inter-model spread of MHT_{MAX} in the $ASR*$- $\frac{MHT_{MAX}}{ASR*}$ plane (Fig. 5.1). MHT_{MAX} is the product of

the axis and ordinate (the colored contours) and can be interpreted as the product of the model's ASR^* value and relative efficiency of dynamic heat transport to all energy export processes. The axis and ordinate have been scaled by equal fractions of the inter-model average so that the same spread on the axis and the ordinate correspond to equal magnitude differences in MHT_{MAX} (the gradient of MHT_{MAX} has unit slope). In the NH, the inter-model spread on the axis and ordinate are comparable (the black rectangular border surrounding the inter-model average represents a one standard deviation anomaly on each axis) suggesting that inter-model differences in ASR^* and energy export efficiencies contribute nearly equally to the spread in MHT_{MAX}. In the SH the spread on the axis exceeds that on the ordinate by approximately 50%, suggesting that model differences in ASR^* contribute more to the MHT_{MAX} spread than do differences in the energy export efficiencies. This framework presents an alternative view of the inter-model spread in MHT_{MAX} that can be reconciled with the statistics of ASR^* and OLR^* presented in Chapter 3. The key component is that models disagree substantially on the relative efficiency of dynamic and radiative energy exports (ordinate of Fig. 5.1) but agree that dynamic energy export is a more efficient process. In the absence of ASR^* differences, models with more efficient dynamic heat transport have more MHT_{MAX} and less OLR^* ("Limiting Model A") and equal spread in OLR^* and MHT_{MAX}. In the absence of energy export efficiency differences ("Limiting Model B"), models with more ASR^* have more MHT_{MAX} and OLR^* but with the MHT_{MAX} difference anomaly approximately twice as large as the OLR^* anomaly (given by the inter-model average $\frac{\delta}{\delta+1}$). This process leads to more MHT_{MAX} spread and less OLR^* spread as was seen in the CMIP3 ensemble (Table 3.3). Therefore, the correlation between MHT_{MAX} and ASR^* seen in Chapter 3 is a consequence of the inter-model spread in ASR^* and an inter-model *average* δ value that is larger than 1. Inter-model variations in δ are significant and lead to a reduction of the correlations between ASR^* and MHT_{MAX} and also result in an insignificant correlation between MHT_{MAX} and OLR^*.

The energy exports from the extra tropical climate system are analogous to a water tank that receives a constant inflow flux of water and losses water through two pipes of different diameters. In equilibrium, the inflow flux is equal to the sum of the outflow flux in both the pipes and the magnitude of the outflow flux in each pipe is proportional to the cross sectional area of the pipe. The outflow rate through any one of the pipes can be altered by either changing the inflow flux or changing the relative diameters of the two pipes. By analogy, ASR^* is akin to the inflow flux and B_{MHT} and B_{OLR} are akin to the cross sectional area of the pipes. Each climate model has a unique inflow rate and unique pipe diameters but all models agree that the MHT_{MAX} pipe has

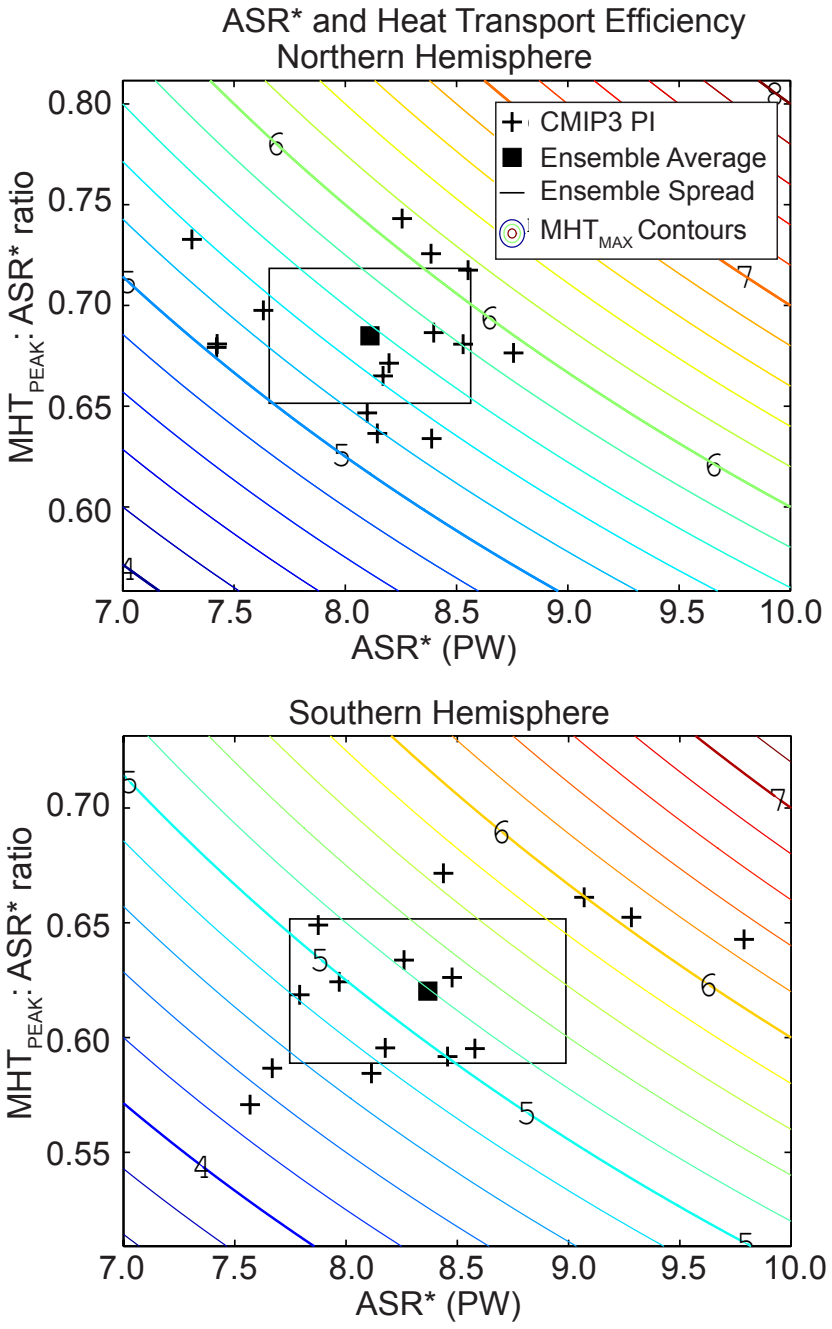

Figure 5.1: The ratio of MHT_{MAX}:ASR^* versus ASR^* for the CMIP3 PI simulations in the NH (left panel) and SH (right panel). The crosses are the individual models, the filled square is the ensemble average, and the hollow rectangular is one ensemble standard deviation on each axis. The colored contours are the MHT_{MAX} values.

a larger diameter than the OLR^* pipe (the ordinate in Fig. 5.1 is greater than 0.5). Therefore, inter-model differences in the inflow rate will primarily be seen in the variations of the MHT_{MAX} outflow. Inter-model differences in the pipe diameters result in tradeoff between the two outflow fluxes with more water flowing through one pipe at the expense of less water flowing through the other pipe. The former process results in more inter-model spread in the outflow flux through the MHT_{MAX} pipe (as compared to the OLR^* outflow flux spread) where as the latter process results in equal (and anti-correlated) spread in both outflow fluxes. As a consequence of the concurrent inter-model spread of inflow rates and pipe diameters, there is more spread in the MHT_{MAX} outflow flux that is well correlated (but not perfectly correlated) with the inflow flux spread (ASR^* spread).

We now apply the concepts of energy export efficiency to the change in MHT_{MAX} due to CO_2 doubling (Fig. 5.2). Similar to the inter-model spread, MHT_{MAX} can increase either by increasing the efficiency of dynamic energy export (or by decreasing the efficiency of radiative heat export) or by increasing ASR^*. The orientation of the blue arrows connecting the PI simulations (black crosses) to the 2XCO_2 simulations (red crosses) in the ASR^*- $\frac{MHT_{MAX}}{ASR*}$ plane indicate whether changes in the relative magnitude of the dynamic and radiative energy export efficiencies or ASR^* contribute more ΔMHT_{MAX}; horizontal (vertical) arrows indicate that changes in ASR^* (heat export efficiencies) play a larger role in the MHT_{MAX} change.

In the NH, all the models indicate that dynamic energy exports become more efficient relative to the radiative energy exports in the 2XCO_2 climate system (Soden and Held 2006). However, there is a large inter-model spread in ΔASR^* (Hwang and Frierson 2011) as can be seen from the ensemble average change (given by the thick blue arrow) and it's inter-model spread (1σ in each direction is given by the blue rectangle centered on the ensemble average change). The shift toward more efficient dynamic energy export is robust in the ensemble average (the blue rectangle does not intersect the PI inter-model average, given by the filled black square, along the ordinate) where as ΔASR^* is not significant (the blue rectangle crosses the PI inter-model average along the axis) and varies widely between models. As a consequence the inter-model average ΔMHT_{MAX} is not significantly different from zero as indicated by the overlap of the blue rectangle with the MHT_{MAX} contour value of the PI ensemble average (filled black square).

In the SH, the ensemble average change in energy export efficiency and ASR^* are both insignificant, and the inter-model spread in ΔASR^* has a large impact on the spread in ΔMHT_{MAX} as compared to the energy export efficiency change. These results suggests the uncertainty ΔASR^* (due to cloud reflection changes) overwhelm any anticipated change in dynamic or radiative energy

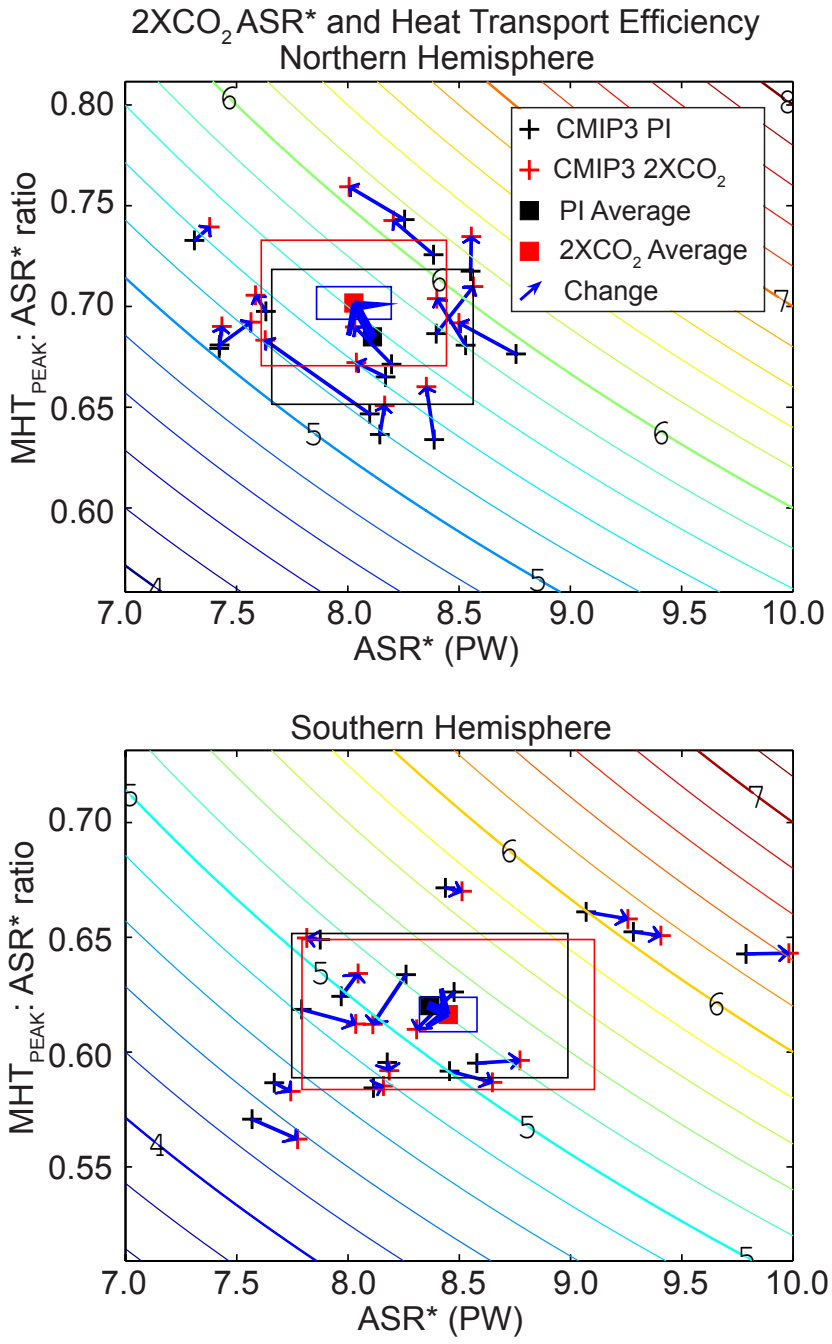

Figure 5.2: As in Fig. 5.1 except with the addition of the $2XCO_2$ simulations (red crosses, square, and rectangle). The blue vectors indicate the change on each axis from the PI to the $2XCO_2$ simulation. The thick blue arrow is the ensemble average change and the blue rectangle gives one ensemble standard deviation of the change centered on the $2XCO_2$ ensemble average (red square).

export efficiencies in terms of their affect on the change in meridional heat transport.

We started this thesis with a discussion of how analyzing large scale energy fluxes, both radiative and dynamic, across a multitude of spatio-temporal scales could provide further insight into the processes controlling the energy fluxes. This thesis has argued that the control of large scale energy fluxes can be thought of as a consequence of two bulk processes: (i) the processes controlling the spatio-temporal distribution of ASR and (ii) the relative efficiency of exporting energy between the regions and subcomponents of the climate system. We demonstrated that the ASR is controlled primarily by cloud properties and differs markedly between climate models. The relative efficiencies of energy exports are more constrained by fundamental physics (i.e. the Planck function is well established and the heat capacity of the atmosphere contrains B_{CTEN} in all climate models); while there is some inter-model variability in the energy export efficiencies, all models agree on the ranking of the various processes. For example, all models have more efficient dynamic energy export on the equator-to-pole scale as compared to the radiative energy export and seasonal heat storage in the oceanic mixed layer is a more efficient energy sink for seasonal ASR than radiaitve or dynamic energy exports. Spatio-temporal gradients in ASR will adjust toward equilibrium along the most efficient pathway, and therefore, the relative partitioning of the global scale energy fluxes scales as the ASR structure times the relative export efficiency of a given process. Therefore, while the exact details of the energy flux parameterization in models do contribute to the inter-model spread in the magnitude of the energy fluxes, the vast majority of the inter-model spread is a consequence of the ASR spread and its partitioning along the most efficient dynamic energy pathway (MHT_{MAX} for the annual average equator-to-pole contrast problem).

In future work, we hope to apply these same ideas to the inter-model spread in the seasonal cycle and its change in altered climate states. We hope this work will continue to put the relative efficiency of dynamic and radiative energy exports into a common framework that is applicable across a multitude of spatio-temporal scales.

BIBLIOGRAPHY

Barkstrom, B., E. Harrison, G. Smith, R. Green, J. Kibler, and T. E. S. T. R. Cess, 1989: Earth radiation budget (erbe) archival and april 1985 results. *Bull. Amer. Meteor. Soc.*, **70**, 1254–1262.

Barkstrom, B. R. and J. B. Hall, 1982: Earth radiation budget experiment (erbe)-an overview. *J. Energy*, **6**, 141–146.

Bender, F., A.-M., H. Rodhe, R. J. Charlson, A. M. L. Ekman, and N. Loeb, 2006: 22 views of the global albedo - comparison between 20 gcms and two satellites. *Tellus*, **58 (3)**, 320–330.

Bender, F., R. Charlson, and M. Ekman, 2010: Planetary albedo and cloud albedo in present and strongly forced climate. *J. Climate*, submitted.

Berger, A., 1978: Long-term variations of caloric insolation resulting from earth's orbital element. *Quaterbary Res.*, **9**, 139–167.

Boe, J., A. Hall, and X. Qu, 2009: Current gcms' unrealistic negative feedback in the arctic. *J. Climate*, **22**, 4682–4695.

Bony, S. and coauthors, 2006: How well do we understand climate change feedback processes? *J. Climate*, **19**, 3345–3482.

Budyko, M., 1969: The effect of solar radiation variations on the climate of the earth. *Tellus*, **21**, 611–619.

Cahalan, R. F., W. Ridgway, W. J. Wiscombe, T. L. Bell, and J. B. Snider, 1994: The albedo of fractal stratocumulus clouds. *J. Atmos. Sci.*, **51**, 2434–2469.

Curry, J., W. Rossow, D. Randall, and J. Scramm, 1996: Overview of arctic cloud radiation characteristics. *J. Climate*, **9**, 1731–1762.

Curry, J. A. and E. E. Ebert, 1992: Annual cycle of radiation fluxes over the arctic ocean: Sensitivity to cloud optical properties. *J. Climate*, **5**, 1267–1280.

Delworth, T. L., A. J. Broccoli, A. Rosati, R. J. Stouffer, V. Balaji, J. A. Beesley, and W. F. Cooke, 2006: Gfdl's cm2 global coupled climate models. part i: Formulation and simulation characteristics. *J. Climate*, **19 (5)**, 643–674.

Donohoe, A. and D. Battisti, 2011a: Atmospheric and surface contributions to planetary albedo. *J. Climate*, **in press**.

Donohoe, A. and D. Battisti, 2011b: What determines meridional heat transport in climate models? *J. Climate*, **submitted**.

Eastman, R. and S. Warren, 2010: Interannual variations of country-regionarctic cloud types in relation to sea ice. *J. Climate*, **23**, 4216–4232.

Emanuel, K., 2010: A simple model of multiple climate regimes. *J. Geophys. Res.*, **107**, doi:10.1029/2001JD001 002.

Enderton, D. and J. Marshall, 2009: Controls on the total dynamical heat transport of the atmosphere and oceans. *J. Atmos. Sci.*, **66**, 1593–1611.

Fasullo, J. T. and K. E. Trenberth, 2008a: The annual cycle of the energy budget: Pt i. global mean and land-ocean exchanges. *J. Climate*, **21**, 2297–2312.

Fasullo, J. T. and K. E. Trenberth, 2008b: The annual cycle of the energy budget: Pt ii. meridional structures and poleward transports. *J. Climate*, **21**, 2313–2325.

Gorodetskaya, I. V., M. A. Cane, L. Tremblay, and A. Kaplan, 2006: The effects of sea ice and land snow concentrations on planetary albedo from the earth radiation budget experiment. *Atmos.-Ocean*, **44**, 195–205.

Graves, C., W. Lee, and G. North, 1993: New parameterizations and sensitivities for simple climate models. *J. Geophys. Res.*, **98**, 5025–5036.

Hahn, C. and S. Warren, 2003: Cloud climatology for land stations worldwide, 1971-1996. numerical data package ndp-026d. *Carbon Dioxide Information Analysis Center (CDIAC), Department of Energy, Oak Ridge, Tennessee*, 35 pages.

Hall, A., 2004: The role of surface albedo feedback in climate. *J. Climate*, **17**, 1550–1568.

Hartmann, D., 1994: *Global Physical Climatology.* Academic Press.

Hartmann, D. L., L. Moy, and Q. Fu, 1979: A global surface albedo model. *J. Appl. Meteor.*, **18**, 239–253.

Hartmann, D. L., M. E. Ockert-Bell, and M. L. Michelsen, 1992: The effect of cloud type on earth's energy balance: Global analysis. *J. Climate*, **5**, 1281–1304.

Held, I. and B. Soden, 2006: Robust responses of the hydrological cycle to global warming. *J. Appl. Meteor.*, **19 (21)**, 5686–5699.

Holland, M. M. and C. Bitz, 2003: Polar amplification of climate in coupled models. *Climate Dyn.*, **21**, 221–232.

Hummel, J. and R. Reck, 1979: A global surface albedo model. *J. Appl. Meteor.*, **18**, 239–253.

Hwang, Y. and D. Frierson, 2011: Increasing atmospheric poleward energy transport with global warming. *Geophys. Res. Lett.*, **in press**.

Hwang, Y., D. Frierson, I. Held, and B. Soden, 2011: Corrigendum to held and soden (2006). *J. Climate*, **in press**.

International Panel on Climate Change [Griggs, D. and M. N. (eds.)], 2001: *Contribution of Working Group I to the Fourth Assessment Report of the Intergovernmental Panel on Climate Change.* Cambridge University Press.

International Panel on Climate Change [Solomon, S., D. Qin, M. Manning, Z. Chen, M. Marquis, K. Averyt, M.Tignor, and H. M. (eds.)], 2007: *The scientific basis. Contribution of Working Group 1 to the Third Assessment Report of the Intergovernmental Panel on Climate Change.* Cambridge University Press.

Kang, S., I. Held, D. Frierson, and M. Zhao, 2008: The response of the itcz to extratropical thermal forcing: idealized slab-ocean experiments with a gcm. *J. Climate*, **21**, 3521–3532.

Kato, S., T. Ackerman, J. Mather, and E. Clothiaux, 1999: The k-distribution method and correlated-k approximation for a shortwave radiative transfer model. *J. Quan. Spec. Rad. Trans.*, **62**, 109–121.

Kato, S., N. Loeb, P. Minnis, J. Francis, T. Charlock, D. Rutan, E. Clothiaux, and S. Sun-Mack, 2006: Seasonal and interannual variations of top-of-atmosphere irradiance and cloud cover over polar regions derived from ceres data set. *Geophys. Res. Lett.*, **33**, doi:10.1029/2006GL026 685.

Kiehl, J., 1994: On the observed near cancellation between longwave and shortwave cloud forcing in tropical regions. *J. Climate*, **7**, 559–565.

Kim, D. and V. Ramanathan, 2008: Solar radiation and radiative forcing due to aerosols. *J. Geophys. Res.*, **113**, doi:10.1029/2007JD008 434.

Kratz, D. P., S. K. Gupta, A. C. Wilber, and V. E. Sothcott, 2010: Validation of the ceres edition 2b surface-only flux algorithms. *J. Appl. Meteor.*, **49**, 164–180.

Li, C. and D. Battisti, 2008: Reduced atlantic storminess during last glacial maximum: evidence from a coupled climate model. *J. Climate*, **21**, 3561–3579.

Lin, S. J., 2004: A "vertically lagrangian" finite-volume dynamical core for global models. *Mon. Weath. Rev.*, **132 (10)**, 2293–2307.

Loeb, N. G., B. A. Wielicki, D. R. Doelling, G. L. Smith, D. F. Keyes, S. Kato, N. Manalo-Smith, and T. Wong, 2009: Towards optimal closure of the earth's top-of-atmosphere radiation budget. *J. Climate*, **22**, 748–766.

Lucarini, V. and F. Ragone, 2011: Energetics of ipcc4ar4 climate models: energy balance and meridional enthalpy transports. *Rev. Geophys.*, **49**, RG1001.

M.D., C. and K. Lee, 1996: Parameterizations for the absorption of solar radiation by water vapor and ozone. *J. Atmos. Sci.*, **53**, 1203–1208.

Meehl, G. A., C. Covey, T. Delworth, M. Latif, B. McAvaney, J. F. B. Mitchell, R. J. Stouffer, and K. E. Taylor, 2007: The wcrp cmip3 multi-model dataset: A new era in climate change research. *Bull. Amer. Meteor. Soc.*, **88**, 1383–1394.

Minnett, P. J., 1999: The influence of solar zenith angle and cloud type on cloud radiative forcing at the surface in the country-regionarctic. *J. Climate*, **12**, 147–158.

Moberg, A., D. M. Sonechkin, K. Holmgren, N. M. Datsenko, and W. Karlen, 2005: Highly variable northern hemisphere temperatures reconstructed from low- and high-resolution proxy data. *Nature*, **433**, 613–617.

North, G. R., 1975: Theory of energy-balance climate models. *J. Atmos. Sci.*, **32**, 2033–2043.

North, G. R. and J. A. Coakley, 1978: Simple seasonal climate models. *Meteorol. Gidrol.*, **5**, 26–32.

Qu, X. and A. Hall, 2005: Surface contribution to planetary albedo variability in the cryosphere regions. *J. Climate*, **18**, 5239–5252.

Robock, A., 1980: The seasonal cycle of snow cover, sea ice and surface albedo. *Mon. Weath. Rev.*, **108**, 267–285.

Roesch, A., 2006: Evaluation of surface albedo and snow cover in ar4 coupled climate models. *J. Geophys. Res.*, **111**, D15.

Rose, B. and J. Marshall, 2009: Ocean heat transport, sea ice, and multiple climate states: insights from energy balance models. *J. Atmos. Sci.*, **66**, 2828–2843.

Rutan, D., F. Rose, N. Smith, and T. Charlock, 2001: Validation data set for ceres surface and atmospheric radiation budget (sarb). *WCRP/GEWEX Newsletter*, **11 (1)**, 11–12.

S., Y., O. W.S., W. J.J., B. T.L., S. E.A., and C. Kummerow, 2006: Precipitation and latent heating distributions from satellite passive microwave radiometry. part ii: Evaluation of estimates using independent data. *J. Appl. Meteor. Clim.*, **45**, 721–739.

Seager, R., D. Battisti, J. Yin, N. Naik, N. Gordon, A. Clement, and M. Cane, 2002: Is the gulf stream responsible for europe's mild winters? *Quart. J. Roy. Meteor. Soc.*, **128**, 2563–86.

Sellers, W. D., 1969: A global climatic model based on the energy balance of the earth-atmosphere system. *J. Appl. Meteor.*, **8**, 392–400.

Sellers, W. D., 1973: A new global climatic model. *J. Appl. Meteor.*, **12**, 241–254.

Stone, P., 1978: Constraints on dynamical transports of energy on a spherical planet. *Dyn. Atmos. Oceans*, **2**, 123–139.

Taylor, K., M. Crucifix, P. Braconnot, C. Hewitt, C. Doutriaux, A. Broccoli, J. Mitchell, and M. Webb, 2007: Estimating shortwave radiative forcing and response in climate models. *J. Climate*, **20**, 2530–2543.

Thompson, D. and S. Solomon, 2002: Interpretation of recent southern hemisphere climate change. *Science*, **84**, 895–899.

Thompson, S. and S. Schneider, 1979: Seasonal zonal energy balance climate model with an interactive lower layer. *J. Geophys. Res.*, **84**, 2401–2414.

Trenberth, K. E. and J. M. Caron, 2001a: The atmospheric energy budget and implications for surface fluxes and ocean heat transports. *Climate Dyn.*, **17**, 259–276.

Trenberth, K. E. and J. M. Caron, 2001b: Estimates of meridional atmosphere and ocean heat transports. *J. Climate*, **14**, 3433–3443.

Trenberth, K. E. and J. T. Fasullo, 2009: Global warming due to increasing absorbed solar radiation. *Geophys. Res. Lett.*, **36**, doi:10.1029/2009GL037 527.

Trenberth, K. E., J. T. Fasullo, and J. Kiehl, 2009: Earth's global energy budget. *Bull. Amer. Meteor. Soc.*, **90 (3)**, 311–324.

Vonder Haar, T. and A. Oort, 1973: New estimate of annual poleward energy transport by northern hemisphere oceans. *J. Phys. Oceanogr.*, **2**, 169–172.

Warren, S. and S. Schneider, 1979: Seasonal simulation as a test for uncertainties in the parameterizations of a budyko-sellers zonal climate model. *J. Atmos. Sci.*, **36**, 1377–1391.

Wielicki, B., B. Barkstrom, E. Harrison, R. Lee, G. Smith, and J. Cooper, 1996: Clouds and the earth's radiant energy system (ceres): An earth observing system experiment. *Bull. Amer. Meteor. Soc.*, **77**, 853–868.

Wielicki, B., R. Cess, M. King, D. Randall, and E. Harrison, 1995: Mission to planet earth – role of clouds and radiation in climate. *Bull. Amer. Meteor. Soc.*, **76**, 2125–2153.

Wunsch, C., 2005: The total meridional heat flux and its oceanic and atmospheric partition. *J. Climate*, **18**, 4374–4380.

Appendix A

UNCERTAINTIES IN OBSERVATIONAL ESTIMATES OF $\alpha_{P,ATMOS}$ AND $\alpha_{P,SURF}$

The satellite derived TOA and surface shortwave fluxes used in this study are both uncertain. Here we analyze how the uncertainty in these fields propagates to uncertainties in $\alpha_{P,SURF}$, $\alpha_{P,ATMOS}$, and α_P.

The climatological CERES TOA shortwave fluxes have a total uncertainty of order 6 Wm^{-2} or about 2% of the incident radiation (Loeb et al., 2009); the error in the CERES surface shortwave fluxes is approximately 5% (Kratz et al., 2010). We propagate these errors to obtain error estimates in $\alpha_{P,ATMOS}$ and $\alpha_{P,SURF}$ using a Monte Carlo simulation. At each grid point, we add a random error to the observed flux; the error is assumed to be Gaussian with a standard deviation of 2% of the observed flux for the TOA fluxes and 5% of the observed flux for the surface fluxes. We then take 100 random realizations of the radiative fluxes and calculate $\alpha_{P,ATMOS}$ and $\alpha_{P,SURF}$ using the methodology outlined in Section 2.2.

The $\alpha_{P,ATMOS}$ and $\alpha_{P,SURF}$ maps averaged over the 100 realizations are statistically indistinguishable from the maps calculated using the original data suggesting that our partitioning algorithm is sufficiently linear over the range of the uncertainty in the observed radiative fluxes. The standard deviation of the $\alpha_{P,ATMOS}$ over the 100 realizations is approximately 5% of the average $\alpha_{P,ATMOS}$ over most of the domain while the standard deviation of $\alpha_{P,SURF}$ is approximately 10% of the average $\alpha_{P,SURF}$. The standard deviation of both $\alpha_{P,ATMOS}$ and $\alpha_{P,SURF}$ is significantly larger (reaching 25% of the average value) over the Greenland Ice sheet and East Antarctica where the surface albedo is large and the higher order reflections contribute to the partitioning algorithm (not shown).

We propagate the uncertainty in $\alpha_{P,ATMOS}$ and $\alpha_{P,SURF}$ onto the zonal averages (Fig. A.1) with error bars representing two standard deviations. If we assume that the uncertainties are random, and uncorrelated at adjacent grid points, the uncertainties in the zonal average $\alpha_{P,ATMOS}$ and $\alpha_{P,SURF}$ (shaded areas) are less than .008 at all locations. In this case the standard deviation of

the zonal average is approximately equal the standard deviation at a given grid point divided by the square root of the number of zonal gridpoints (zonal averaging reduces the uncertainty by more than a factor of 10). On the other hand, if the errors are systematic and have the same sign at all zonal locations, then the uncertainty in the zonal mean is equal to the zonal average uncertainty (dashed lines in Fig. A.1 give 2σ of this quantity). The true zonal average uncertainty is most likely somewhere in between these two estimates; observational errors at one gridpoint are expected to be correlated with those at their adjacent gridpoints with a spatial decorrelation scale that is regional (i.e. smaller than the zonal circumference assumed if the errors are systematic).

If the observational errors are systematic, the two standard deviation range of the global average $\alpha_{P,ATMOS}$ is 0.244-0.280 (82%-94% of the total planetary albedo); the two standard deviation range of global average $\alpha_{P,SURF}$ is 0.028-0.045 (9% - 15% of the total planetary albedo).

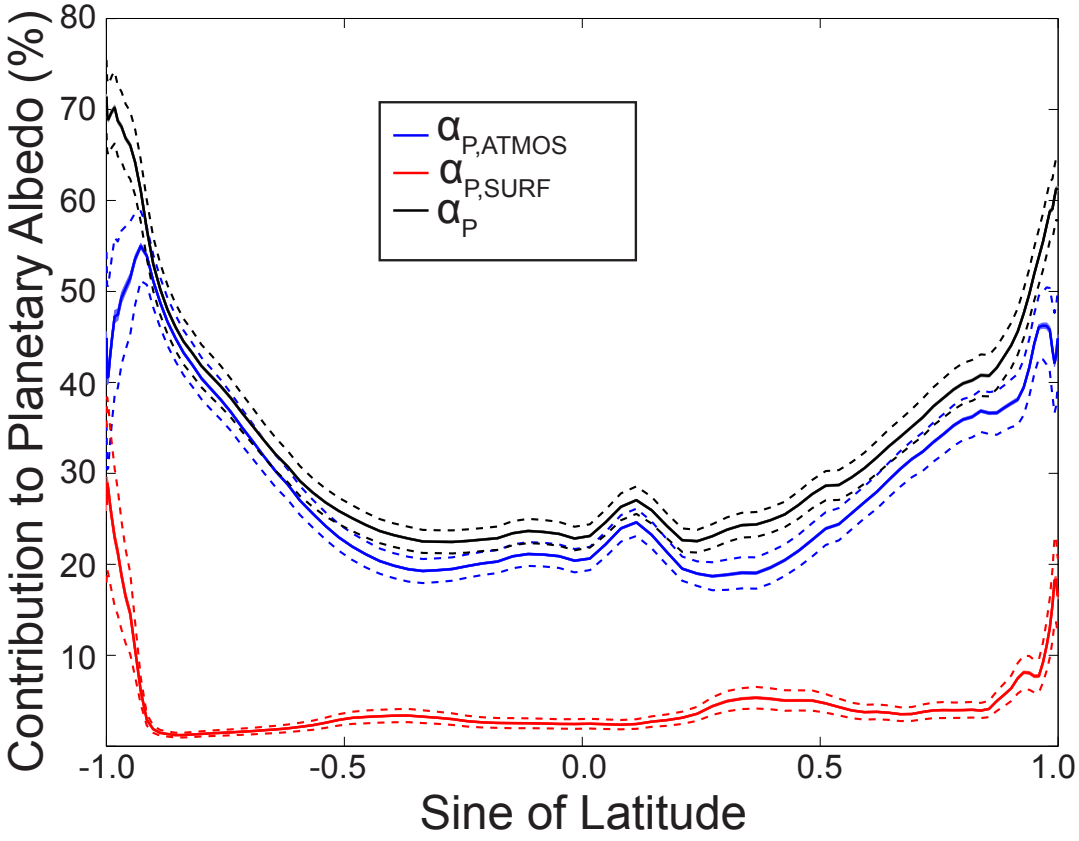

Figure A.1: Zonal average planetary albedo, $\alpha_{P,ATMOS}$, $\alpha_{P,SURF}$, and α_P calculated from the observations and their uncertainties (2σ) estimated from the Monte Carlo simulations described in the text. The shaded area is the uncertainty if the observational errors are random and uncorrelated at each gridpoint. The dashed lines are the uncertainty if the errors are systematic and perfectly correlated at all locations in each zonal band.

Appendix B

SENSITIVITY OF $\alpha_{P,ATMOS}$ AND $\alpha_{P,SURF}$ PARTITIONING METHODOLOGY

The partitioning of planetary albedo into surface and atmospheric components presented in this paper is contingent on the assumptions underlying the simple single layer shortwave radiative transfer model (Fig. 2.1 and Section 2.2). Specifically, we assume that (a) absorption and reflection of radiation is isotropic, (b) atmospheric absorption occurs during each pass through the atmosphere, and (c) absorption and reflection of shortwave radiation occurs at the same vertical level of the atmosphere. Taylor et al. (2007),hereafter T07, partitioned the planetary albedo feedback between atmospheric and surface processes using a similar conceptual model except that they assumed that the absorption of shortwave radiation in the atmosphere occurred only during the first downward pass through the atmosphere (differs from our assumption b) and that the absorption occurs above the level of atmospheric reflection (differs from our assumption c, see their Fig. 1). Specifically, T07 assume that downwelling shortwave radiation in the atmospheric absorption bands is entirely depleted prior to arriving at the cloud top level. (These assumptions allow the partitioning to be performed analytically). In contrast, we assume that shortwave radiation reflected from the surface also experiences some absorption on its upward path towards the TOA because calculations using a radiative transfer model (Kato et al., 1999) show that the atmospheric absorption of solar radiation increases as the surface albedo is increased from 0 to 1, indicating that solar radiation in the atmospheric absorption bands are *not* depleted in a single pass through the atmosphere. In this section, we explore the sensitivity of our results to these differing assumptions.

We apply the methodology of T07 to the observational and model data sets. We further illuminate the effects of the differing assumptions (b) and (c) by performing the planetary albedo partitioning with a model that assumes absorption occurs during the first pass through the atmosphere only, but that the absorption and reflection occur at the same level of the atmosphere. These three different models for partitioning planetary albedo are summarized in Table B.

The partitioning of planetary albedo into $\alpha_{P,ATMOS}$ and $\alpha_{P,SURF}$ using each of these models is shown in Fig. B.1 for both the observations and the ensemble average of the CMIP3 PI simulations.

Model Name	Number of passes with Atmospheric Absorption	Vertical Location of Absorption	Global Average $\alpha_{P,ATMOS}$	Global Average $\alpha_{P,SURF}$
This Study	Infinite (all passes)	Co-located with reflection	0.262 (88%)	0.036 (12%)
Taylor et al. (2007)	1	Above reflection	0.253(85%)	0.045 (15%)
Single Absorption	1	Co-located with reflection	0.246 (83%)	0.052 (17%)

Table B.1: Summary of the different simplified radiative transfer models used to calculate $\alpha_{P,ATMOS}$ and $\alpha_{P,SURF}$.

The model used in this study and the T07 model are in very close agreement in the partitioning of the observed planetary albedo at all latitudes. The T07 model finds lower values of $\alpha_{P,ATMOS}$ (and consequentially, higher values of $\alpha_{P,SURF}$) than the model used in this study at all latitudes. The average difference in $\alpha_{P,ATMOS}$ estimated using the two models is approximately 3% of the average $\alpha_{P,ATMOS}$ and does not exceed 10% at any latitude. Our model finds that 88% of the global average planetary albedo is due to $\alpha_{P,ATMOS}$ where as the T07 model finds a value of 85% (Table B). The single absorption model finds smaller values of $\alpha_{P,ATMOS}$ (and larger values of $\alpha_{P,SURF}$) than the other two models; on average, the single absorption $\alpha_{P,ATMOS}$ values are 4% smaller than the Taylor model and 9% smaller than the values found in this study.

The three methodologies yield similar results for the partitioning of planetary albedo between $\alpha_{P,ATMOS}$ and $\alpha_{P,SURF}$in the CMIP3 PI ensemble average. The smallest $\alpha_{P,ATMOS}$ values are obtained using the single absorption model and the model used in this study finds the highest $\alpha_{P,ATMOS}$ (Fig. B.1).

Although all three models give similar results for the partitioning of α_P, the three models disagree on the magnitude of the atmospheric attenuation of surface albedo (K). Our model finds that the atmosphere attenuates the surface albedo's contribution to the planetary albedo by 69% in the global average where as the country-regioncountry-regionTaylor and single absorption models find values of 61% and 57%. The differences in atmospheric attenuation between the three models are largest in the dry subtropics where atmospheric reflection is relatively small and, thus, absorption contributes to a larger fraction of the atmospheric opacity. Our model determines significantly larger values of attenuation in this region relative to the T07 and single absorption models because absorption

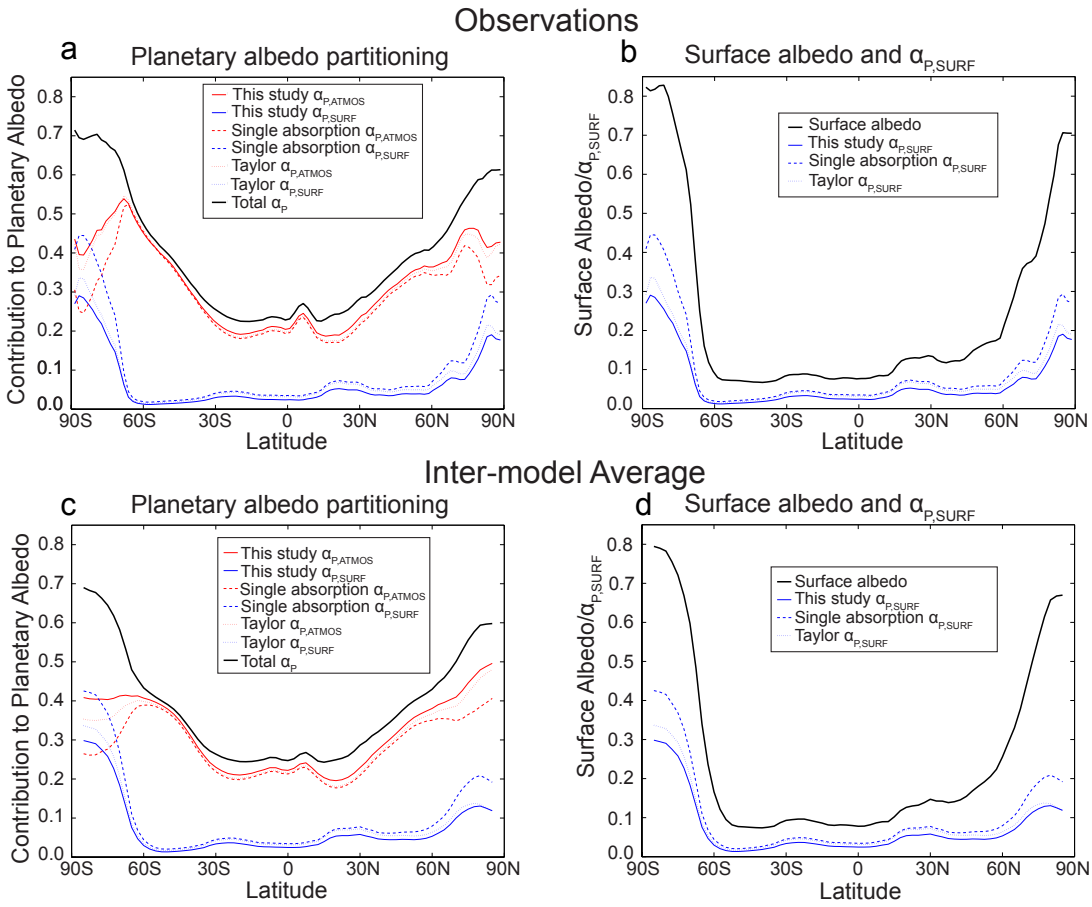

Figure B.1: (a) Planetary albedo partitioning in the observations using the model described in this study, the single absorption model, and the model of Taylor et al. (2007). (b) The surface albedo and the surface contribution to planetary albedo ($\alpha_{P,SURF}$) using the three methods of planetary albedo partitioning. (c) and (d) as in (a) and (b) except for the CMIP3 inter-model average.

increases the atmospheric opacity to upwelling shortwave radiation in our model and thus a smaller fraction of the radiation reflected by the surface escapes to space.

Although an evaluation of which model most accurately captures the radiative behavior of the atmosphere is beyond the scope of the present work, we will briefly comment on the source of differences in the results obtained using the three models, and why the T07 model yields results that are in closer agreement with our results than those using the single absorption model. The ratio of downwelling radiation at the surface and at the TOA is roughly equal to the atmospheric tranmissivity (neglecting the effect of multiple reflections) and is constrained by the input radiative data used to partition the planetary albedo. In our model, the atmospheric transmissivity is *(1-R-A)* where as in Taylor's model[1] it is (1-R_T)(1-A_T) where the subscripts have been added to denote that the R and A values determined by the two models are not equivalent. Expanding out the opacity in T07's model, and knowing that values for A and A_T are similar (although A is always = A_T), one can show that $R_T > R$. This is because the radiation reaching the cloud top has been depleted by absorption in the T07 model (and not in our model). Hence, clouds in the T07 model must reflect a larger fraction of the radiation incident at cloud top to satisfy the other radiative constraints imposed by the input data. The opacity to upwelling radiation in our model is *(1-R-A)* where as in the T07 model it is *(1-R_T)*. The exclusion of absorption in atmospheric opacity to upwelling radiation in the T07 model is partially balanced by the fact that $R_T > R$. As a consequence, our model and the T07 model produce results that are in close agreement.

[1]T07 call this quantity μ (1$-\gamma$), where μ is (1-A$_T$) and γ is reflection.

Appendix C

DETAILS OF THE SEASONAL ENERGY BALANCE MODEL

Here we elaborate and provide justification for the parameterizations used in the EBM presented in Chapter 4. We have diagnosed our parameterizations from linear best fits to the observations or, in some cases, simulations using an aquaplanet AGCM coupled to a slab ocean.

C.1 Latent heat flux parameterization

We diagnose a simple surface latent heat flux parameterization from the ensemble of five aquaplanet AGCM simulations described in Section 4.2.1 by regressing the monthly mean latent heat flux against the monthly mean surface temperature for all data points and seasons collectively (Fig. C.1 shows the 12 meter depth slab ocean regression). The regression coefficients from each of the runs are averaged to obtain the coefficient B_{LH} in Eq. 4.1; the ensemble average R^2 value is 0.8. We chose to diagnose this relationship from AGCM simulations as opposed to observations because the AGCM diagnostics are more readily available and internally self consistent.

C.2 Sensible Heat Flux Parameterization

The surface to atmosphere sensible heat flux is also diagnosed from the aquaplanet AGCM runs by regressing the sensible heat flux against the difference between the surface temperature and the 900 hPa atmospheric temperature for all grid-points and months collectively (Fig. C.1b). The linear best fits have an intercept that is significantly different from zero, as would be expected from the vertical lapse rate within the atmosphere. The ensemble average regression gives the coefficients B_{SH} used in Eq. C.2, (with an ensemble average R^2 value of 0.7), assuming that the lowest EBM atmospheric layer can be substituted for the 900 hPa level. The constant C_{SH} in Eq. C.2 is then adjusted to account for the lowest EBM layer corresponding to a significantly higher level in the atmosphere than the 900 hPa level.

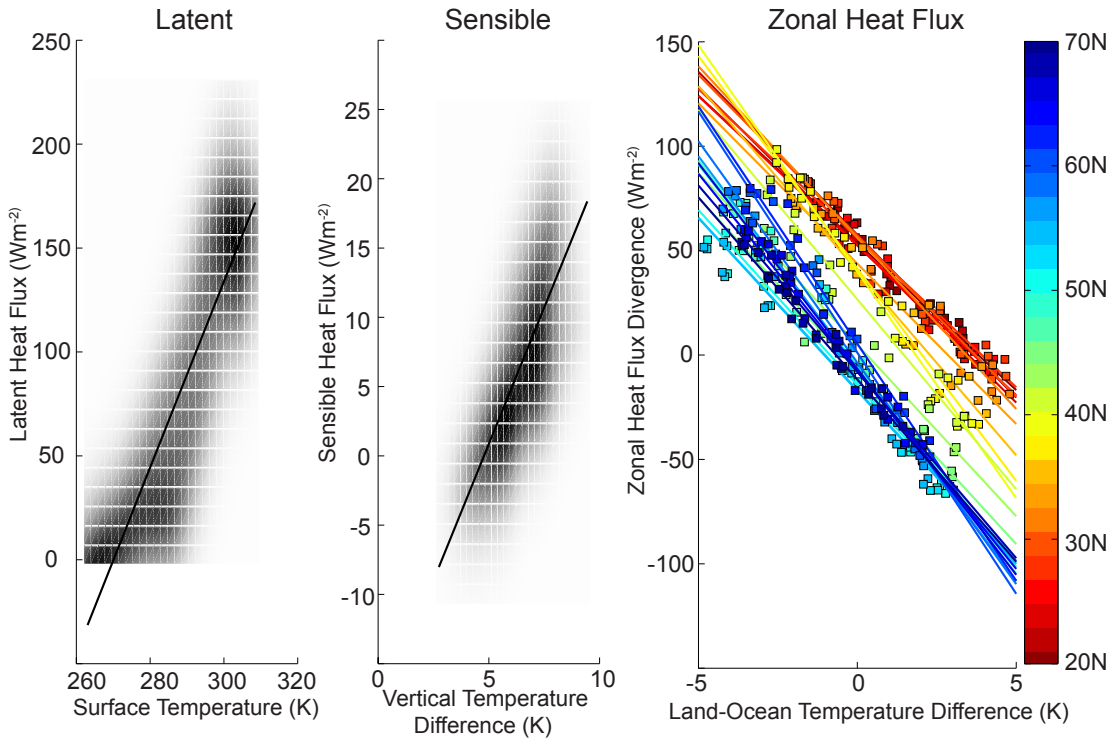

Figure C.1: (a) 12 meter depth Aquaplanet AGCM surface latent heat flux versus surface temperature for all gridpoints and seasons, plotted as a density function. The straight line is the linear best fit. (b) as in (a) except for the sensible heat flux (ordinate) and surface temperature minus 900 hPa temperature (abscissa). (c) The heat flux divergence due to land-ocean zonal heat transport (calculated from the reanalysis as described in the Appendix section e) versus the land-ocean vertically averaged temperature difference. Each set of the same colored dots represent the monthly mean values at a given latitude and the corresponding colored line is the linear best fit to the data at that latitude. Only data between 20°N and 70°N are shown in these plots.

C.3 Water vapor feedback factor

Linearizing the radiation about the single column atmosphere mean state described in Section 4.2.1.1, gives an OLR anomaly that can be expressed as a weighted average of the local $B_{OLR,N}$s with the weights representing the relative contribution of each layer to the radiation emitted to space:

$$OLR^{'}|_{\varepsilon} = \sum_{N=1}^{4} B_{OLR,N} T_N^{'} \varepsilon_N \prod_{n=N+1}^{4} (1-\varepsilon_n) \equiv \sum_{N=1}^{4} B_{OLR,N} T_N^{'} W_N \tag{C.1}$$

where W_N is a normalized weighting coefficient. This expression states that, for a system with fixed layer emissivities, the inverse climate sensitivity for the entire column is the weighted average of the local $B_{OLR,N}$s, which vary from 5.3 W m^{-2} at the surface (N=1) to 2.8 W m^{-2} in the highest atmospheric layer in our basic state. All these values are significantly larger than the more commonly accepted values for inverse climate sensitivity (of order 2 W m^{-2} K^{-1}, see Warren and Schneider, 1979, for a discussion). Therefore, the weighted column average calculated from Eq. C.1 will not give a realistic inverse climate sensitivity (in our model, Eq. C.1 gives a value of 4 W m^{-2} K^{-1}) unless the column mean emission temperature drops to approximately 200 K.

The missing component is the water vapor feedback. The layer emissivities increase with increasing temperatures (due to the impact of water vapor on emissivity and temperature on water vapor via the Clausius Clayperon equation) leading to an upward shift of the emission level (i.e. the vertical weighting function) with increasing atmospheric temperature. Therefore, a warmer column will emit from a higher level in the atmosphere where the basic state temperatures are colder (and the emitted longwave radiation is less energetic). This phenomenon partially offsets the increase in OLR from local heating of the column only (i.e. Eq. C.1). We can take this into account while still maintaining the linearity in our model by decomposing the change in OLR into a component due directly to temperature change and a component due to the change in emissivity (itself due to temperature change):

$$\frac{d(OLR')}{d([T'])} = \frac{\partial(OLR')}{\partial([T'])}\bigg|_{\varepsilon} + \frac{\partial(OLR')}{\partial(\varepsilon)}\bigg|_{[T']} \frac{\partial(\varepsilon)}{\partial([T'])} \approx C_{WV} \frac{\partial(OLR')}{\partial([T'])}\bigg|_{\varepsilon}. \tag{C.2}$$

The fixed emissivity term was discussed above. The fixed temperature term is assessed to be -1.4 W m^{-2} K^{-1} in our 3-layer atmospheric mean state using Emanuel's (2002) formulation of emissivity with a fixed relative humidity of 70% and a CO_2 concentration of 350 ppm. C_{WV} is the sum of the two terms divided by the fixed emissivity term and has a value of 0.65; it allows us to incorporate

the water vapor feedback into the EBM while retaining linearity.

C.4 Meridional heat transport

We assume that the meridional heat flux divergence can be approximated by temperature diffusion:

$$MHT = D\nabla^2[T], \tag{C.3}$$

where D is a diffusive parameter intended to capture the net effect of synoptic eddies and ∇^2 is the spherical Laplacian. Taking the zonal mean of Eq. C.3 and Legendre expanding gives

$$A_{MHT,L} = D\frac{L(L+1)}{a^2}A_{T,L} \tag{C.4}$$

where $A_{MHT,L}$ and $A_{T,L}$ are the L^{th} meridional wavenumber spectral coefficients in the zonal mean heat transport divergence and temperature respectively. We obtain the Legendre coefficients for the annual mean heat transport divergence and vertically averaged temperature from reanalysis data and determine D from Eq. C.4. If the heat transport were truly diffusive, each meridional wavenumber would determine the same value of D; in reality the calculated D values differ from one wavenumber to the next. We chose the value of D that is associated with meridional wave number 2 ($D = 0.95a^2$ W m^{-2} K^{-1}) because meridional wavenumber 2 is the dominant scale associated with the equator to pole difference (this scale dominates the variance in both expansions).

We now relate this D value to the B_{MHT} value used in equation 4.5. The D value must be multiplied by the spherical Laplacian eigenvalue which is $6a^{-2}$ at the equator to pole scale (wavenumber 2). Additionally, we recognize that the finite difference formulation of the diffusion equation used in 4.5 only approximates the spatial structure of the 2^{nd} Legendre polynomial; in reality, the finite difference equation specifies a boxcar function with unit magnitude, changing signs at 30°. We determine how the EBM specification of the equator pole gradient relates to the Legendre coefficients in Eq. C.4 by projecting the boxcar function onto the 2^{nd} Legendre polynomial; each unit of tropical-extratropical temperature difference in the EBM geometry corresponds to 0.63 units of the 2^{nd} Legendre polynomial. Thus, the value D must be multiplied by these two geometric factors to get the value of B_{MHT} specified in Section 4.2.1.

C.5 Zonal heat flux

We diagnose the zonal heat flux parameterization from the reanalysis products. For each latitude between 20°N and 70°N (where land is prevalent), we first subtract the zonal averaged heat flux divergence (equivalently, the meridional heat transport divergence) from the heat flux divergence and then average the residual over the land domain; this quantity represents the heating over land due to zonal heat transport from the ocean domain. We then regress the (monthly) climatology of this quantity against the (monthly) climatological atmospheric temperature difference between the land and ocean domains, at each latitude separately (Fig. C.1c). The resulting best fit slopes for each latitude (12 monthly points go into each regression) have fairly constant slopes with an average of -19 W m^{-2} K^{-1} corresponding to a zonal advection speed of 16 m/s if we assume that both the zonal temperature and heat flux divergence anomalies follow a zonal wavenumber 2 structure (corresponding to the presence of the American and Asian continents at these latitudes). This average slope is related to the ZHT parameterization given in Eq. 4.6 by assuming that this data corresponds to a land fraction of approximately 50%. We postulate that the change in intercept with latitude seen in Fig. C.1c results from more water vapor import from ocean to land in the low latitudes, where the ocean is warmer.